BremHLR
Kompetenzzentrum für Höchstleistungsrechnen Bremen

Statusbericht 2023

des

Kompetenzzentrums

für

Höchstleistungsrechnen Bremen

–BremHLR–

Bremen, Juni 2024

Universität Bremen
CONSTRUCTOR UNIVERSITY
AWI ALFRED-WEGENER-INSTITUT HELMHOLTZ-ZENTRUM FÜR POLAR- UND MEERESFORSCHUNG
HSB Hochschule Bremerhaven

HLRN
Norddeutscher Verbund für Hoch- und Höchstleistungsrechnen

© 2003-2024 BremHLR – Kompetenzzentrum für Höchstleistungsrechnen Bremen

www.bremhlr.uni-bremen.de

Das Berichtsjahr 2023 in Stichpunkten

- Einbindung an den NHR-Zentren Berlin und Göttingen
- Stabiler Betrieb der beiden NHR-Systeme im HLRN
- Verfügbarkeit von Graphik-Prozessoren (GPUs) an beiden HLRN-Standorten

Inhaltsverzeichnis

1 BremHLR: Aufgaben und organisatorische Struktur 5
1.1 Aufgaben 5
1.2 Struktur 5
2 Tätigkeitsprofil des BremHLR im Berichtszeitraum 6
2.1 Unterstützung der HLRN-Nutzung im Land Bremen 6
2.2 Weitere Aktivitäten des BremHLR 6
3 Statistische Angaben zu den Bremer Höchstleistungsprojekten 7
4 Veranstaltungen mit Beteiligung des BremHLR 8
5 Projektberichte 10
5.1 *hbb00001:* Exploring the conformational phase space of N-linked glycans using enhanced molecular dynamics and sketch-map analysis 10
5.2 *hbb00003:* Unravelling the mechanism of ion transport of the HumanP2X4R receptor channel 12
5.3 *hbc00045:* Rupturing Materials in Electric Fields 14
5.4 *hbc00056:* Towards an atomic-level understanding of the interaction of probe molecules with acid sites in zeolites 18
5.5 *hbc00061:* Studying the Wet and Dry CO Oxidation on Nanoporous Gold Using Static DFT Computations and AIMD Simulations 22
5.6 *hbc00062*: Adsorption of pharmaceuticals and personal care products in zeolites studied with density functional theory calculations 26
5.7 *hbi00037:* Molekulardynamische Untersuchung der Stressbean-spruchungen auf Proteine an der Phasengrenzfläche beim Premix-Membranemulgieren 30
5.8 *hbi00059:* A systematic ab-initio vibrational spectra study of Mars' olivine solid solutions 34
5.9 *hbi00062*: Multiphase numerical modeling for water jet quenching of the stationary and moving metal plate 38
5.10 *hbk00059*: Joint state-parameter estimation for the Last Glacial Maximum with CESM1.2 41
5.11 *hbk00062:* Retrieval of stratospheric ozone profiles from OMPS observations in limb geometry and long-term trends 45
5.12 *hbk00083:* Tipping points in the ecosystem of the 'new Arctic' Ocean 49
5.13 *hbk00084:* Marine biogenic aerosol precursors in the Arctic Ocean 52
5.14 *hbk00085:* Modellierung des Einsetzens der letzten Eiszeit 55
5.15 *hbk00090:* Paleoclimate Applications of Mixing Parameterizations in an Earth System Model 58

5.16 *hbk00094:* The effects of Ocean Alkalinity Enhancement on the anthropogenic CO2 concentrations in the 21st century 62

5.17 *hbk00095:* Application of ensemble data assimilation for improved prediction of ocean ecosystem indicators 67

5.18 *hbk00096:* Tropical Climate Variability of the Past 70

5.19 *hbk00097:* Improved Projections of the Antarctic Ice Sheet Contribution to Sea Level Rise until 2100 using Coupled Ice Sheet-Ice Shelf-Ocean Modelling 74

6.20 *hbk00098:* Climate Data Record of Stratospheric Aerosols 78

6.21 *hbk00099:* Ocean - ice shelf interaction at the 79 North Glacier: Sensitivity to bathymetry and environmental conditions 84

6.22 *hbp00058:* Exploring the mechanistic process of vitamin B_{12} acquisition by human gut bacteria 87

6.23 *hb00067:* Relaxation and Multiplication in Bi doped Graphen 91

6.24 *hbp00068:* Enhanced sampling methods for constructing free energy surfaces of antibiotic permeation through porins 94

6.25 *hbp00075:* Computational search for more efficient thermal barrier coatings using the Wigner formulation 98

6.26 *hbp00076:* Multiscale analysis of the dynamic interactions of nanoparticles and oil-soluble surfactants at liquid interfaces 101

1 BremHLR: Aufgaben und organisatorische Struktur

1.1 Aufgaben

Das Land Bremen beteiligt sich am Norddeutschen Verbund für Hoch- und Höchstleistungsrechnen – HLRN – um an dem rasanten Fortschritt der Computer- und Softwaretechnologie Teil zu haben. Das Kompetenzzentrum für Höchstleistungsrechnen Bremen – BremHLR – unterstützt dazu Wissenschaftler im wissenschaftlichen Rechnen insbesondere im Land Bremen. Die Fachberater des BremHLR leisten Unterstützung für Projekte sowohl in der Konzeption, der Antragstellung als auch der Durchführung. Der Schwerpunkt der Unterstützung liegt hierbei auf Projekten auf den beiden HLRN-Systemen. Seit 2005 wurde die Betreuung aber auch auf Rechenprojekte an den nationalen Höchstleistungsrechenzentren wie z. B. dem Jülich Supercomputing Centre (JSC) ausgeweitet.

Als Bestandteil im Kompetenznetzwerk des HLRN beteiligt sich BremHLR unter anderem an der fachspezifischen Nutzerberatung, der Pflege von Software-Paketen und der Veranstaltung überregionaler Nutzerworkshops. Die Geschäftsstelle des BremHLR ist an der Universität Bremen im Zentrum für Technomathematik angesiedelt.

Das BremHLR wurde am 1. Juli 2003 als Kooperation zwischen der Universität Bremen (UB), der Jacobs University Bremen (JUB, jetzt Constructor University, CUB) und dem Alfred-Wegener-Institut Helmholtz-Zentrum für Polar- und Meeresforschung (AWI) gegründet. Seit April 2008 ist die Hochschule Bremerhaven (HBHV) und seit Juli 2021 die Hochschule Bremen (HSHB) Kooperationspartner des BremHLR. Das Kompetenzzentrum wird von den beteiligten Kooperationspartnern sowie der Bremer Senatorin für Umwelt Klima und Wissenschaft (SUKW) anteilig finanziell getragen. Seit Januar 2014 ist die CUB als ideelles Mitglied beitragsfrei gestellt. Im Jahr 2021 konnte eine Weiterfinanzierung des BremHLR bis Ende 2024 sichergestellt werden. Die Einreichung eines Antrags zur Weiterführung als Bremer Landesnetzwerk ist für 2024 vorgesehen.

1.2 Struktur

Dem Lenkungsausschuss des BremHLR als oberstes beschlussfassendes und steuerndes Gremium gehörten in der Berichtsperiode folgende Vertreter der kooperierenden Einrichtungen an. Im Einzelnen sind dies:

- Prof. Dr. Alfred Schmidt (UB/Zentrum für Technomathematik ZeTeM)
- Prof. Dr. Stephan Frickenhaus (AWI/Rechenzentrum, UB/FB3)
- Prof. Dr. Ulrich Kleinekathöfer (CUB)
- Prof. Dr. Henrik Lipskoch (HBHV)
- Prof. Dr. A. Baars (HSHB)
- Dr. Astrid Sänger (SUKW, bis Juli 2023)

Die fachspezifische Betreuung der Projekte am Norddeutschen Verbund für Hoch- und Höchstleistungsrechnen (HLRN) sowie von Projekten an anderen nationalen Höchstleistungsrechenzentren wird von den Fachberatern des BremHLR geleistet, die ebenfalls den Einrichtungen der Kooperationspartner angehören. Im Berichtszeitraum waren folgende Fachberater tätig:

- Dr. Lars Nerger (AWI/Rechenzentrum, UB/ZeTeM, Leiter Geschäftsstelle)
- Thorsten Coordes (UB/ZARM)
- Dr. Achim Geleßus (CUB/CLAMV)
- Dr. Paul Gierz (AWI/Rechenzentrum)

Die Geschäftsstelle ist verantwortlich für die Organisation der Workshops (siehe Abschnitt Veranstaltungen) und die Unterstützung der Nutzer, insbesondere im Antragsverfahren. Das Sekretariat der Geschäftsstelle wird betreut von

- Katharina Müller.

2 Tätigkeitsprofil des BremHLR im Berichtszeitraum

2.1 Unterstützung der HLRN-Nutzung im Land Bremen

Ein Schwerpunkt der Aktivitäten des BremHLR lag auch in diesem Berichtszeitraum in der Unterstützung der Nutzung der beiden NHR-Systeme im HLRN. Neben der Tätigkeit von Prof. Dr. Stephan Frickenhaus als Mitglied des Technischen Beirats bestand die Unterstützung des HLRN durch das BremHLR hauptsächlich in der Fachberatung für Bremer Projekte an den beiden NHR-Rechnern im HLRN von der Antragstellung bis zur Begleitung rechenintensiver Projekte während der gesamten Projektlaufzeit.

Eine wesentliche Aufgabe im Berichtsjahr war die weitere Unterstützung der Bremer Nutzer des HLRN bei der effizienten Nutzung der HLRN-Hochleistungsrechner-Systeme. Hierbei war ein Fokus den stabilen Fortschritt der Projekte zu unterstützen.

2.2 Weitere Aktivitäten des BremHLR

Im Veranstaltungsjahr 2023 wurde vom BremHLR der *16. Workshop zur Einführung in die parallele Programmierung mit MPI und OpenMP* organisiert und durchgeführt. Mit 8 Teilnehmern war dieser Workshop wieder gut besucht.

Der Workshop wurde in der Zeit vom 9. bis 13. Oktober 2023 an der Universität Bremen abgehalten. Als Referent konnte wie bereits bei bisherigen Workshops Dr. Hinnerk Stüben vom Regionalen Rechenzentrum der Universität Hamburg gewonnen werden, der den Workshop gemeinsam mit dem BremHLR-Fachberater Dr. Lars Nerger leitete.

Die Fachberater des BremHLR beteiligten sich an dem Fachberaterworkshop des HLRN-Kompetenznetzwerks der im Jahr 2023 in Verbindung mit der ersten NHR-Konferenz im September 2023 abgehalten wurde. Bei dem Workshop wurden unterschiedliche Themen des HLRN-Betriebs und der Nutzerbetreuung besprochen. Durch den weiten Kontext des NHR-Verbunds wurden dieses Mal auch Fachberater der anderen NHR-Standorte einbezogen. Eine Übersicht über die Veranstaltungen ist in Abschnitt 4 zu finden.

Die Kanzlerin und der Konrektor der Universität Bremen beauftragten Stephan Frickenhaus und Torsten Coordes, sich in der Entwicklung eines Konzepts für einen nachhaltig betreibbaren und synergiestiftenden HPC-Cluster an der Universität Bremen einzubringen. Diese TIER3-Initiative der Universität Bremen soll mit Diensten und Infrastrukturen für ein geregeltes Datenmanagement verknüpft werden und sich so der Nachhaltigkeitsstrategie der Universität angliedern. Zu erneuernde Computing-Infrastrukturen an der Universität Bremen könnten nach und nach integriert werden. BremHLR soll dazu den technischen Austausch und die Fachberatung und Software-Bereitstellung – etwa auch im Data Science Center der UB – befördern, und als Brücke zu TIER2 (NHR) fungieren. Das Thema Datenmanagement für und neben HPC ist sowohl in der Landesinitiative Daten (BMBF-Kompetenzzentrum „DataNord“) mit bedacht, als auch in der Entwicklung auf TIER2-Ebene in NHR. Ebenso ist eine Orientierung neuer Bremer HPC-Nutzender im NHR eine Aufgabe von BremHLR.

Eine erste Skizze zur Fortführung von BremHLR ab 2024 wurde 2023 mit der behördlichen Vertretung diskutiert. Es ist beabsichtigt, BremHLR ab 2025 weiterhin durch Beiträge aus Universität Bremen, Senatorischer Behörde und AWI zu finanzieren.

3 Statistische Angaben zu den Bremer Höchstleistungsprojekten

Auch im Jahr 2023 wurden die NHR-Rechner des HLRN intensiv durch Bremer Projekte genutzt. Über das Jahr wurde auf den beiden NHR-Systemen des HLRN ein prozentualer Anteil von 12,7% an der gesamten genutzten Rechenleistung des HLRN erreicht. Dieses liegt deutlich über dem Finanzierungsanteil von etwa 7,9% des Landes Bremen am HLRN und ist eine weitere Steigerung der Nutzung im Vergleich zum Vorjahr. Über die gesamte Laufzeit der HLRN-IV Systeme wurde durch Bremer Projekte ein Anteil von 9% der verfügbaren Rechenzeit abgenommen.

Der stabile Betrieb der HLRN-IV Systeme ermöglicht eine stabile Nutzung durch die Bremer Wissenschaftler. Diese zeichnet sich durch eine hohe Nutzung von ca. 43 Mio. core-h pro Quartal aus. Hiervon weicht nur das dritte Quartal nach oben ab, in dem 57,5 Mio. core-h genutzt wurden. Insgesamt wurden im Jahr 2022 etwa 189 Mio. core-h[1] durch Bremer Projekte am HLRN abgenommen. Abbildung 3.1 zeigt die quartalsweise Nutzung der NHR-Rechner des HLRN durch die Bremer Projekte. Während der Umbauphase Ende 2019 und Anfang 2020 wurde die Nutzung nur unvollständig erfasst.

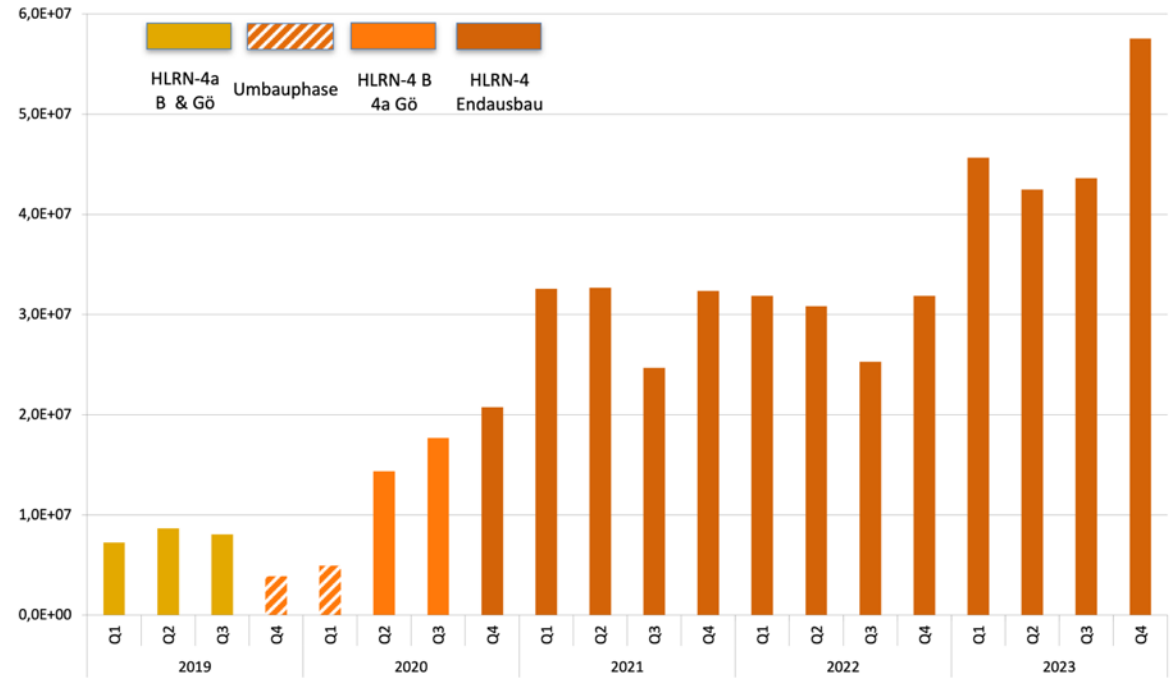

Abbildung 3.1: Quartalsweise Rechenzeitnutzung der Bremer HLRN-Großprojekte auf den HLRN-IV Systemen in der Einheit Prozessor-Stunden (core-h). Die Farben zeigen die Verfügbarkeit der unterschiedlichen Ausbaustufen des HLRN-Systems. Im vierten Quartal 2019 war der Betrieb durch die Umbaumaßnahmen beeinträchtigt und weitgehend nur das HLRN-IV System in Göttingen verfügbar. Im ersten Quartal 2020 waren die Nutzer vielfach mit Portierungsarbeiten befasst. Seit dem vierten Quartal 2020 befindet sich das HLRN-IV System im Endausbau.

Eine Übersicht zu allen vom BremHLR betreuten Projekten geben die Tabellen 3.1 und 3.2. Im Jahr 2023 wurden vom BremHLR 35 Projekte am HLRN betreut. 6 neue Projekte mit teilweise sehr großem Rechenzeitbedarf wurden im Jahr 2023 vom Wissenschaftlichen Ausschuss des HLRN bewilligt. 12 Projekte wurden im Berichtsjahr beendet.

[1]Seit dem vierten Quartal 2022 wird die Rechenleistung am HLRN in Prozessorkern-Stunden erfasst. Die Werte der früheren Quartale, die noch in der Norddeutschen Parallelrechner-Leistungseinheit erfasst wurden, wurden entsprechend dem Faktor 96/14=6,857 umgerechnet.

4 Veranstaltungen mit Beteiligung des BremHLR

43. Fachberater-Workshop

Veranstalter: ZIB

Datum: 20. - 21. September 2023

Ort: Berlin

Beschreibung: Der Workshop wurde im Kontext der ersten NHR-Konferenz durchgeführt. Hierbei gab es mehrere Networking-Sessions zu unterschiedlichen Fachthemen wie z. B. die Modellierung im Bereich Earth System Sciences. Des Weiteren wurden Aspekte des Rechnerbetriebs und des Nutzersupports besprochen.

Teilnehmende Institutionen: BremHLR (AWI), GWDG/Uni Göttingen, IOW, TU Hamburg, Uni Hamburg, Uni Kiel, Uni Potsdam, ZIB

16. BremHLR-Workshop *Einführung in die Programmierung mit MPI und OpenMP*

Veranstalter: BremHLR

Datum: 9. – 13. Oktober 2023

Ort: Universität Bremen

Beschreibung: In dem Workshop wurden die Grundlagen der parallelen Programmierung vermittelt. Der Schwerpunkt lag auf den Programmiermodellen MPI und OpenMP. Praktische Übungen bildeten einen wesentlichen Teil des Workshops.

Teilnehmer: 8

Referenten: Dr. Hinnerk Stüben (Regionales Rechenzentrum der Universität Hamburg) und Dr. Lars Nerger (BremHLR).

Teilnehmende Institutionen: AWI, Uni Bremen, Hochschule Bremerhaven

Tabelle 3.1: Übersicht neu begonnener Bremer HPC-Projekte, die innerhalb des Berichtszeitraums vom BremHLR betreut wurden. Status: E = Erstantrag, X = Projektende in 2023; kcore-h: Kontingent im Jahr 2023 in tausend core-h.

Kennung	Projektleiter	Institut	Laufzeit	kcore-h	Status
hbi00062	Prof. Dr. U. Fritsching	UB/FB4	III/23 – II/24	930	E
hbk00097	Prof. Dr. T. Kanzow	AWI & UB	I/23 – IV/24	4800	E
hbk00098	Dr. A. Rozanov	UB/IUP	I/23 – I/24	8311	E
hbk00099	Prof. Dr. T. Kanzow	AWI & UB	II/23 – I/24	6248	E
hbp00075	Dr. A. Pahedath	UB/BCCMS	I/23 – IV/23	8380	EX
hbp00076	Dr. S. Amiri	UB/BCCMS	I/23 – IV/24	17200	E
hbp00081	Dr. Z. Zhou	UB/BCCMS	III/23 – IV/23	751	EX

Tabelle 3.2: Von BremHLR betreute fortgeführte Bremer HPC-Projekte. Status: F = Fortsetzung, X = Projektende in 2023; kcore-h: Kontingent im Jahr 2023 in tausend core-h.

Kennung	Projektleiter	Institut	Laufzeit	kcore-h	Status
hbb00001	Prof. Dr. L. Colombi Ciacchi	UB/BCCMS	III/20 – II/24	2152	F
hbb00002	Dr. S. Köppen	UB/BCCMS	III/22 – II/24	9744	F
hbb00003	Dr. S. Köppen	UB/BCCMS	IV/22 – III/24	2000	F
hbc00045	Prof. Dr. T Neudecker	UB/Chemie	II/20 – III/24	31688	F
hbc00049	Dr. P. Guo	UB/BCCMS	I/21 – I/23	220	X
hbc00056	Dr. M. Fischer	UB/Geo	III/21 – III/23	1250	X
hbc00057	Dr. M. Delle Piane	UB/BCCMS	III/21 – I/23	274	X
hbc00061	Dr. L. Moskaleva	UB/Chemie	IV/21 – III/24	5786	F
hbc00062	Dr. M. Fischer	UB/Geo	I/22 – IV/24	2200	F
hbi00036	Prof. Dr. U. Fritsching	UB/FB4	II/17 – II/23	597	X
hbi00037	Prof. Dr. U. Fritsching	UB/FB4	II/17 – II/24	924	F
hbi00055	Dr. D. Feldmann	UB/ZARM	II/22 – I/23	1372	X
hbi00056	Prof. Dr. A. Baars	HSB	II/22 – I/23	1715	X
hbi00057	Dr. S. Köppen	UB/BCCMS	III/22 – II/23	692	X
hbi00059	Prof. Dr. L. Colombi Ciacchi	UB/BCCMS	IV/22 – IV/23	6750	X
hbk00059	Prof. Dr. M. Schulz	UB/MARUM	III/17 – III/24	8404	F
hbk00062	Dr. A. Rozanov	UB/IUP	IV/17 – III/24	2100	F
hbk00083	Prof. Dr. B. Rost	AWI & UB	II/21 – III/24	3179	F
hbk00084	Prof Dr. A. Bracher	AWI & UB	IV/21 – IV/23	1388	X
hbk00085	Prof. Dr. M. Schulz	UB/MARUM	IV/21 – II/24	13068	F
hbk00090	Prof. Dr. M. Schulz	UB/MARUM	III/22 – I/24	38310	F
hbk00094	Prof. Dr. B. Rost	AWI & UB	III/22 – II/24	17435	F
hbk00095	Dr. L. Nerger	AWI	III/22 – II/24	28334	F
hbk00096	Prof. Dr. M. Schulz	UB/MARUM	IV/22 – IV/24	6912	F
hbp00041	Prof. Dr. C. Lämmerzahl/ Prof. Dr. S. Rosswog	UB/ZARM	I/17 – I/23	412	X
hbp00058	Prof. Dr. U. Kleinekathöfer	Jacobs U	II/20 – II/24	3484	F
hbp00067	Dr. Y. Liu	UB/BCCMS	IV/20 – I/24	1272	F
hbp00068	Prof. Dr. U. Kleinekathöfer	Jacobs U	IV/20 – IV/24	8820	F
hbp00072	Dr. A. Rozanov	UB/IUP	I/22 – II/24	8412	F

5 Projektberichte[2]

5.1 *hbb00001:* Exploring the conformational phase space of N-linked glycans using enhanced molecular dynamics and sketch-map analysis

HLRN-Projektkennung:	hbb00001
Laufzeit:	IV/2022 – I/2024
Projektleiter:	Prof. Dr.-Ing. Lucio Colombi Ciacchi
Projektbearbeiter.	Isabell Louise Grothaus
Institut / Einrichtung:	Faculty Production Engineering

Overview

Various enzymes in the endoplasmic reticulum (ER) and Golgi process post-translationally added N-glycans in eukaryotic cells. Transitioning from high-mannose to complex N-glycans involves trimming Man residues by mannosidases. Cancers like colon, skin, and breast cancers exhibit elevated complex N-glycans on cell surfaces, linked to metastasis growth and disease progression. Inhibiting key glycosylation enzymes, such as α-mannosidase II (GMII), reduces complex N-glycan formation, potentially hindering tumor growth and metastasis. However, inhibitors like swainsonine have side effects, possibly due to lysosomal α-mannosidase inhibition. Despite efforts to develop selective inhibitors, clinical application remains elusive. Understanding monosaccharide pucker distortion in glycoside hydrolase (GH) transition states is crucial for inhibitor development. GHs exhibit diverse catalytic mechanisms; addressing this, we used GMII as a model due to its well-studied catalysis and crystal structure (PDB entry: 3CZN). Our focus includes the substrate's structural role, mainly how pucker distortion is induced.

Results

GMII, a member of GH family 38, operates in the medial Golgi, catalyzing the removal of two Man residues from glycan M5G0, converting it to M3G0. The enzyme's binding site comprises anchor, holding, and catalytic regions, with specific amino acids facilitating substrate orientation and hydrolysis. GMII's catalytic process follows a retaining mechanism, involving conformational changes in the substrate from a 4C1 pucker to a B2,5/1S5 pucker before reaching the transition state. The catalytic site features a stably bound Zn ion, coordinated by specific amino acids. Quantum mechanics/molecular mechanics (QM/MM) calculations elucidate the detailed reaction mechanism, emphasizing the dissociation of the glycosidic bond and the covalent bond formation between the substrate and D204, exhibiting an oxocarbenium ion-like character in the transition state.

This study delves into the glycan conformation at the reaction's onset, exploring how the terminal Man residue undergoes distortion. N-glycans, known for flexibility, adopt various conformations. The prevailing glycan conformers in GMII's binding site, crucial for understanding substrate interactions, are investigated using our REST-RECT methodology [1]. This comprehensive exploration contributes to understanding GMII's catalytic mechanism, paving the way for potential therapeutic insights.

[2] Für den Inhalt der Projektberichte sind ausschließlich die genannten Projektleiter bzw. die Projektbearbeiter verantwortlich.

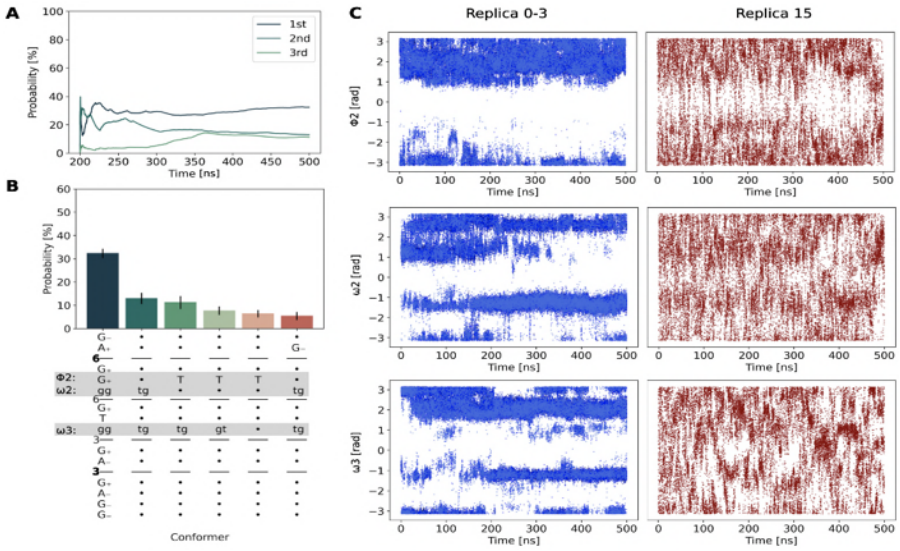

Figure 1: Convergence of the M5G0 conformer distribution. A) Cumulative average of the three most populated conformer clusters according to panel B. B) Conformer distribution for M5G0. The conformer string is given on the x-axis. The gray boxes highlight key conformational differences between conformers. For A and B, data points recorded up to 200 ns of simulation were discarded, as the REST-RECT sampling required lead time to take action. 75000 datapoints were analyzed. C) Torsion angle fluctuations of φ 2, ω 2 and ω 3 over the simulation time for replica 0-3 and 15, respectively.

The REST-RECT simulation, conducted for 500 ns per replica, accumulated 8 µs of sampling time. The chosen replica exchange parameters were validated by monitoring exchanges across the replica ladder. These settings produced a converged conformer distribution for M5G0 in GMII's catalytic site (Figure 1A). The cumulative average of the three most populated conformers flattened after 350 ns, excluding the initial 200 ns to allow metadynamics potentials to take effect.

The conformer histogram (Figure 1B) revealed variations mainly in the second φ and both ω angles, akin to free glycans in solution. In this protein-glycan simulation, temperature and bias factor ranges were shorter due to convergence challenges. Optimal results were achieved with a maximum temperature of 550 K and a bias factor limited to six, ensuring comprehensive sampling of all torsion angles in the highest replica (Figure 1C). While the distributions in the lowest replicas differed due to reduced bias potential, frequent exchanges maintained mixing of relevant conformers from higher to lower replicas.

Outlook

We were able to apply our previously developed REST-RECT method to the protein-glycan system ManII – M5G0, optimizing the algorithm to achieve convergence of glycan conformers in the catalytic site, within the computational restraints. This benchmark allows for future simulations of e.g. ManII mutants, to monitor the change in glycan conformer distributions.

Publications

[1] I. L. Grothaus, G. Bussi, L. Colombi Ciacchi, *Exploration, representation and rationalization of the conformational phase-space of N-glycans*, Journal of Chemical Information and Modelling, 62(20), 4992–5008, 2022

5.2 *hbb00003:* Unravelling the mechanism of ion transport of the HumanP2X4R receptor channel

HLRN Project ID:	hbb00003
Run time:	I/2023 – I/2024
Project Leader:	Dr. Susan Köppen
Project Scientists:	Aparna Sai Malisetty
Affiliation:	Hybrid Materials Interfaces Group Faculty of Production Engineering University of Bremen

Overview

Purinergic (P2X) receptors are a family of seven members, P2X1-P2X7 and are activated by ATP. They have a peculiar trimeric structure formed by non-covalent interactions of the subunits. The conformational change of P2XR occurs with the binding (open state) or non-binding (closed state) of extracellular ATP shown in Figure 1A. To date, many experimental studies have focused on the therapeutic deactivation of this pain signaling receptor. Nevertheless, there are many gaps in the knowledge of the molecular mechanism of the ion transport pathways.

In the previous project entitled “Identification of residues involved in homotrimeric stabilization and function of Human P2X4R(hP2X4R) receptor channel by molecular dynamic simulations” addressed the key residues for stabilization or functionalization were identified. However, these simulations were limited to the closed state models (without ATP ligand). In this project entitled “Unravelling the mechanism of ion transport of the HumanP2X4R receptor channel”, the role of residue Arg309 in the activation of channel was investigated. We simulated open-state models with ATP ligand at the three binding sites (Figure 1B).

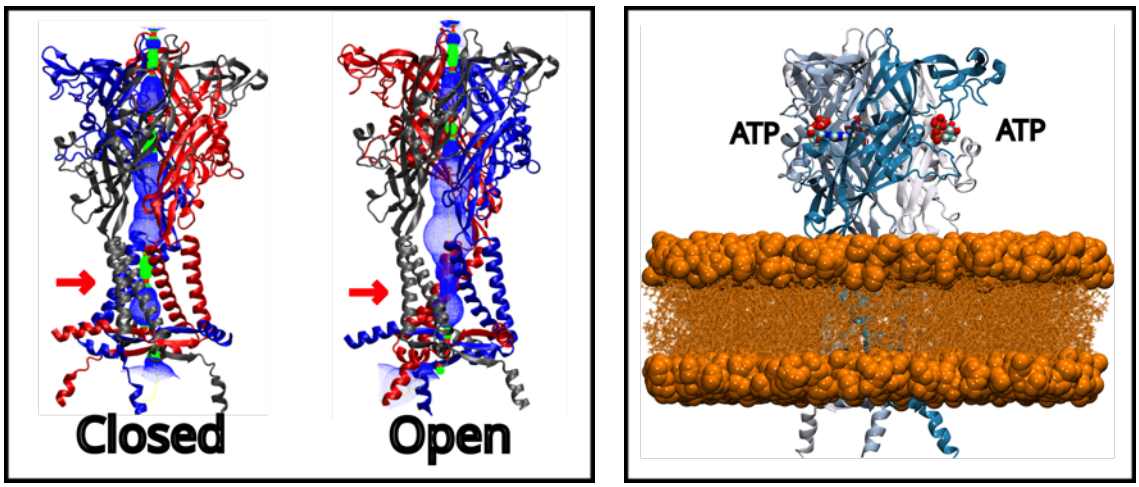

Figure 1: (A) HP2X4R conformational states. The channel pore is shown in blue dots and is obtained using the HOLE program. The different colors of the pore represents red: inaccessible to water (<1.15Å), green: accessible to water(1.15-2.3Å) and blue: >2.3Å radius. In closed state, when no ATP is bound, the pore is narrowed and no ion can pass through the channel, in the open state, when ATP is bound, the pore opens and ions can pass thorugh the channel. (B) HP2X4R simulation setup in the open-state. The open state is simulated with ATP at three binding sites and inserted into a POPC lipid bilayer membrane (shown in orange). Water and ions are not shown here.

Results

The experiments showed a significant inactivation of the hP2x4R channel by the point alanine mutation of Arg309. In the first phase of the project, an open-state model without ATP was simulated to determine whether the simulation time would be sufficient for the conformational change to the closed-state structure. It was observed that the open-state without ATP ligand changes to a closed-state within the simulation time.

In the second phase, we simulated a point-alanine mutation of the Arg309 model in the open state and a control structure in the open state without mutation. Both structures have ATP ligand at the three binding sites. We saw that with the mutation of the Arg309 lead to closed state channel even with ATP ligand as shown in Figure 2.

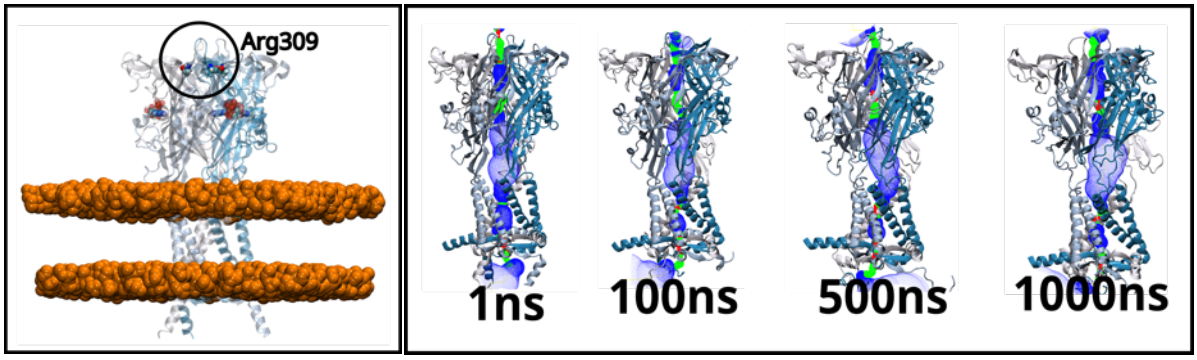

Figure 2: (A) Location of Arg309 on hP2X4R. (B) Open to closed-state of the mutant. The conformational change of the channel in the open-state channel to closed-state during the simulation time even with ATP ligand at the binding site. The narrowing of the pore can be seen over time

Outlook

Further simulations are planned to investigate different mutations that have the same effect as Arg309. In the future, electrophysiological simulations will also be carried out.

Presentations

1. A. Malisetty, *Identification of residues involved in homotrimeric assembly of the human P2X4 receptor by simulations and site-directed mutagenesis*. Annual meeting of the American Biophysical Society, San Diego (USA), February 18-22, 2023

5.3 *hbc00045:* Rupturing Materials in Electric Fields

HLRN Project ID:	hbc00045
Run time:	II/2020 – II/2024
Project Leader:	Prof. Dr. Tim Neudecker
Project Scientists:	Dr. Sourabh Kumar, M. Sc. Tarek Scheele, M. Sc. Alexander Dellwisch
Affiliation:	University of Bremen Institute for Physical and Theoretical Chemistry Leobener Str. 6 D-28359 Bremen

Overview

In mechanochemistry, forces are applied to initiate chemical reactions. This approach can be used in the production of mechanochromic materials, which change their color when a threshold stretching force is applied. In the case of a polymer, for example, a molecular subunit, the so-called mechanophore, is embedded in the polymer backbone. Upon application of stretching forces, the mechanophore changes its structure, e.g., via bond-rupture or cis-/trans-isomerization, which can be accompanied by color changes. The applications of this approach are immense, including optical strain detection in the construction industry, tamper-proof packaging, and self-healing materials.

Oriented external electric fields (OEEFs) have been used to catalyze a number of reactions by lowering the energy of a transition state if a zwitterionic resonance structure, which is favored in an OEEF, is present in the transition state (cf. Figure 1). Examples of reactions induced by OEEFs include enzymatic processes, isomerizations and Diels-Alder reactions. Moreover, it has been demonstrated that OEEFs reduce the bond dissociation energy of σ- and π-bonds and allow the switching of typically homolytic to heterolytic bond rupture processes.

In this project, mechanochemistry is coupled to the application of OEEFs in order to reduce the rupture forces of mechanophores in mechanochromic materials. While it is far from straightforward to conduct mechanochemical experiments in OEEFs due to the difficulty of controlling the relative orientation of the substrate and the electric field, computational chemistry offers the opportunity to rapidly screen a variety of mechanochemical reactions in OEEFs. The focus in this project lies on determining the rupture forces required to achieve the color switching process, using state-of-the-art computational methods.

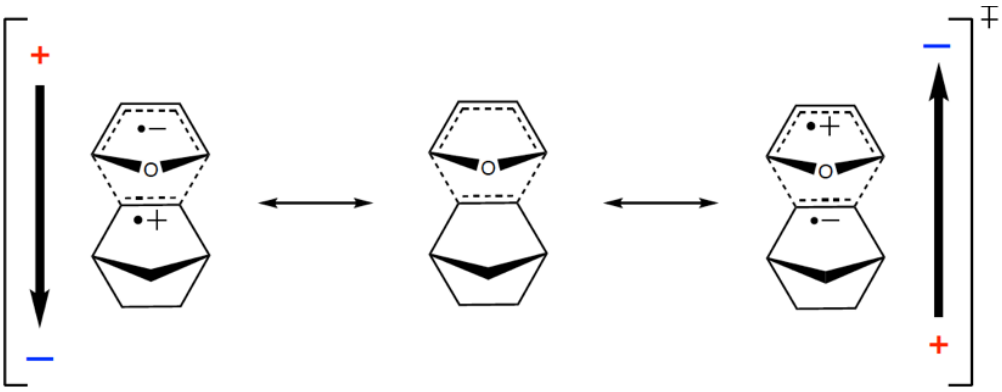

Figure 1: Schematic representation of the resonance structures in the transition state of a Diels-Alder reaction, which can be energetically favored in an oriented external electric field (OEEF).

Results

In the previous phases of the project hbc00045, we conducted a thorough benchmark of density functionals that reproduce energetic and geometric changes of molecules induced by strong oriented external electric fields (OEEFs). High-level benchmark data was provided by CCSD[T]. We found that the rung of the density functional on Jacob's Ladder does not correlate with its reliability in predicting energetic and geometric properties of molecules in OEEFs, which was surprising, but, beneficially, provided us with proof that computationally inexpensive functionals can be used for conducting the rest of the calculations in hbc00045. We finished the manuscript reporting on the results of the benchmark and submitted it to a journal. In 2023, we addressed all of the reviewers' comments by running additional calculations. The article has been published. [1]

In the second phase of the project, we performed calculations on the mechanical properties of a model mechanophore in an OEEF. The full set of calculations on three mechanophores (spiropyran, benzocyclobutene and a model molecule featuring a disulfide bond) in a polymer chain were finished and the effect of the relative orientation of the electric field w.r.t. the scissile bond was tested (Figure 1). The results agreed well with our hypothesis: OEEFs that are aligned with the scissile bond weaken the mechanophore and decrease the rupture force. The extent of the weakening correlates well with the alignment of the OEEF with the scissile bond, and the weakening effects of OEEFs and mechanical force amplify one another. In the past year, we conducted all remaining calculations and completed the manuscript detailing our findings. The article has been published. [2]

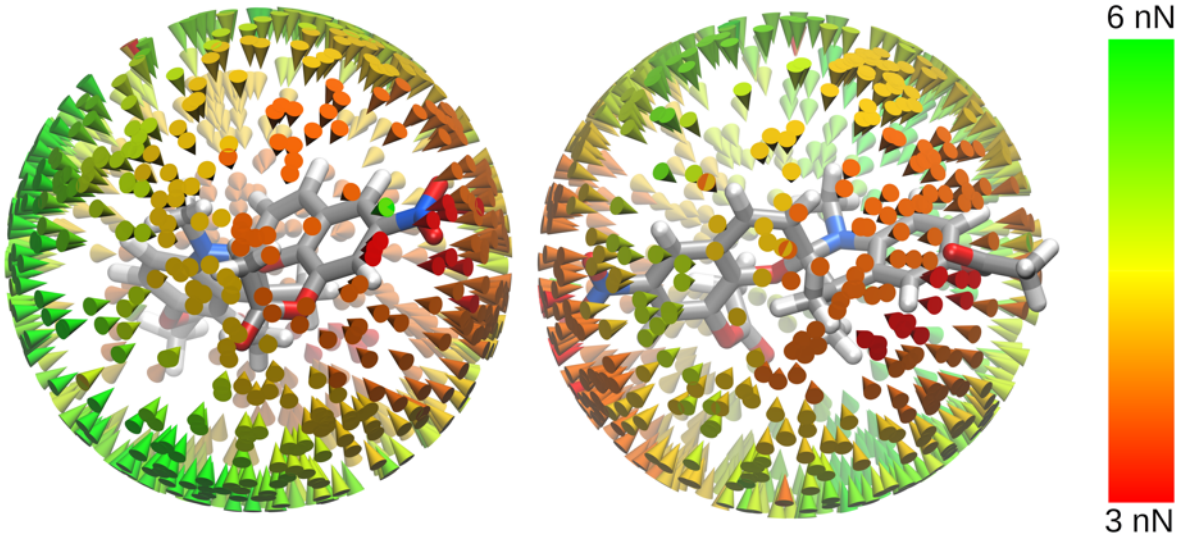

Figure 1: Dependence of the rupture force of the scissile bond in spiropyran on the orientation of the OEEF (strength: 0.01 a.u.). Colored cones represent directions of the OEEF. Red cones signify maximum weakening of the mechanophore, whereas green cones denote a small influence of the OEEF on the rupture force.

To study the crucial impact of the chemical environment on the rupture behavior of mechanophores, we constructed a multiscale mechanochemical model for the activation of spiropyran (SP)-doped polymers in a complex polymer network (PMMA). Using much of the computational power granted to us in 2022 and 2023, we completed the calculations on the mechanical properties of the functional polymer. We found that, for an efficient activation of SP, the polymer chain incoporporating the mechanophore needs to be fully elongated. The manuscript detailing our findings has been published [3].

Based on these findings, we investigated more complex SP-doted PMMA systems where the equilibration routine was improved by using an initial random-walk algorithm which leads to a

higher entanglement of the polymer chains. In addition to the polymer system already examined, a system with twice the chain length as well as another system with twice the number of chains were set up. Each system yields the correct experimental density after equilibration. Subsequently, tensile deformation simulations were performed using an experimental strain rate of 5 · 108 s-1 while the calculated ranges of Young's modulus are in agreement with experimental results. In general, we found out that both an increase in the chain length as well as in the number of chains leads to more SP activations during deformation. In addition, we tend to obtain activations at lower strain especially for the system containing more chains. These results can be attributed to an enhanced chain entanglement in both cases, which leads to an improved force transduction from the polymer backbone to the mechanophore. Furthermore, with an increased number of chains SP activation is statistically more likely. Besides tensile deformation we also performed uniaxial compression simulations for all systems. SP activations were observed in the plastic region at high compressive strain. As with deformation, both more chains as well as a higher chain length led to earlier and more frequent activations. Beyond this, another bond length parameter was implemented in our published polymer system to simulate bond ruptures in the polymer backbone. During deformation no bond breaks were observed where uniaxial compression results in ruptures at high compressive strain. In addition, we also simulated hydrostatic compression while no mechanophore activations were obtained in any of the three systems. These results will be disseminated in a future publication.

Outlook

Within the next phase of the project, the focus will shift towards investigating dynamic effects of OEEFs on mechanophores on a smaller scale, while also continuing to pursue the use and further refinement of the multiscale model for further investigations.

The next objective of the project involves investigating the effects of OEEFs on mechanophores at different temperatures. Using ab initio molecular dynamics (AIMD) simulations based on density functional theory (DFT), we plan to investigate the dissociation point of mechanophores in OEEFs of different strengths at different temperatures, with and without mechanical stress. Our goal is to gain insights into the behavior of a mechanophore's scissile bond at higher temperatures, and into how the OEEF weakens the bond as the temperature increases. This will give us an understanding of the interplay between mechanical force, electric fields, and temperature, which will be crucial for further studies of the dynamic behavior of mechanophores embedded in polymer chains. The calculations required for this objective are currently being performed and are expected to finish by the end of the first quarter of 2024.

Concerning the refinement of the multiscale simulation protocol for SP-doped PMMA, in the next phase of this project three main objectives will be pursued:

1) Performing deformation and compression simulations for several different starting structures of each of the three SP-doted PMMA systems.

2) Performing coarse-grained MD deformation and compression simulations on SP-doped PMMA systems.

3) Restoring the activated mechanophores into its deactivated form by applying pressure to the stretched polymer system after deformation.

The first goal we set is to increase the statistical reliability of our results and to identify outliers. Subsequently, in order to take our simulations to a larger scale and enhance their comparability to experiments we will switch from all-atom models to coarse-grained (CG) models. In this case the PMMA polymer backbone will be represented by CG beads, while we continue to use our parameterized all-atom force field for the mechanophores. Regarding the third objective the baromechanical cycle for repeated activation of SP and deactivation of MC by alternating

mechanical stretching and hydrostatic compression has already been shown in the gas phase. In the next step we will try to transfer this cycle to our SP-doped polymer systems by performing alternating deformation and compression simulations.

Publications

1. T. Scheele, T. Neudecker, *Investigating the accuracy of density functional methods for molecules in electric fields*, J. Chem. Phys. 2023, 159, 124111.

2. T. Scheele, T. Neudecker, *Using oriented external electric fields to manipulate rupture forces of mechanophores*, Phys. Chem. Chem. Phys. 2023, 25, 28070–28077.

3. S. Kumar, B. Demir, A. Dellwisch, L. Colombi Ciacchi, T. Neudecker, Macromolecules 2023, 56, 8438-8447.

Presentations

1. T. Scheele, *Using Oriented External Electric Fields to Manipulate Rupture Forces of Mechanophores*, 59th Symposium on Theoretical Chemistry, Zürich, September 2023

5.4 *hbc00056:* Towards an atomic-level understanding of the interaction of probe molecules with acid sites in zeolites

HLRN Project ID:	hbc00056
Run time:	Initial: III/2021 – II/2022, continuation III/2022 – II/2023
Project Leader:	PD Dr. Michael Fischer[1]
Project Scientists:	PD Dr. Michael Fischer[1], Carlos Bornes[2]
Affiliation:	1: Crystallography & Geomaterials Research Group, Faculty of Geosciences, University of Bremen; Bremen Center of Computational Materials Science, University of Bremen; MAPEX Center for Materials and Processes, University of Bremen, Bibliothekstraße 1, 28359 Bremen 2: CICECO, Aveiro Institute of Materials, Department of Chemistry, University of Aveiro, 3810-193 Aveiro, Portugal; now at: (Nano)Materials Modeling Group, Department of Physical and Macromolecular Chemistry, Charles University Prague, Hlavova 8, 12800 Prague, Czech Republic

Overview

The adsorption of probe molecules like ammonia, pyridine, or trimethylphosphine oxide is a common technique to characterize protonated zeolites, which are important solid acid catalysts. However, recent work has shown that the interpretation of experimental results is less straightforward than commonly assumed, because more than one probe molecule can interact with a single acid site. In this project, electronic structure calculations in the framework of density functional theory (DFT) and DFT-based molecular dynamics simulations are performed to shed light on the interaction between protonated zeolites and probe molecules. The calculations are carried out in close collaboration with experimental partners, who employ advanced nuclear magnetic resonance (NMR) spectroscopy to investigate these systems.

Scientific background

Zeolites are inorganic tetrahedral framework materials exhibiting an intrinsic porosity. They are used as solid acid catalysts in large-scale industrial processes, with the economically most significant application being the fluid catalytic cracking of heavy hydrocarbons, a key step in the processing of crude oil.[1,2] Highly siliceous zeolites, the most important zeolite catalysts, contain relatively small amounts of tetrahedrally coordinated aluminum atoms, the remainder of the tetrahedral sites being occupied by silicon. In protonated zeolites, the negative framework charge is balanced through protons bonded to framework oxygen atoms of the AlO4 tetrahedra. The overall catalytic activity of these zeolites strongly depends on the location, amount, and acid strength of the framework protons, which act as Brønsted acid sites. Hence, a comprehensive characterization of the acid site properties is pivotal to develop increasingly active and selective catalysts.[3,4]

Probe molecules like ammonia (NH3), pyridine (C5H5N), and trimethylphosphine oxide (TMPO, C3H9OP) have been widely used to study the acid properties of zeolites. Studies employing probe molecules identified “fingerprint” vibrational modes (in vibrational spectroscopy) or distinct chemical shifts (in NMR spectroscopy) that were commonly assigned to probe molecules interacting with framework protons of different acid strength.[3,4] However, computational studies have shown consistently that the deprotonation energy of zeolites, often

considered as the “true” measure of acid strength, is largely independent of the acid site location and the zeolite framework.[5,6]

This project aimed to enhance the atomic-level understanding of the interaction of protonated zeolites with ammonia, pyridine, and TMPO through DFT calculations. To study the impact of the local environment, two zeolites with channels of different size were included in the investigation (MFI and MOR, see Figure 1), and different positions of framework Al atoms and charge-balancing protons were considered for each of them. In the first project phase, DFT structure optimizations, which delivered equilibrium structures of adsorption complexes and adsorption energies, were complemented by DFT-based ab initio molecular dynamics (AIMD) simulations to include temperature effects. The second phase was aimed at a DFT-based prediction of NMR chemical shifts and vibrational modes and their comparison to experimental data. While the computational part of the project is finished, experiments are still being carried out by the collaboration partners at CICECO, Aveiro Institute of Materials, Portugal (Dr. Luís Mafra, Prof. Dr. João Rocha).

Funding of the project scientists was provided through a Heisenberg grant to PD Dr. Michael Fischer (Deutsche Forschungsgemeinschaft project no. 455871835, Fi1800/6-1), and through a PhD scholarship from the Portuguese Fundação para a Ciência e Tecnologia (FCT) to Carlos Bornes (ref. PD/BD/142849/2018).

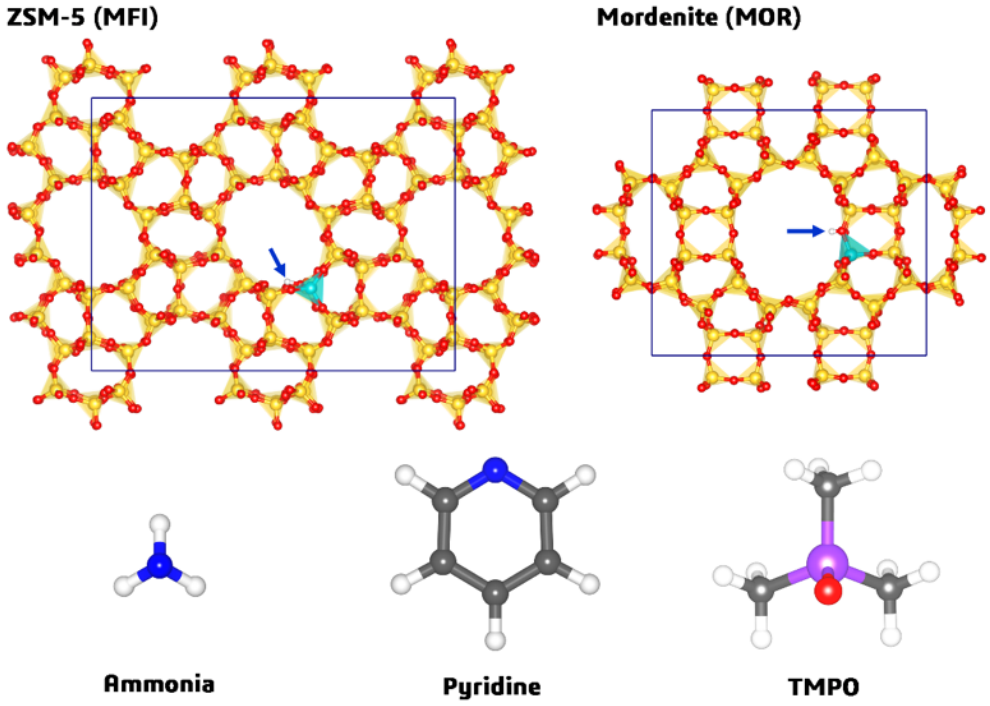

Figure 1: Zeolites and probe molecules considered in this investigation. Top: MFI contains a two-dimensional system of channels formed by ten-membered rings of TO4 tetrahedra (10MRs), MOR contains a one-dimensional system of 12MR channels. Yellow = silicon, turquoise = aluminum, red = oxygen, white = hydrogen. Positions of the framework protons are emphasized by arrows. Bottom: Probe molecules. Blue = nitrogen, grey = carbon, purple = phosphorus. Note that probe molecules are not shown on the same scale as the zeolite crystal structures.

Project results

1:1 complexes of ammonia, pyridine, and TMPO in the different zeolite models were constructed (1:1 = one probe molecule per acid site) and DFT-optimized adsorption complexes were compared to structures that were subjected to a short AIMD simulation (~10 picoseconds, temperature: 150 °C) prior to optimization. For all three probe molecules, the interaction with

the acid site resulted in framework deprotonation, i.e., an abstraction of the proton from the framework and formation of a cationic species in the pores. Whereas only limited movement was observed in AIMD simulations of pyridine- and TMPO-containing systems, the ammonium cation was found to diffuse away from the acid site. Calculations for 2:1 complexes showed larger differences between structures obtained from DFT optimizations and from AIMD simulations, as shown for the case of pyridine in **Figure 2**. In some cases, the formation of probe molecule dimers was only captured when employing the computationally more demanding AIMD simulations, indicating the necessity to run such simulations for a realistic modelling of dimer formation.

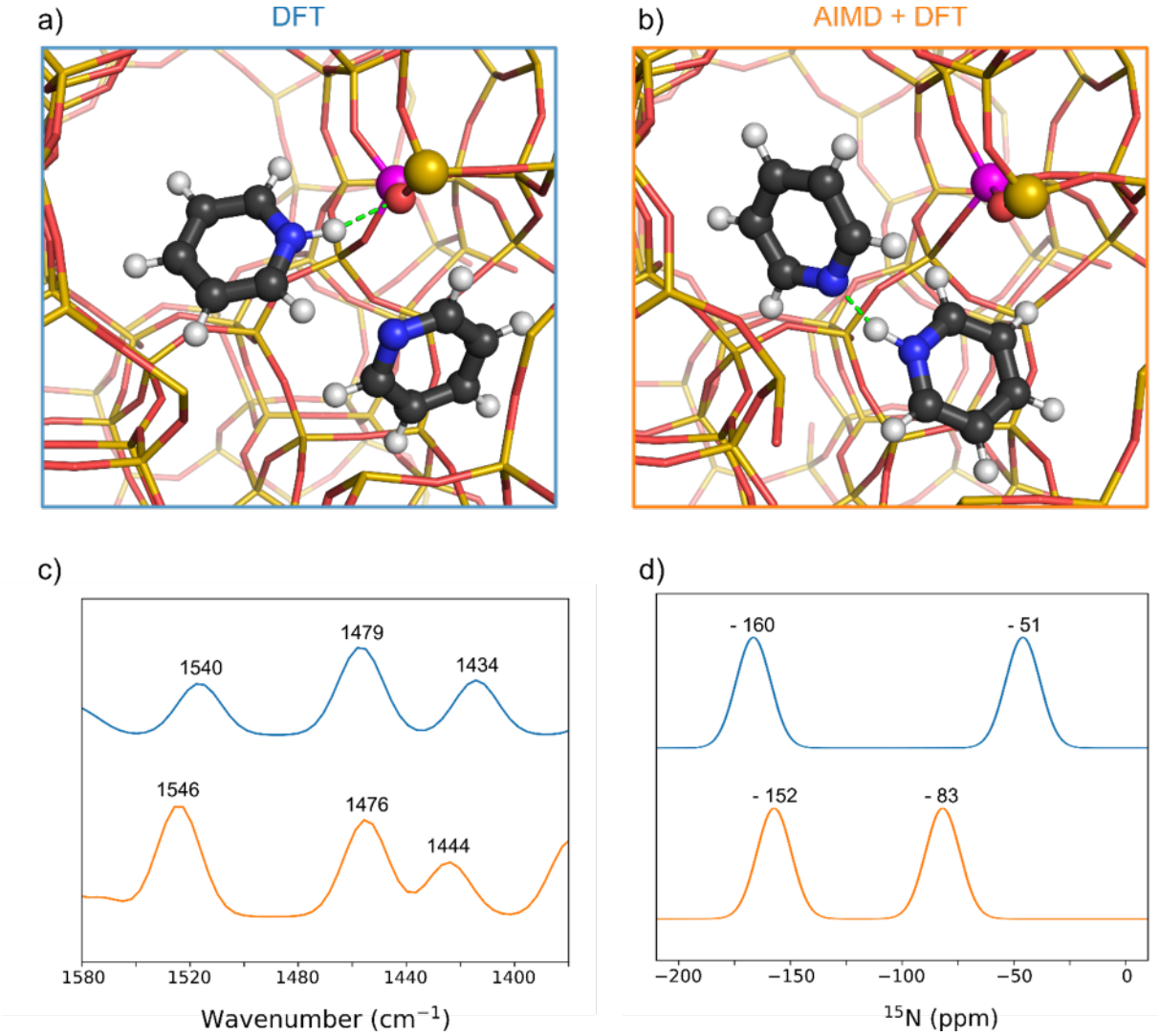

Figure 2: 2:1 complexes of pyridine in MFI model with Al at the channel intersection. a) Complex consisting of pyridinium cation and free pyridine molecule obtained from DFT optimization, b) pyridinium-pyridine dimer obtained from AIMD simulation and subsequent optimization, c) calculated IR spectra, d) calculated 15N NMR spectra. Spectra obtained for complexes shown in a) and b) are displayed as blue and orange curves, respectively.

In the second project phase, a portfolio of DFT-based methods was used to predict 31P and 15N chemical shifts of low-energy adsorption complexes. Calculations of 31P chemical shifts in TMPO-loaded MFI and MOR corroborated that the chemical shift is sensitive to the Brønsted acid site location.[P1] Computations for zeolites loaded with ammonia and pyridine also predicted an influence of the acid site location on the 15N chemical shift. However, due to the low natural abundance of 15N, the number of experimental NMR studies is very limited. One investigation of MFI loaded with 15N-enriched pyridine suggested that a broad 15N resonance

at −176 ppm arises from the interaction with Brønsted acid sites.[7] This value agrees very well with our DFT value of −173 ppm, obtained for a 1:1 complex where the acid site is at the MFI channel intersection. Another study using 15N-enriched ammonia loaded onto MFI reported ^{15}N resonances in the range of −360 to −368 ppm.[8] While DFT-computed values are similar (−365 to −373 ppm), they are more dependent on the inclusion/neglect of dynamics than on the location of the acid site.

In addition to NMR chemical shifts, vibrational modes of 1:1 and 2:1 complexes were also predicted using DFT calculations. For a representative zeolite model, Figure 2 shows the equilibrium structures of 2:1 complexes obtained from a DFT structure optimization (2 a) and from an AIMD simulation followed by an optimization (2 b), as well as the predicted IR spectra (2 c) and 15N chemical shifts (2 d). As for TMPO-loaded systems, the use of AIMD simulations is crucial to capture the formation of dimeric species in pyridine-loaded zeolites. Our results suggest that IR spectroscopy, commonly used to study the adsorption of pyridine onto zeolites,[9,10] is not an effective way to distinguish between a single pyridinium cation having a free pyridine molecule in the vicinity (Figure 2 a) and a pyridinium-pyridine dimer (Figure 2 b). In contrast, 15N NMR can distinguish between these species quite easily, with the 15N chemical shift jumping from −51 ppm in the free pyridine molecule to −83 ppm in the hydrogen-bonded pyridine in the dimer.

Outlook

At present, further DFT data generated for pyridine- and NH_3-loaded zeolites are being analyzed. Due to the lack of literature data for ^{15}N chemical shifts of pyridine or ammonia adsorbed in zeolites, the collaborators at CICECO will perform ^{15}N NMR measurements using ^{15}N-enriched probe molecules in order to allow for a comparison of the DFT results to experiment. The development of a specially designed cell to facilitate the adsorption of controlled amounts of pyridine onto NMR rotors is ongoing. Furthermore, a more comprehensive analysis of the DFT-computed vibrational spectra can be complemented by *in-situ* infrared spectroscopy.

Publications

P1 C. Bornes, M. Fischer, J. A. Amelse, C. F. G. C. Geraldes, J. Rocha, L. Mafra, *What Is Being Measured with P-Bearing NMR Probe Molecules Adsorbed on Zeolites?*, J. Am. Chem. Soc. 143, 13616–13623 (2021)

P2 C. Bornes, *NMR study of zeolites' acid sites using molecular probes*, PhD Thesis, University of Aveiro (2023), weblink: http://hdl.handle.net/10773/39616

References

[1] G. Busca, Chem. Rev. 107, 5366–5410 (2007)

[2] A. Primo, H. Garcia, Chem. Soc Rev. 43, 7548–7561 (2014)

[3] L. E. Sandoval-Diaz, J. A. González-Amaya, C. A. Trujillo, Microporous Mesoporous Mater. 215, 229–243 (2015)

[4] G. Busca, Microporous Mesoporous Mater. 254, 3–16 (2017)

[5] A. J. Jones, E. Iglesia, ACS Catal. 5, 5741–5755 (2015)

[6] P. Deshlara, E. Iglesia, Chem. Commun. 56, 7371–7398 (2020)

[7] T. Xu, N. Kob, R. S. Drago, J. B. Nicholas, J. F. Haw, J. Am. Chem. Soc. 119, 12231–12239 (1997)

[8] V.M. Mastikhin, S.V. Filimonova, J. Chem. Soc., Faraday Trans. 88, 1473–1476 (1992)

[9] M. Castellà-Ventura, Y. Akacem, E. Kassab, J. Phys. Chem. C 112, 19045–19054 (2008)

[10] T.D. Klots, Spectrochimica Acta A: Mol. Biomol. Spectr. 54, 1481–1498 (1998)

5.5 *hbc00061:* Studying the Wet and Dry CO Oxidation on Nanoporous Gold Using Static DFT Computations and AIMD Simulations

HLRN Project ID:	hbc00061
Run time:	IV/2022 – III/2023
Project Leader:	Dr. Lyudmila Moskaleva
Project Scientists:	Shikun Li, Lenard Carroll
Affiliation:	Universität Bremen, Institut für Angewandte und Physikalische Chemie, Leobener Str. UFT, 28359, Bremen

Overview

Nanostructure science and technology, an interdisciplinary field, is gaining momentum in materials science due to its focus on materials with dimensions under 100 nm. This scale, found in natural phenomena and engineered materials, notably alters physical properties, creating unique and enhanced characteristics. Examples include microorganisms with tiny ferromagnetic particles. The field encompasses diverse nanostructures, such as atomic clusters, thin films, and bulk materials with nano-features. Our current research project focuses on nanoporous gold surfaces, using advanced computational tools such as density functional theory (DFT) and *ab initio* molecular dynamics (AIMD). These tools are instrumental in exploring the evolution of nanoporous gold surface atoms and the associated adsorbates, highlighting the field's potential for developing materials with novel properties.

Previous research of our group has shown that oxygen (O) atoms, when adsorbed near the step edge on stepped gold surfaces, spontaneously arrange into quasi-ordered Au-O-Au-O chains [1]. This finding was supported by both AIMD simulations and DFT computations. Existing experimental studies have hinted at the possibility of such self-organization into linear chains [2], a notion further corroborated by other computational analyses [3]. In our current project, we have taken a novel approach by initiating the chain formation process with pseudo-randomly placed oxygen atoms, thereby removing any potential bias from our simulations and results. We have extended our investigation to include O atoms on Au(111) and Au(221) surfaces, and also on Au(221) in the presence of additional co-adsorbates such as carbon monoxide (CO) and water (H_2O). Our objective is to gain a deeper insight into how oxygen atoms and these co-adsorbates influence surface restructuring and to improve our understanding of the dynamics of the movement of these adsorbates on the surface.

Results

Our study reveals that O atoms adsorbed in a pseudo-random fashion on an Au(221) surface possess the potential to induce notable surface restructuring, which aligns with the experimental observations and conjectures put forth by Fujita et al. Refer to Figure 1 for visual representations of our simulations and the root mean squared deviation (RMSD) values pertaining to both the surface Au atoms and the O atoms.

Additionally, our study encompasses an examination of the Au(111) surface, where O atoms are randomly adsorbed. In this scenario, we observe minimal surface displacement, yet discern sharper fluctuations in the displacement of the adsorbates. Intriguingly, at certain points, the O atoms on the Au(111) surface exhibit greater displacement compared to those on the Au(221) surface. Hence, we deduce that surface displacement and adsorbate mobility are influenced by factors such as the type of adsorbate, its placement, and the characteristics of the surface. Notably, on the Au(111) surface, the O atoms do not form elongated Au-O

chains; instead, they aggregate into disordered AuO_x clusters. This underscores the diverse structural behaviors exhibited by oxygen adsorbates on different surface types.

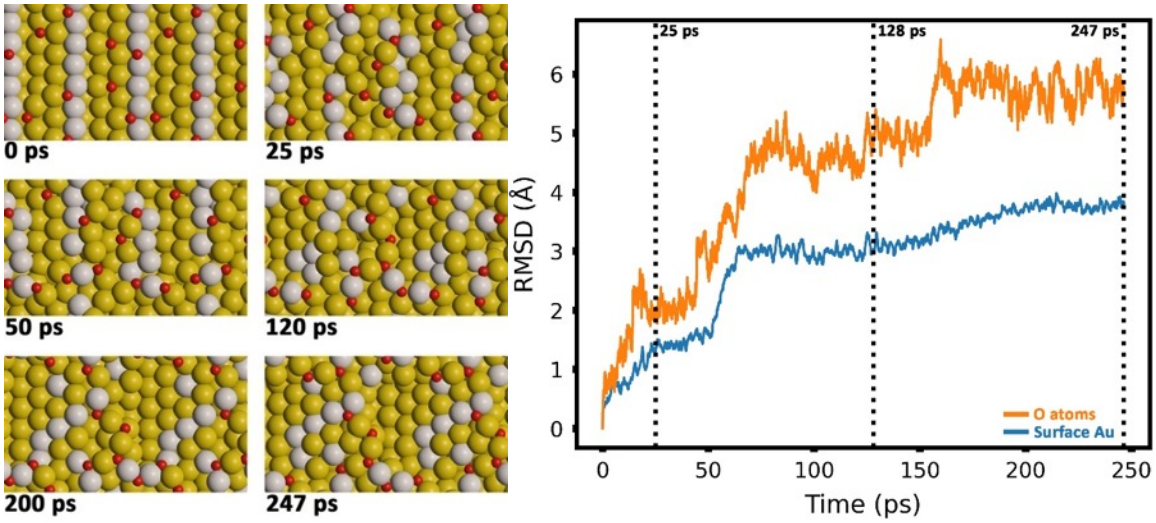

Figure 1: (left) Snapshots of the AIMD simulation involving multiple randomly placed O atoms on the Au(221) surface. The super cells have been multiplied/repeated for better visualisation. Color coding: red = O atoms; white = Au atoms initially at the step edge; yellow = Au atoms. (right) RMSD of the surface Au atoms and O atoms.

Subsequently, we replicated the initial setup depicted in Figure 1, with the addition of several CO molecules randomly placed around the O atoms. Remarkably, this altered configuration exhibits notably reduced surface and adsorbate displacement, indicating a distinct dependency of surface restructuring on the type of adsorbate. As shown in Figure 2, our simulation demonstrates that the presence of CO molecules slows down the formation of Au-O chains and diminishes the extent of displacement required for chain formation.

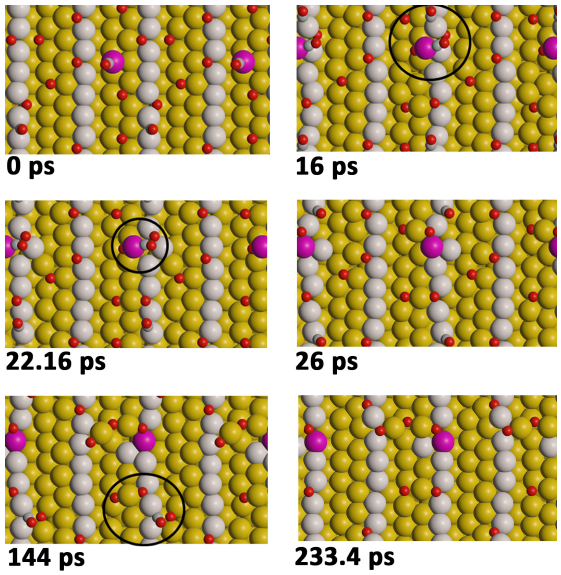

Figure 2: Snapshots of the AIMD simulation involving CO molecules (regular and as an AuCO complex) and O atoms on the Au(221) surface. The super cells have been multiplied/repeated for better visualisation. Color coding: grey = C; red = O; white = Au atoms initially at the step edge; yellow = Au atoms; pink = Au adatom.

Moreover, we observed that these adsorbates engage in reactions, leading to the formation of carbon dioxide (CO_2) molecules that subsequently desorb from the surface. This underscores the dynamic interplay between adsorbates and the surface environment, highlighting the multifaceted nature of surface chemistry phenomena.

Upon introducing water and O atoms to the Au(22) surface (Figure 3), we observe intriguing phenomena wherein H_2O molecules play a facilitating role in chain formation. Concurrently, hydroxyl (OH) groups, transient chains, and hydronium ions (H_3O^+) emerge intermittently throughout the simulation. Despite these dynamic processes, surface restructuring remains relatively limited.

Interestingly, upon removal of the H_2O molecules, we still observe similar surface

restructuring. This outcome suggests that the extent of surface restructuring is primarily influenced by the location of the O adsorbates. These findings shed light on the intricate interplay between adsorbates and the surface environment, emphasizing the nuanced effects of molecular interactions on surface dynamics.

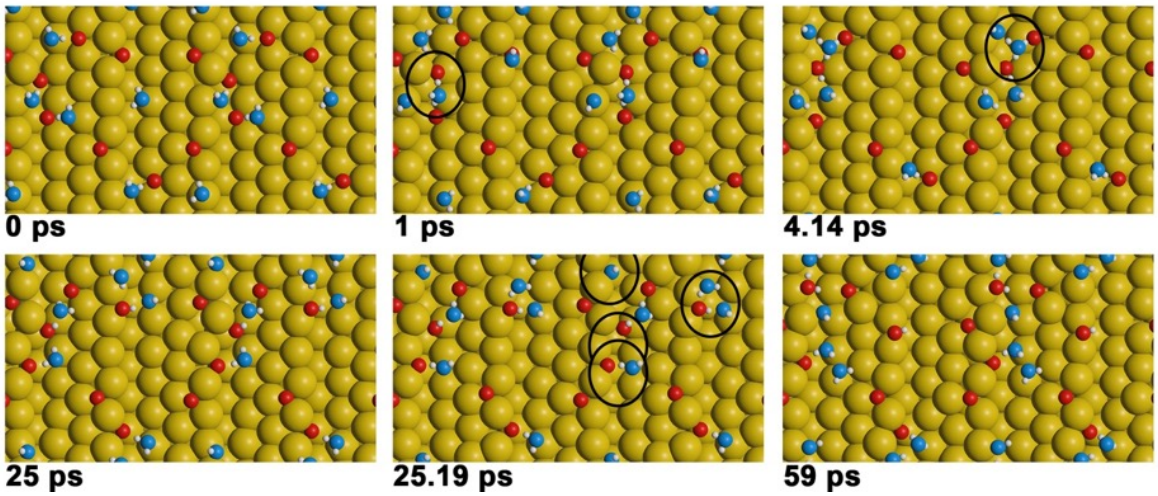

Figure 3: Snapshots of the simulation involving water molecules and atomic oxygen adsorbed on the Au(221) surface. Color coding: Au = yellow; O (atomic) = red; O (water) = blue; H = white.

Furthermore, we explored the reaction between CO and O_2 on bimetallic AuAg(221) surfaces, see Figure 4. In one scenario, Ag atoms are arranged as a biased island at the center of the Au(221) surface, while in another scenario, Ag atoms are randomly dispersed.

Interestingly, we observed that when Ag atoms are randomly scattered, the CO + O_2 reactions occur at an accelerated rate compared to the biased island configuration. However, regardless of the Ag arrangement, the reactions predominantly proceed via the associative mechanism, wherein $CO^* + O_2^* \rightarrow O^* + CO_2(g)$. This mechanistic behavior aligns with our prior investigation [4].

Remarkably, in the simulation with random Ag placement, the third CO + O_2 reaction completes within a mere 15 ps, while in the biased configuration, this reaction remains incomplete even after 25 ps. Despite the notable disparity in reaction kinetics between the two scenarios, we observed minimal differences in surface or adsorbate displacement. These findings underscore the complex interplay between surface structure, adsorbate arrangement, and reaction dynamics on bimetallic surfaces.

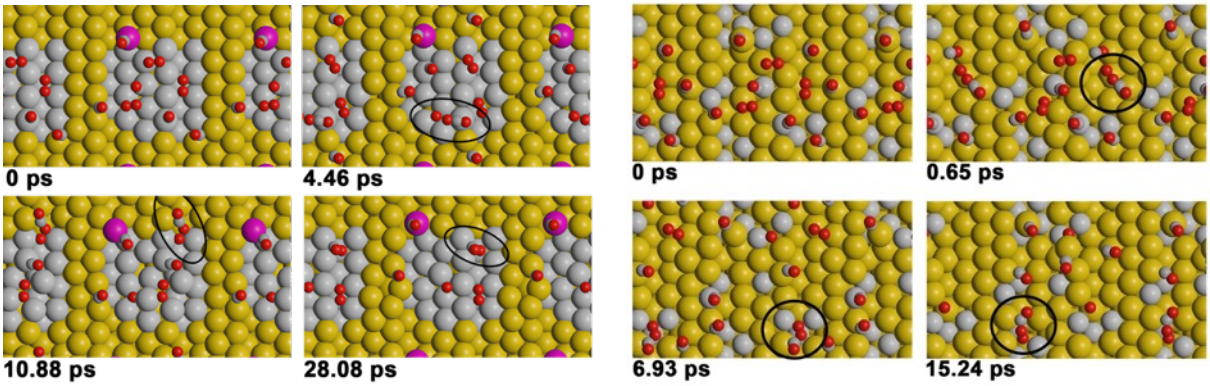

Figure 4: Snapshots of the simulation involving CO molecules and O_2 molecules adsorbed on an AuAg(221) surface: (left) with a biased placement of the Ag atoms, (right) with a random placement of the Ag atoms. Color coding: Au = yellow; O = red; (small) grey = C; (large) grey = Ag; Au adatom = pink.

Outlook

The subsequent phase of our research endeavors entails delving into more intricate molecular systems, such as formaldehyde (CH_2O) reaction with co-adsorbed H_2O and O and methanol (CH_3OH) reaction with O_2 on alloyed AuAg surfaces, where CH_3OH will replace CO in the initial geometries of Figure 4.

Furthermore, we are busy with the implementation of Nudged Elastic Band (NEB) calculations, with a specific focus on CO + O_2 and CO + O reactions occurring on a AuAg(221) surface. These NEB computations aim to provide insights into how surface characteristics and reaction types influence the activation barrier.

Lastly, we are exploring a simulation involving O atoms and Au adatoms incorporated onto an Au(111) surface. This simulation seeks to investigate potential chain formation and the formation of Au clusters on the Au(111) surface, thereby contributing to our understanding of surface dynamics and nanoparticle formation mechanisms.

Publications

1. S. Eltayeb, L.L. Carroll, L. Dippel, M. Mostaghimi, W. Riedel, L.V. Moskaleva, T. Risse, *Low-coordinated sites on gold direct selectivity in partial oxidation of methanol*, submitted
2. S. Li, O. Olaniyan, L. Carroll, L. V. Moskaleva, M. Bäumer, *Catalytic activity of 1D chains of gold oxide on a stepped gold surface from density functional theory*, Phys. Chem. Chem. Phys., 24, 28853-28863 (2022)
3. G. Wittstock, M. Bäumer, W. Dononelli, T. Klüner, L. Lührs, C. Mahr, L.V. Moskaleva, M. Oezaslan, T. Risse, A. Rosenauer, A. Staubitz, J. Weissmüller, A. Wittstock, *Nanoporous Gold: From Structure Evolution to Functional Properties in Catalysis and Electrochemistry*, Chem. Rev., 123, 6716-6792 (2023)

Presentations

1. L. Carroll, L. V. Moskaleva, *Investigating the catalysis on nanoporous gold surfaces using AIMD simulations: Self-organization, reactivity and restructuring*, 4th International Symposium on Nanoporous Materials by Alloy Corrosion, Nohfelden, Germany, April, 2023
2. L. Carroll, L.V. Moskaleva, *Computational Modelling of Catalysis on Nanoporous Gold: Studying the Self-Organization of Oxygen Atoms*, *Surface Restructuring and Reactivity with AIMD Simulations*, Workshop at TU Wien, Vienna, Austria, June, 2023
3. L. Carroll, L.V. Moskaleva, Selforganization, *Restructuring and Reactivity: Computational Modelling of Catalysis on Nanoporous Gold using AIMD Simulations*, ICQC 2023, Bratislava, Slovakia, June, 2023

References

1. Y. Li, W. Dononelli, R. Moreira, T. Risse, M. Bäumer, T. Klüner, L. V. Moskaleva; *Oxygen-driven surface evolution of nanoporous gold: Insights from ab initio molecular dynamics and Auger spectroscopy*, J. Phys. Chem. C, 22, 5349-5357 (2017)
2. F. Hiebel, M. M. Montemore, E. Kaxiras, C. M. Friend, *Direct visualization of quasi-ordered oxygen chain structures on Au(110)-(1 × 2)*, Surf. Sci., 650, 5-10 (2016)
3. M. M. Montemore, R. J. Madix and E. Kaxiras, *How Does Nanoporous Gold Dissociate Molecular Oxygen?* J. Phys. Chem. C, 120, 16636-16640 (2016)
4. S. Li, O. Olaniyan, L. Carroll, L. V. Moskaleva, M. Bäumer, *Catalytic activity of 1D chains of gold oxide on a stepped gold surface from density functional theory*, Phys. Chem. Chem. Phys., 24, 28853-28863 (2022)

5.6 *hbc00062*: Adsorption of pharmaceuticals and personal care products in zeolites studied with density functional theory calculations

HLRN Project ID:	hbc00062
Run time:	Initial: I/2022 – IV/2022, continuations: I/2023 – IV/2024
Project Leader:	PD Dr. Michael Fischer
Project Scientists:	PD Dr. Michael Fischer, Lobna Saeed, Jakob Brauer
Affiliations:	Crystallography & Geomaterials Research Group, Faculty of Geosciences, University of Bremen; Bremen Center of Computational Materials Science, University of Bremen; MAPEX Center for Materials and Processes, University of Bremen, Bibliothekstraße 1, 28359 Bremen

Overview

Electronic structure calculations in the framework of density functional theory (DFT) are used to investigate the interaction of selected pharmaceuticals and personal care products with zeolites. Focus is placed on the adsorption of triclosan, a disinfectant, and of 5-fluorouracil, an anti-cancer drug. In addition to allowing a detailed understanding of the host-guest interactions, the calculations can also deliver insights into the role of water co-adsorption, which is important in most real-world scenarios. Besides, the adsorption of two organic UV filters (UVfs) is investigated in close collaboration with experimental partners. The calculations enable a detailed interpretation of the experimental vibrational (infrared) spectra of zeolite-UVf composite materials.

Scientific background

Zeolites are inorganic crystalline materials whose structures are formed by frameworks of corner-sharing TO_4 tetrahedra (where T = Si, Al, …). The presence of accessible cavities or channels is a distinctive feature of zeolite structures. This intrinsic porosity is pivotal for their large-scale industrial applications, which encompass catalysis, ion exchange, and the separation of gaseous or liquid mixtures. Looking beyond these established uses, zeolites could also be employed in applications involving the adsorption of functional organic molecules. On the one hand, zeolites could be used as adsorbents for the removal of emerging organic contaminants from wastewaters. In this context, the active ingredients of pharmaceuticals and personal care products (PPCPs) have been identified as pollutants of particular concern. [1] On the other hand, zeolites could also be suitable host materials for the encapsulation of drugs or other active compounds, such as organic UVfs that are used in sunscreen lotions.

With regard to the potential use in PPCP removal, highly siliceous zeolites appear as the most promising zeolitic adsorbents, as their hydrophobicity limits the co-adsorption of water. [2,3,4] Following a study of carbamazepine adsorption that was completed during the first project phase,[5] the adsorption of the disinfectant triclosan (TCS), another important PPCP contaminant, was investigated. DFT calculations were employed to predict adsorption energies for six distinct all-silica zeolite frameworks and for two highly siliceous aluminosilicate zeolites. DFT-based *ab initio* molecular dynamics (AIMD) simulations were performed to study the dynamic behavior of adsorbed TCS molecules at room temperature, and the competitive adsorption of water was also considered in the simulations. A subsequent investigation

focused on the adsorption of the anti-cancer drug 5-fluorouracil (5-FU) in FAU-type zeolites having different Si/Al ratios (zeolite framework types are commonly abridged using three-letter codes [6]). This study was motivated by the previously proposed use of highly siliceous FAU-type zeolites as carrier materials for 5-FU delivery. [7]

A separate part of the project dealt with the adsorption of two UVfs, octinoxate (OMC) and avobenzone (AVO), in sodium-exchanged zeolite X (NaX, FAU topology). The computational investigations were carried out in collaboration with experimental partners from the **University of Modena and Reggio Emilia, Italy** (Dr. Riccardo Fantini, Prof. Dr. Rossella Arletti) and the **University of Turin, Italy** (Prof. Dr. Lorenzo Mino). The Modena group has reported the successful incorporation of OMC and AVO in NaX and other zeolites. [8] The collaborator in Turin uses infrared (IR) spectroscopy for a detailed characterization of the zeolite-UVf composites. DFT calculations were used to predict the vibrational spectra of adsorption complexes, thus aiding the interpretation of the experimental IR spectra.

Funding of this research is provided through a Heisenberg grant to PD Dr. Michael Fischer (Deutsche Forschungsgemeinschaft project no. 455871835, Fi1800/6-1). The associated PhD students are funded by the DFG (Jakob Brauer, DFG project no. 492604837) and by the Central Research Development Funds of the University of Bremen (Lobna Saeed).

Project results

DFT studies of TCS adsorption in all-silica zeolites **[P1]** showed that the adsorption energy is not strongly affected by the framework topology, as the flexible TCS molecule can adjust to different pore shapes without any significant energetic penalty (a noteworthy difference to the previously studied carbamazepine molecule [5]). The interaction in aluminosilicate zeolites is distinctly stronger than in their all-silica counterparts, an observation that is straightforwardly explained with the formation of hydrogen bonds between a zeolite framework proton and the hydroxyl group of TCS. AIMD simulations confirmed the stability of these hydrogen bonds at room temperature in the absence of water. However, the inclusion of co-adsorbed water molecules in the simulations resulted in framework deprotonation, formation of a hydronium ion in the pores, and a motion of the TCS molecule away from the vicinity of the framework Al atom. As a decrease in hydrophobicity will incur a more significant competitive adsorption of water, weakening the interaction with TCS, it can be inferred that the hydrophobicity of the adsorbent should be maximized for efficient TCS removal.

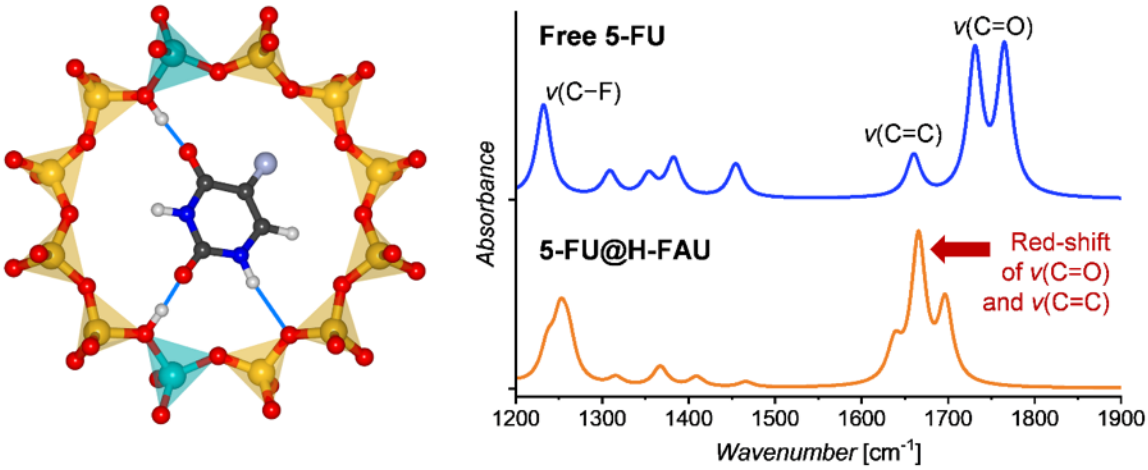

Figure 1: Left: Representative configuration of 5-FU molecule adsorbed in H-FAU. For clarity, only one twelve-membered ring of the H-FAU structure is shown. Thin blue lines indicate hydrogen bonds. **Right:** DFT-calculated IR spectra of free 5-FU and of adsorbed, hydrogen-bonded 5-FU@H-FAU.

The investigation of 5-FU adsorption looked at “multi-site” interactions of 5-FU, which possesses two negatively polarized carbonyl groups, with more than one framework proton in zeolites having different Si/Al ratios. The left panel of **Figure 1** shows a representative example, in which the 5-FU molecule is stabilized through several hydrogen bonds. The comparison of the simulated IR spectrum to that of free 5-FU in the right panel of **Figure 1** shows that there are distinct features that should facilitate the spectroscopic identification of such hydrogen-bonded 5-FU molecules. Interestingly, qualitatively different features have been reported in an experimental study, [7] which are likely due to the adsorption of 5-FU at extra-framework Al sites, rather than framework protons, in the studied samples. Additional calculations have been performed to investigate the behavior of adsorbed 5-FU in the presence of water. As water molecules tend to displace 5-FU from the vicinity of the framework Al atoms, it seems possible to trigger 5-FU release through exposure to water.

With regard to organic UV filters, the molecules octyl methoxycinnamate (OMC) and avobenzone (AVO) were considered in the combined experimental-computational investigations. Both of these species were successfully encapsulated in zeolite NaX in earlier work.[8] The study of OMC adsorption focused primarily on two questions, namely, the dominant isomer in the adsorbed state and the nature of the stabilizing host-guest interactions.[P2] A comparison of DFT-calculated IR spectra for two OMC isomers (cis vs. trans) adsorbed in the pores of NaX to experimental data indicates that adsorbed OMC is primarily in the trans form (Figure 2, note especially the features in the wavenumber range from 1550 to 1650 cm-1). Localized interactions between sodium cations and different parts of the OMC molecule (oxygen atoms, phenyl ring) play a key role in stabilizing OMC in the zeolite pores. These interactions also manifest in characteristic shifts of certain IR-active modes, allowing for their experimental detection. Besides, ubiquitous dispersion interactions make a significant contribution to the total adsorption energy. For OMC, the trans form is the more efficient UV absorber, and the findings of the combined DFT and spectroscopic study thus explain why the OMC@NaX composite retains the good UV absorption properties of the free molecule. For avobenzone, a preliminary analysis of experimental IR spectra and DFT calculations indicates that adsorbed AVO is dominantly in the diketo form. As this tautomer has less beneficial UV absorption properties than the keto-enol form, it appears surprising that the AVO@NaX composite still shows a very similar absorption spectrum as free AVO. [8] Future work will aim to reconcile these discrepancies.

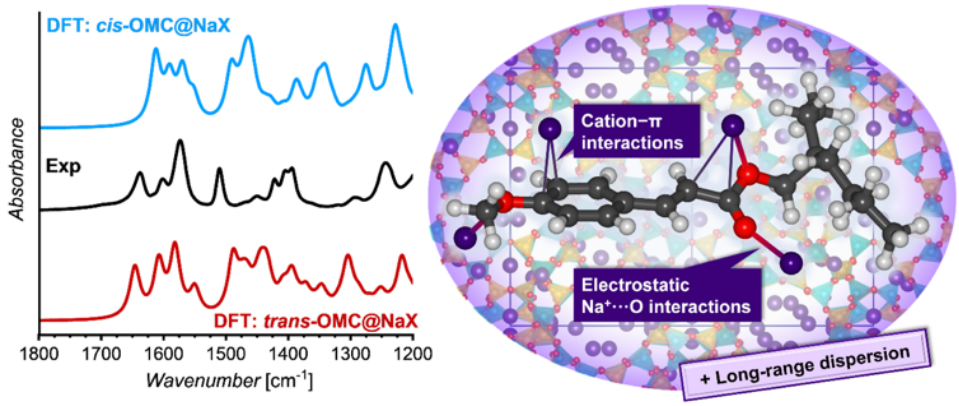

Figure 2: Left: Comparison of experimental IR spectrum of OMC@NaX (black) to DFT-calculated spectra for different isomers in NaX (blue/red). **Right:** Cartoon-like representation highlighting interaction types that stabilize *trans*-OMC in the pores of NaX.

Other calculations associated with the project have dealt with the development of surface models of clinoptilolite, an important natural zeolite that could be used in drug delivery and wastewater treatment, and with the thorough benchmarking of dispersion-corrected DFT calculations to compute adsorption energies of emerging organic contaminants in all-silica zeolites. **[P3]**

Outlook

In the next project phase, the role of “multi-site” interactions will be investigated for other relevant guest molecules, such as the stimulant caffeine, the antibiotic metronidazole, and the monomer bisphenol A, used in the production of various plastics. Moreover, it will be attempted to employ realistic modes of extra-framework aluminum sites in order to study the interaction of 5-FU and other relevant molecules with such sites. Due to the importance of guest molecule diffusion for many applications, DFT-based AIMD simulations will be used to train accurate machine-learned potentials that can afterwards be used in diffusion simulations. Research on clinoptilolite surfaces will be expanded towards the modelling of pharmaceutical adsorption at these surfaces.

Publications

P1 M. Fischer, Density functional theory study of hydrophobic zeolites for the removal of triclosan from aqueous solution, Environ. Sci. Adv. 2, 1082–1098 (2023)

P2 M. Fischer, R. Fantini, R. Arletti, J. Brauer, L. Mino, Unraveling the Molecular Structure of Zeolite–Octyl Methoxycinnamate Hybrid UV Filters: A Combined Spectroscopic and Computational Approach, J. Phys. Chem. C 127, 24242–24252 (2023)

P3 M. Fischer, J. Brauer, Studying the adsorption of emerging organic contaminants in zeolites with dispersion-corrected density functional theory calculations: From numbers to recommendations, ChemistryOpen, online: https://doi.org/10.1002/open.202300273

Presentations (selection of oral presentations)

O1 M. Fischer, J. Brauer, Atomistic modelling approaches to study the adsorption of emerging organic contaminants in hydrophobic zeolites, European Zeolite Conference (FEZA2023), Portorož (Slovenia), 2nd to 6th July 2023

O2 R. Fantini, G. Vezzalini, G. Confalonieri, F. Di Renzo, L. Mino, R. Cavalli, M. Argenziano, M. Fischer, M. Sisti, R. Arletti, Characterization and technological performances of zeolite-encapsulated organic UV filters, EUROCLAY 2023, International Conference of European Clay Groups Association, Bari (Italy), 24th to 27th July 2023

O3 M. Fischer, J. Brauer, Computational studies of zeolites as adsorbents for the removal of pharmaceuticals and personal care products, MinWien2023, Joint Meeting of the German, Austrian, and Slovakian Mineralogical Societies, Vienna (Austria), 17th to 21st September 2023

References

[1] M. Patel, R. Kumar, K. Kishor, T. Mlsna, C. U. Pittman Jr, D. Mohan, Chem. Rev. *119, 3510–3673 (2019)*

[2] A. Martucci et al., Microporous Mesoporous Mater. *148, 174–183 (2012)*

[3] D. J. de Ridder, J. Q. J. C. Verberk, S. G. J. Heijman, G. L. Amy, J. C. van Dijk, Separ. Purf. Technol. *89, 71–77 (2012)*

[4] N. Jiang, R. Shang, S. G. J. Heijman, L. C. Rietveld, Water Res. *144, 145–161 (2018)*

[5] M. Fischer, *ChemPhysChem 24, e202300022 (2023)*

[6] C. Baerlocher, L.B. McCusker, Database of Zeolite Structures (fully revised 2017); http://www.iza-structure.org/databases

[7] A. Datt, E. A. Burns, N. A. Dhuna, S. C. Larsen, Microporous Mesoporous Mater. *167, 182–187 (2013)*

[8] R. Fantini, G. Vezzalini, A. Zambon, E. Ferrari, F. Di Renzo, M. Fabbiani, R. Arletti, Microporous Mesoporous Mater. *328, 111478 (2021)*

5.7 *hbi00037:* Molekulardynamische Untersuchung der Stressbeanspruchungen auf Proteine an der Phasengrenzfläche beim Premix-Membranemulgieren

HLRN-Projektkennung:	hbi00037
Laufzeit:	I/2019 – II/2023
Projektleiter:	Prof. Dr.-Ing. habil Udo Fritsching
Projektbearbeiter.	Patrick Giefer, M.Sc
Institut / Einrichtung:	Fachgebiet Mechanische Verfahrenstechnik, Universität Bremen

Überblick

Emulgierverfahren werden im Rahmen des Downstream-Prozessierens und der Weiterverarbeitung/Formulierung zur Homogenisierung oder auch Verkapselung in biogenen Produkten eingesetzt. Beim Premix-Emulgieren wird eine grobdisperse Voremulsion mittels der Dispergierung in porösen Membranen in eine Feinemulsion bzw. -dispersion überführt. Insbesondere das Stress-Verweilzeitverhalten und die darauf erfolgende Reaktion eines protein-stabilisierten dispersen Systems bedarf einer vertieften wissenschaftlichen Klärung. Hieraus können mechanistische Schädigungsmodelle abgeleitet werden. Die im Emulgier-Prozess auftretenden mikromechanischen Belastungen auf biologische Systeme sind nicht vollständig geklärt, die Prozessumgebung ist somit noch weiter zu entwickeln im Hinblick auf die Anpassung an spezielle biologische Systeme. Um den Einfluss des Premix-Emulgierverfahrens und der dabei auftretenden Stress-Verweilzeit-Belastungen auf die agglomerierten Proteine (hier beta-Lactoglobulin) im Fluid und an den Phasengrenzflächen zu untersuchen, werden numerische Untersuchungen auf molekulardynamischer Ebene an Proteinstrukturen durchgeführt. Diese Untersuchungen zeigen, inwieweit die Proteinstrukturen durch den Emulgiervorgang belastet und geschädigt werden können, beziehungsweise ob eine proteinschonendere Emulgierung mit den Membranen möglich ist.

Das Projekt ist in dem DFG geförderten Schwerpunktprogramm 1934 „DISPBiotech“ eingebunden. Der Förderungszeitraum der zweiten Förderperiode beträgt 36 Monate

Ergebnisse

Zielsetzung des Projektzeitraumes waren molekulardynamische Simulationen, um den Einfluss von Proteinadsorption and flüssig/flüssig und flüssig/fest Grenzflächen auf die Benetzbarkeit im Premix-Membran-Emulgieren zu untersuchen. Darüber hinaus wurden die molekulardynamische Untersuchung von rekombinanten Varianten des Milchproteins beta-Lactoblobulin an flüssig/flüssig Grenzflächen vertieft, um den Einfluss von Disulfidbrücken auf den Adsorbtionsvorgang zu quantifizieren.

Einfluss der Proteinadsorption auf die Benetzbarkeit

In Experimenten zum Premix-Membranemulgieren hat sich gezeigt, dass die zur Emulsionstabilisierung eingesetzten Proteine nicht nur an der flüssig/flüssig Phasengrenzfläche adsorbieren, sondern auch an die fest/flüssig Phasengrenzfläche adsorbieren und folglich den Prozess beeinflussen können. Aus bereits veröffentlichten Forschungsergebnissen ist bekannt, dass die Benetzungseigenschaft der Membran und damit der Kontaktwinkel, den Tropfenaufbruch maßgeblich beeinflusst. [1] Um den Einfluss der

Proteinadsorption zu quantifizieren, werden molekulardynamische Simulationen mit und ohne Proteinadsorption durchgeführt. Dazu ist in Abbildung 1 die Start-Konfiguration der Simulationen ohne Proteine dargestellt. Da es sich bei der Benetzung immer um einen dreiphasigen Kontakt handelt müssen auch alle drei Phasen simuliert werden. In diesem Fall: das kontinuierliche Medium Wasser, die disperse Phase Öl und das Membranmaterial Silica. Nach der Young-Dupré Gleichung setzt sich der Gleichgewichtskontaktwinkel θ_e aus den Grenzflächenenergien der drei binären Systeme als,

$$cos\theta_e = \frac{\gamma_{SK} - \gamma_{SD}}{\gamma_{KD}}$$

zusammen. Dabei steht γ für die Grenzflächenspannung und die Indizes S für die solide Phase, K für die kontinuierliche Phase und D für die disperse Phase. An die Simulationen anschließend wurden Simulationen mit Proteinadsorption an die feste Grenzfläche durchgeführt. Dazu wurden verschiedene Proteinkonzentrationen an der Grenzfläche betrachtet und der Kontaktwinkel ausgerechnet. In Abbildung 2 ist eine vollständig belegte Grenzfläche beispielhaft dargestellt.

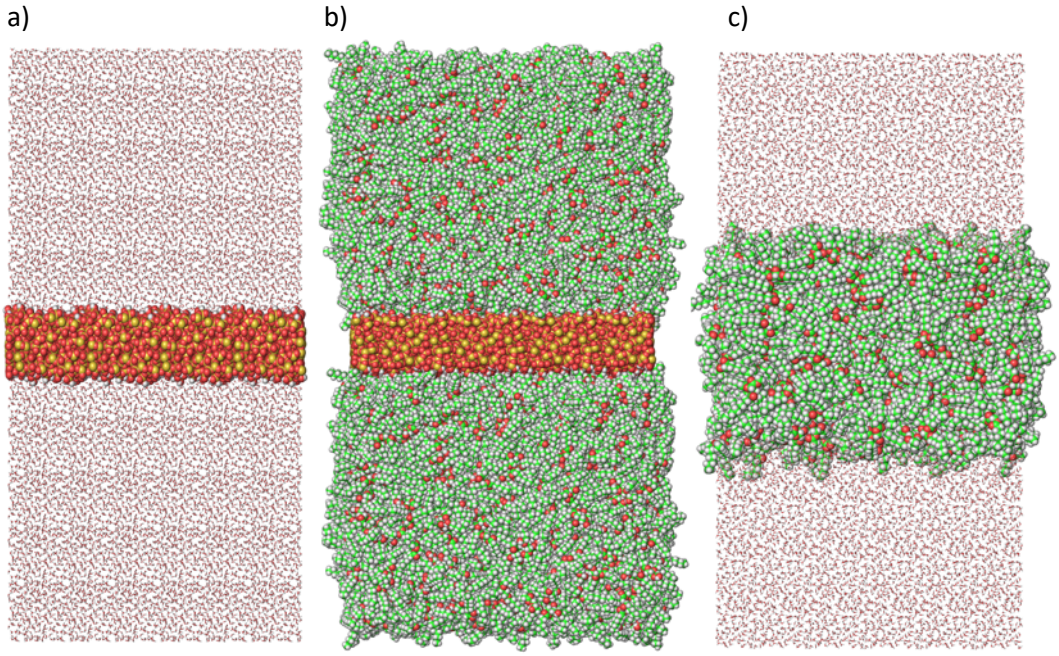

Abbildung 1: Seitliche Ansicht der Start-Konfigurationen für unbelegte flüssig/fest und flüssig/flüssig Grenzflächen für a) Wasser/Silica, b) Öl/Silica und c) Wasser/Öl

Die Ergebnisse aus den Simulationen zeigen, dass eine unbelegte Grenzfläche einen Kontaktwinkel von θ_e= 70.66° aufweisen, wohingehend ein belegtes System mit 5 Proteinen schon zu einer Änderung des Kontaktwinkels zu θ_e= 111.2° führt. Diese Ergebnisse wurden mit Hilfe von experimenteller Bestimmung des Kontaktwinkels validiert. Aus diesen Ergebnissen konnten die Kontaktwinkel als Randbedingung für eine CFD Berechnung herangezogen werden. Diese hat gezeigt, dass mit der vorliegenden Änderung des Kontakwinkels das Regime in dem sich Tropfen innerhalb des Emulgierprozesses bilden können um 31 % zu höheren Kapillarzahlen verschiebt. Diese Ergebnisse konnten nur durch die Bereitstellung von Rechenresourcen des HLRN erzielt werden und wurden unter Anerkennung dieser in [4] veröffentlicht.

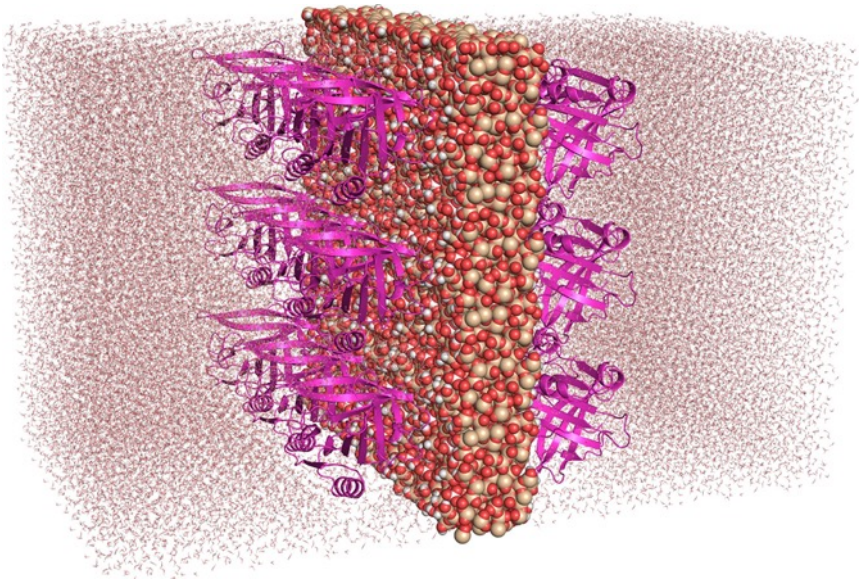

Abbildung 2: Vollständig belegte Wasser/Silica Grenzfläche mit adsorbierten beta-Lactoglobulin Proteinen

Einfluss der Disulfidbrücken auf die Adsorption von beta-Lactoglobulin

Der Einfluss von Disulfidbindungen von beta-Lactoglobulin auf die Proteinstruktur und die Grenzflächenadsorption an Öl/Wasser wurde untersucht. Dafür wurden verschiedene rekombinante Varianten betrachtet, bei denen die Cysteine durch Alanin ersetzt wurden. Experimentelle Analysen der Varianten und molekulardynamische Studien wurden genutzt, um den Effekt der Cysteine auf die Struktur, die Grenzflächenadsorption und die Eigenschaften des Proteinfilms zu quantifizieren. Dazu wurden die Varianten sowohl im Bulk-Wasser als auch an Öl/Wasser-Grenzflächen analysiert.

Die Variante noCYS (ohne verbleibende Disulfidbindungen) zeigt signifikante strukturelle Veränderungen im Bulk, die mit der Entfernung aller Cysteine verbunden sind: eine Abnahme der β-Faltblätter sowie eine Zunahme von α-Helix und random coil. Insbesondere scheint die Zunahme von α-Helix wichtig für die Adsorption an Öl/Wasser-Grenzflächen zu sein, da diese während des teilweisen Entfaltens mit dem Öl interagiert. Es konnte gezeigt werden, dass die anderen Varianten weniger α-Helices aufweisen und sich in der simulierten Zeit nicht an der Grenzfläche entfalten, sowie niedrigere Adsorptionsraten in den Experimenten im Vergleich zur Variante ohne Cysteine aufweisen.

Bemerkenswert ist, dass die Variante C66A/C160A eine veränderte Adsorptionskonfiguration zeigt, bei der der N-Terminus mit der Grenzfläche interagiert und der C-Terminus von der Grenzfläche abgewandt ist (siehe Abbildung 4). Die strukturelle Flexibilität an der Grenzfläche der Variante noCys ist insgesamt am höchsten unter den Varianten und unterstützt die Adsorption an der Öl/Wasser-Grenzfläche sowie das anschließende Entfalten dieser Variante. Darüber hinaus zeigt diese Variante viskoelastische Filmeigenschaften, was darauf hinweist, dass sie gegen Deformation der Grenzfläche stabiler ist.

Während der Adsorption und teilweisen Entfaltung der Variante noCys werden hydrophobe Reste freigelegt, die die Anordnung des Proteins an der Grenzfläche stabilisieren. Die äußere Disulfidbindung wurde als wichtig für die Neuordnung an der Grenzfläche identifiziert: Die Löschung dieser Bindung zeigt den größten Effekt im Vergleich zur Kontrolle. Es ist außerdem wichtig, dass beide Cysteine der Aminosäuresequenz, die zu einer Disulfidbindung beitragen, ersetzt werden, um die Bindung zu löschen. Ohne dies, kann aufgrund der möglichen Interaktion der verbleibenden oder mutierten Aminosäure mit anderen Aminosäuren des Proteins, das Entfalten durch neu entstandene Stabilisierungen behindert werden.

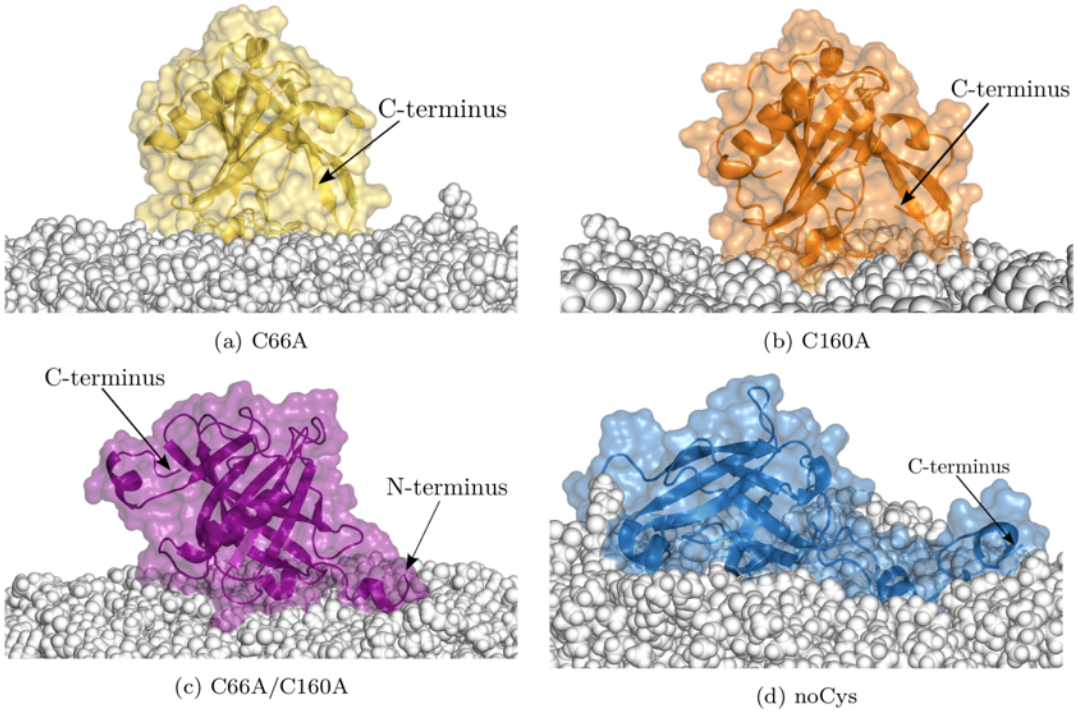

Abbildung 3: Adsorptionskonfiguration der simulierten Varianten, der C-terminus und N-Terminus sind hervorgehoben

Publikationen

1. P. Giefer, A. Kyrloglou, *Impact of wettability on interface deformationand droplet breakup in microcapillaries*, Physics of Fluids, 35, 042110 (2023)
2. A. Heyse, M. Gößmann, P. Giefer, *Lipase adsorption during premix-membrane emulsification affects membrane surface properties and structural conformation of lipase*, Process Biochemistry, 132, 75-85 (2023)
3. P. Giefer, S. Bäther, *Characterization of β-lactoglobulin adsorption on silica membrane pore surfaces and its impact on membrane emulsification processes*, Journal of Colloid and Interface Science, 652, 1074-1084 (2023)
4. P.Giefer, A. Heyse, *How adsorbed proteins at solid interfaces impact the droplet propagation through micro capillaries*, Physics of Fluids, 36, 012136 (2024)
5. P. Giefer, A. Heyse, *Cysteines in β-lactoglobulin impact the protein structure and interfacial adsorption*, under review

Vorträge / Poster

1. P. Giefer, Vortrag*, Liquid/Liquid Displacement in Microchannels and the Effect of Wettability*, DECHEMA Jahrestreffen MPH, Paderborn, 03.2023
2. P. Giefer, A. Heyse, Vortrag, *Liquid-Liquid Displacement in Capillaries and Proteins at Interfaces*, ECCE&ECAB, Berlin, 09.2023

5.8 *hbi00059:* A systematic ab-initio vibrational spectra study of Mars' olivine solid solutions

HLRN Project ID:	hbi00059
Run Time:	IV/2022 – III/2023
Project Leader:	Lorenzo Bastonero
Project Scientists:	Prof. Dr. Nicola Marzari, Prof. Dr. Lucio Colombi Ciacchi
Affiliation:	U Bremen Excellence Chair, Bremen Center for Computational Materials Science, and MAPEX Center for Materials and Processes, University of Bremen, Germany

Overview

In the latest years, the general interest in Mars human exploration programs have risen again [1], boosted by the new private market and the related advances in green technologies. One of the main challenges is the in-situ characterisation of the Martian soil, essential for many applications, due its complex nature of amorphous and mixed oxides phases [2]. Infra-red (IR) and Raman spectroscopies are among the most employed methods for the investigation of such materials. Nevertheless, these spectra can be extremely complex and their interpretation not straightforward, calling for theoretical support. Olivines are one of the most prominent mineral group in Martian regolith, and neither its transition metal end-members nor its solid solutions vibrational spectra have been described accurately yet. A deep understanding of these spectra is thus desirable for the advancement in the field. We employ density functional theory (DFT) for this analysis, and describe the transition metal end-members through Hubbard corrections to cure for self-interaction errors, and by determining self-consistently the Hubbard parameters from the density functional perturbation theory framework [3]. The simulations are performed using our freshly developed automatic workflow for IR and Raman spectra within the AiiDA infrastructure, which exploits finite displacements and finite fields to allow application to any complex functional. Prior to the olivines spectra, we first fully benchmark our implementation against well established experimental and theoretical materials vibrational spectra in both polarized single-crystal and powder setups.

Overview

The first step of this work was to benchmark our ab-initio code implementation on a prototypical ferroelectric material: $LiNbO_3$ (space group R3c, no. 161). This latter vibrational spectra have long been debated in the literature and exhibit large LO-TO phonon splittings at $\mathbf{q} \approx \mathbf{0}$ that are ideal for exploring different exchange-correlation functionals. Its experimental polarized single-crystal Raman spectra are well known and measured in different scattering geometries. In Fig. 1 we compare the experimental measured spectra with density-functional theory predictions employing seven different functionals. The calculations show very good agreement with the experiments, both for polarized single-crystal and powder sample spectra. For this material, the best performing functional is PBE0, with a remarkable mean average error (MAE) on peak positions ($\overline{|\Delta\omega|}$) of 7 cm^{-1}. PBEsol with extended Hubbard functional ($+U_{sc} + V_{sc}$) shows as well very good performance, with about 11 cm^{-1} MAE on frequencies and the lowest relative error (16%) on peak intensities. This preliminary work shows the importance of using different functionals for the calculation of vibrational spectra from first-principles. Importantly, we deployed the code for performing these automated calculations as an open-source software, available on GitHub and on PyPI, under the name of `aiida-vibroscopy`. The code can also

compute infrared absorption and reflectivity spectra, phonon dispersion and related thermal properties, in fully automated user-friendly fashion.

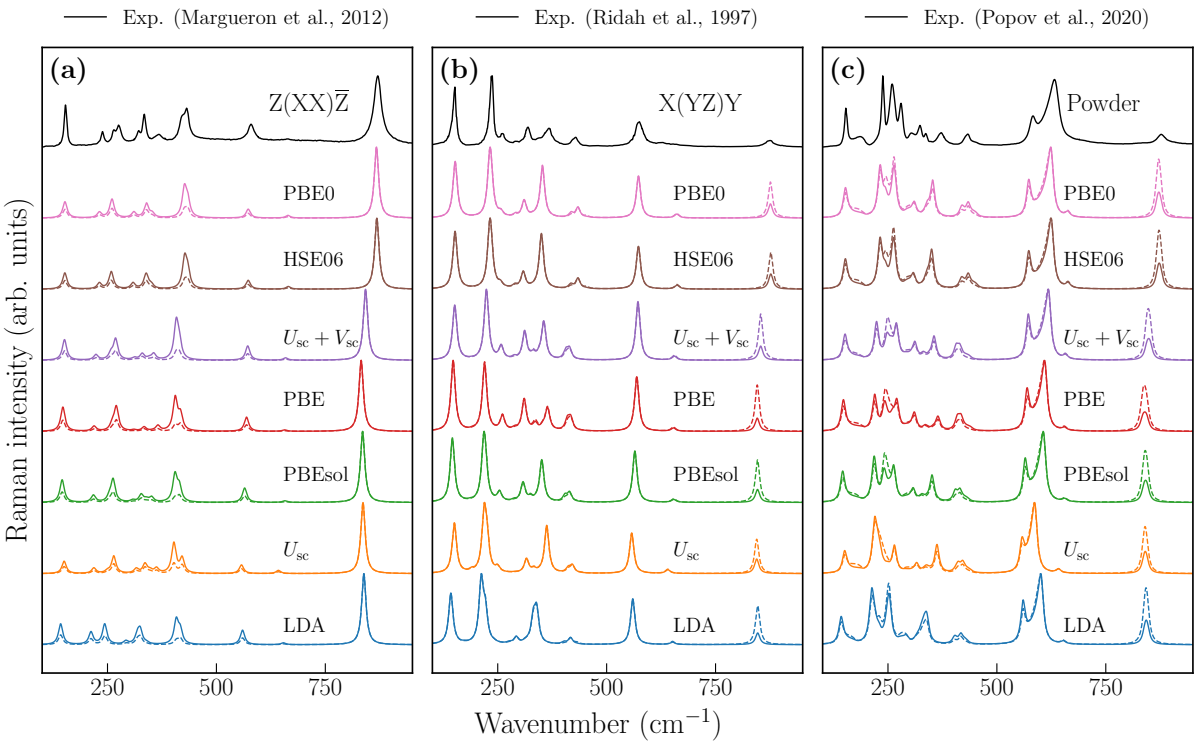

Figure 1: Polarized single-crystal and powder Raman spectra of ferroelectric $LiNbO_3$ as obtained with seven different functionals, and compared to experimental measurements [4,5]. (a,b) Raman spectra of single-crystal polarized setups; the scattering geometry is reported in the Porto notation. (c) Raman spectra of polycrystalline powder sample; the theoretical spectra are computed using the spherical average formula [6]. In each panel, the dashed lines show the computed spectra when the Fröhlich term in neglected. Theoretical intensities are smeared with a constant 12 cm^{-1} broadened Lorentzian. The theoretical spectra are reported in order of decreasing error $\overline{|\Delta\omega|}$, and Hubbard-corrected PBEsol are abbreviated only with their corrective parameters.

As planned, we then computed, using self-consistent Hubbard corrections, the Raman spectra of faylite, the iron end-member of the olivine serie, the second most abundant cation in such mineral group. As in our preliminary results on forsterite (magnesium end-member), we computed the spectra using different van der Waals corrections on top of the PBEsol functional, as shown in Fig. 2(a); these corrections should describe better translational modes at higher frequencies. It can be noted that some improvements at higher frequencies are obtained, although such improvements are modest and are significant only for one functional. Interestingly, LDA+U_{sc} is the best performing functional among the one tested for this material. This is in fact a common result in silicate compounds, and the better performance at higher frequencies is due to the overbinding and consequent underestimation of the volume (as also shown in our preliminary results). On the other hand, PBEsol+*U*sc still provides decent agreement, and especially it predicts a satisfactory cell geometry, which is important to compute other properties and/or spectra, such as XRD. Furthermore, the olivine solid solution Raman spectra are usually characterized by visible and measurable peak shifts in the two highest frequency and highest intensity A_g modes, which are easily measurable and less affected by experimental noise. In Fig. 2(b) we reported the comparison between DFT and experiments of such shifts for the three highest frequency and highest intensity A_g modes between the Mg and Fe end-members. Interestingly, the shifts are less functional dependent, and the PBEsol(+U_{sc}) functional gives the best matching results. We note nevertheless that all the functionals give rather close results, with a spread comparable to the experimental

uncertainty (about ±2 cm^{-1}). As such shifts are extremely useful for the material characterization, we then decided to employ the PBEsol for studying the solid solution.

The previous analysis allowed us to select a good functional to model the olivine solid solutions. We then focused in particular on the Mg–Fe solid solution. For the latter, the magnetic and the atomic ordering are not known. Considering fayalite, the pure Fe end-member, has an antiferromagnetic ground-state at low temperature, we needed to explore the configurational phase-space for the solid solution to find the (magnetic) ordering at low temperature. To this end, we started by constructing structures $(Mg_xFe_{1-x})_2SiO_4$ with different atomic and magnetic orderings and we computed self-consistently the Hubbard parameters for the Fe sites. Interestingly, the final Hubbard $U_{Fe,sc}$ is always 5.0 ± 0.2 eV. Moreover, when setting U_{Fe} = 5.0 eV, the final total energy and forces have a negligible change when compared to the results with full self-consistent $U_{Fe,sc}$. This result is very useful, since it allows us to employ for this material a unique Hubbard value on all the Fe sites in the structure, thus avoiding to compute the Hubbard *U* self-consistently for large structures, which are required to model the solid solution.

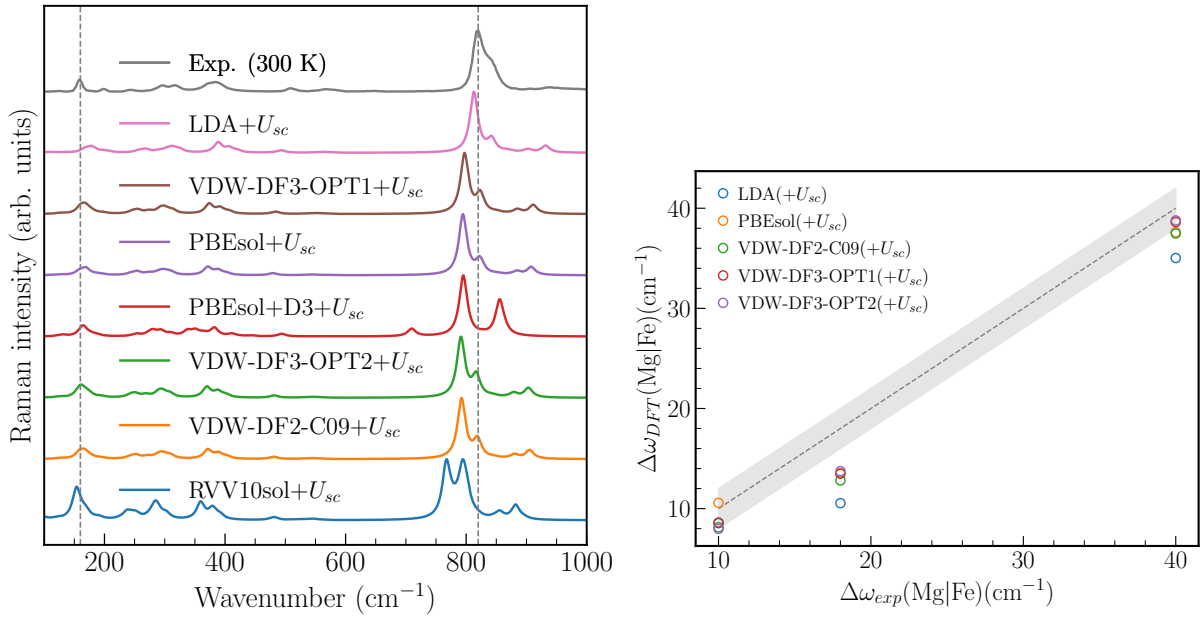

Figure 2: (a) Raman spectra of powder fayalite (Fe_2SiO_4) using different functionals and compared to experimental results found on the open-access online RRUFF database for vibrational spectra of minerals. (b) Shift of the three highest frequency and highest intensity A_g modes between pure forsterite (Mg_2SiO_4) and fayalite (Fe_2SiO_4) computed with different functionals and compared to experiments (Hubbard corrections are applied to the iron end-member). Gray area represents ±2 cm^{-1} from the experimental references; ideally, the points should lie on the dashed line, or within the faded area, for optimal agreement.

Overview

The results obtained during the project period will allow us to study the olivine solid solution comprising of the Mg and Fe cations. Thanks to the AiiDA infrastructure, we managed to compute hundreds of supercell configurations for $(Mg_xFe_{1-x})_2SiO_4$ with varying *x*. The data produce will then be employed to fit a cluster expansion model that can be used for Monte Carlo simulations to find the ground-state configurations of this important class of minerals. To benchmark the accuracy of the future predictions, we will benchmark the Néel temperature as a function of *x* with the experimental literature, where the structure undergoes a magnetic transition from antiferromagnetic (low temperature) to paramagnetic (high temperature). Once

the ground-state structures are found, the data will be employed again to train a neural network potential to predict inexpensively the Raman modes and the thermal properties as a function of the composition *x*. These can then be used to infer from theory the expected Raman shifts in ideal solid solution as a function of *x*.

Publications

1. Lorenzo Bastonero and Nicola Marzari*, Automated all-functional infrared and Raman spectra* (in press, npj Computational Materials), arXiv:2308.04308 (2023)
2. Garu Gebreyesus, Lorenzo Bastonero, Michele Kotiuga, Nicola Marzari, and Iurii Timrov, *Understanding the role of Hubbard corrections in the rhombohedral phase of BaTiO3*, Physical Review B 108, 23 (2023)
3. Anees Pazhedath, Lorenzo Bastonero, Nicola Marzari, and Michele Simoncelli, *First-principles characterization of thermal conductivity in LaPO4-based alloys*, arXiv:2309.10789 (2023)

References

[1] C. A. Platt, M. Jason, and C. J. Sullivan, Space Policy 51, doi:10.1016/j.spacepol.2019.101358 (2020).

[2] C. N. Achilles, R. T. Downs, D. W. Ming, E. B. Rampe, R. V. Morris, A. H. Treiman, S. M. Morrison, D. F. Blake, D. T. Vaniman, R. C. Ewing, S. J. Chipera, A. S. Yen, T. F. Bristow, B. L. Ehlmann, R. Gellert, R. M. Hazen, K. V. Fendrich, P. I. Craig, J. P. Grotzinger, D. J. D. Marais, J. D. Farmer, P. C. Sarrazin, and J. M. Morookian, Journal of Geophysical Research: Planets 122, 2344 (2017).

[3] I. Timrov, N. Marzari, and M. Cococcioni, Physical Review B 98, 085127 (2018).

[4] S. Margueron, A. Bartasyte, A. M. Glazer, E. Simon, J. Hlinka, I. Gregora, and J. Gleize, Journal of Applied Physics 111, 104105 (2012).

[5] S. Kojima, K. Kanehara, T. Hoshina, and T. Tsurumi, Japanese Journal of Applied Physics 55, 10TC02 (2016).

[6] M. N. Popov, J. Spitaler, V. K. Veerapandiyan, E. Bousquet, J. Hlinka, and M. Deluca, npj Computational Materials 6, 121 (2020).

5.9 *hbi00062*: Multiphase numerical modeling for water jet quenching of the stationary and moving metal plate

HLRN Project ID:	hbi00062
Run time:	III/2023 – II/2024
Project Leader:	Prof. Dr.-Ing. Lutz Mädler, Prof. Dr.-Ing. Udo Fritsching
Project Scientists:	M. Sc. Nithin Mohan Narayan
Affiliation:	University of Bremen, Germany

Overview

Quenching is widely applied in metal industries for improving the material properties thereby making it suitable for various engineering applications. In this process the plate is heated above the Leidenfrost temperature and cooled by water jet or array of water jets. For the applications such as chill casting, hot rolling etc., the metal sample is moving below the water jets. Since the metal plate is being quenched from a higher surface temperature the boiling heat transfer dominates and thereby higher temperature gradients are involved which can lead to plate deformation and cracking. Moreover, experiments at these high temperatures are technically limited. To solve this problem, a multiphase numerical model based on the Euler-Euler approach is developed and validated with experiments to study the spatial and temporal heat transfer behavior during quenching of the stationary and the moving plates. The movement of the plate is realized by incorporating the concept of sliding mesh. The validated simulations can provide the technical parameters of the impinging surface that are not directly available from an experiment. The influence of process parameters such as jet Reynolds number, plate velocity, surface temperature etc. are numerically investigated. This model could provide the parameters such as the heat flux, heat transfer coefficient (HTC), Leidenfrost temperature, wetting front behavior etc. of the conjugate heat transfer problem.

Results

As planned in the project proposal, the numerical modeling of single jet (Q3) and two jets quenching (Q4) are accomplished in 2023. The required discretisation has been generated with ANSYS ICEM-CFD 19.2 and the numerical simulations are performed in ANSYS Fluent 19.2. The temperature and vapor contours (numerical results) of single jet and two jets quenching are shown in Figs. 1 and 2 respectively.

A numerical model is developed and validated for single-jet quenching. Due to the axial symmetry of the process, only one quadrant of the whole domain is modeled. Infrared imaging and high-speed imaging techniques are employed to obtain hydrodynamic and thermodynamic validation. This validated numerical model provides the technical information such as cooling curves, heat flux, wetting front propagation, heat transfer coefficient (HTC), Leidenfrost temperature, maximum heat flux temperature etc. These cannot be obtained directly from experiments and will help to optimize the process. The CFD simulations are also performed to analyze the influence of jet Reynolds number and plate materials on the heat transfer. The results show that the Leidenfrost temperature decreases with time over the radial positions and a similar trend is also observed for the maximum heat flux temperature. The detailed results are published, which is included in the publication section [1], the HLRN/NHR has been mentioned properly in this publication under section funding with the project-id.

Furthermore, the investigations are carried out to evaluate the quenching with two jets as a fundamental stage before modeling the nozzle field quenching. The single jet numerical model

has been further extended with two liquid jets. In this case, only half symmetry can be assumed. As in the case of single jet quenching, this numerical model has been validated with experiments. Accordingly, high-speed and infrared imaging have been performed. The validated model provides the technical parameters of the impinging surface such as cooling curves, heat flux, HTC, wetting front propagation, Leidenfrost temperature, maximum heat flux temperature, etc. However, for the quenching with two jets, the region between the two jets is of higher interest, where a complex fluid film interaction occurs. The wetting front propagation at the outer zones behaves similarly to the single jet quenching. But the inner zone propagates faster after a certain time and an asymmetric trend has been observed. Furthermore, the influence of jet Reyolds number, nozzle spacing, plate materials, etc. has been investigated.

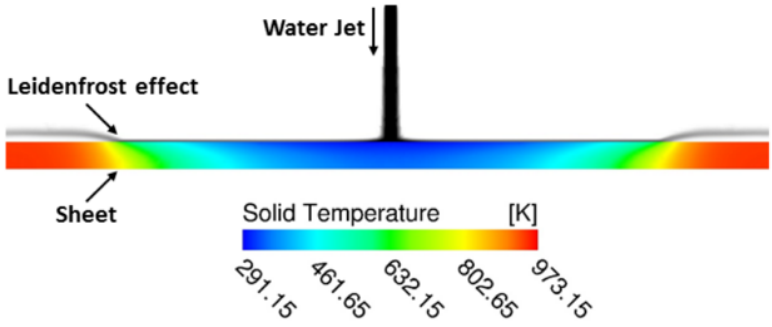

Figure 1: Numerical results from the stationary plate quenching process with single jet

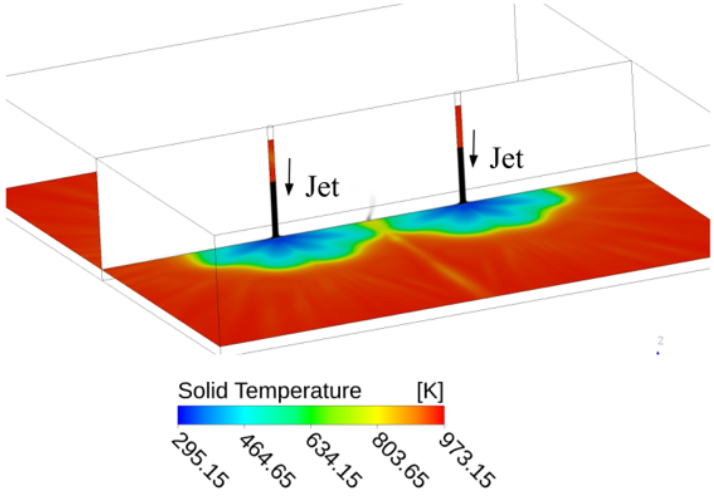

Figure 2: Numerical results from the stationary plate quenching process with two jets

Outlook

The developed numerical models can be further extended to simulate the quenching of nozzle fields. As a next step, the quenching with four jets is planned. The quenching process for nozzle arrays can have different configurations such as inline and staggered configurations. Since a full 3D-simulation is expected in this case, a smaller domain will be adopted for the simulations to reduce the computational effort.

In addition, the quenching of a moving metal plate is also planned in this project. For this purpose, the already developed single jet quenching model will be further extended to include the moving plate case. Preliminary investigations show that the extension with the sliding mesh concept is reasonable, since the dynamic meshing demands a remeshing of the entire computational domain at each time step. This can lead to a very high computational effort. For

this reason, the sliding mesh concept is further considered in this study. Once the numerical model is validated, this model can be used to investigate the influence of process parameters such as the jet Reynolds number, plate velocity, plate thickness, subcooling, initial plate temperature etc.

Publications

1. N. M. Narayan, U. Fritsching, *Investigation of the hydrodynamic and thermodynamic behavior of the liquid jet quenching process,* Heat and Mass Transfer (Springer), 1-24 (2024), doi.org/10.1007/s00231-024-03447-2

5.10 *hbk00059*: Joint state-parameter estimation for the Last Glacial Maximum with CESM1.2

HLRN Project ID:	hbk00059
Run time:	II/2017 – III/2024
Project Leader:	Prof. Dr. Michael Schulz
Project Scientists:	Dr. Tamás Kovács, Dr. André Paul
Affiliation:	Fachbereich Geowissenschaften, MARUM--Zentrum für Marine Umweltwissenschaften, Universität Bremen

Overview

This compute project is set within the framework of PALMOD, a BMBF-funded project that seeks to understand climate system dynamics and variability during the last glacial cycle. Specific topics are: i) to identify and quantify the relative contributions of the fundamental processes which determined the Earth's climate trajectory and variability during the last glacial cycle, ii) to simulate with comprehensive Earth System Models (ESMs) the climate from the peak of the last interglacial (the Eemian warm period) up to the present, including the changes in the spectrum of variability, and iii) to assess possible future climate trajectories beyond this century during the next millennia with sophisticated ESMs tested in such a way.

In the current phase, our main focus is on the direct forward modeling of stable water isotopes, combined with a comprehensive analysis of reconstructed and simulated isotope distribution. For this, we are using a global and comprehensive Earth system model: the Community Earth System Model version 1.2, in its isotope-enabled configuration (Brady et al. 2019). This version can provide stronger constraints regarding model-data comparison than simulations of only the basic physical variables without the explicit simulation of isotopes.

Results

The main outcome of this compute project in the previous year was the analysis of the mechanism behind a multi-centennial oscillation in the strength of the Atlantic Meridional Overturning Circulation (AMOC) in our model simulation for the Marine Isotope Stage 3 (MIS3), and the assessment of the sensitivity of such oscillations in the model with regard to the applied boundary conditions. The MIS3 lasted from about 60 to 27 thousand years before present, and is characterized by climate variability on different time scales: most notably, by climate transitions between cold stadial and warm interstadial states on a multi-millennial time scale called Dansgaard-Oeschger events. Our MIS3 simulation uses boundary conditions and greenhouse gas and orbital forcing representative of 38 thousand years before present, and has been integrated to 5500 years.

According to Fig. 1, the model results show the AMOC oscillating with a period of about 500 years; the strength of the upper, North Atlantic Deep Water cell of the AMOC, defined here as the maximum value of the meridional barotropic streamfunction below 500 meters in the Atlantic Ocean at 30°N, varies between 16 and 20 Sv (Sverdrups; 1 Sv = 10^6 m^3s^{-1}) when we apply a 100 years low-pass filter to remove sub-centennial signals from the series. Comparing the variations of AMOC strength with the time series of Atlantic northward salt fluxes on Fig. 1 we find a negative correlation at 5°N and a positive correlation at 35°N. This is very similar to the results of Prange et al. (2023) who identified a salt-oscillator mechanism behind the glacial AMOC variability in their simulation using the same model as we apply in this compute project.

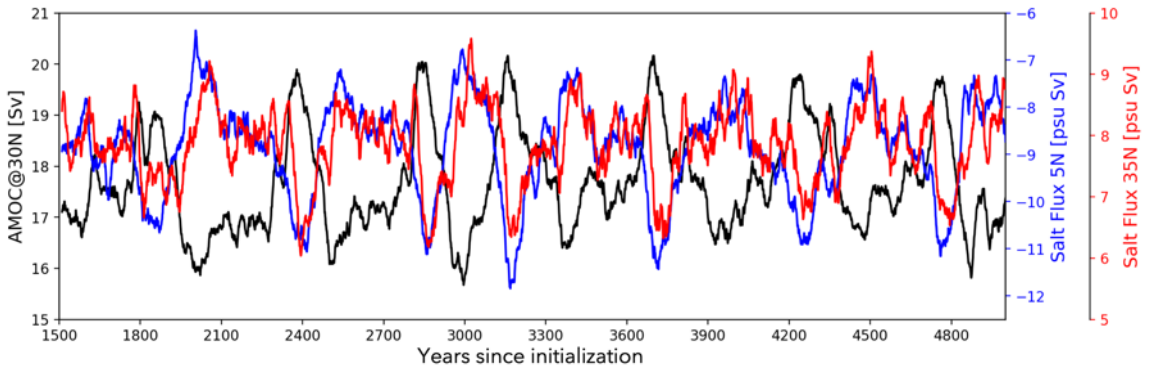

Figure 1: Simulated time series of maximum AMOC strength at 30°N (black) and total integrated northward advective salt flux across 5°N (blue) and 35°N (red) in the Atlantic Ocean.

In order to quantitatively explain the mechanism behind the AMOC variability, we have used a supervised machine learning method called causal discovery. This method analyses timeseries of variables that stand for the proxies of physical processes that potentially drive the AMOC oscillation and identifies causal connections among them. The PCMCI causal discovery framework (Runge et al, 2019) used here is based on the combination of the PC algorithm to find causal relationships between actors and their time lags by using partial correlations, and the Momentary Conditional Independence Test to quantify the strength of the causal links. Our results here are generated using the extended PCMCI+ algorithm that is able to detect contemporaneous links too in addition to lagged causal links (Runge, 2020).

Following the salt-oscillator mechanism presented by Prange et al. (2023), we have chosen annual mean time series of AMOC strength, northward salt advection in the Atlantic at 5°N and at 35°N, and the mean Atlantic salinity averaged between 5-35°N and integrated vertically over the top 1 km as the variables for causal discovery. The results are shown in Fig. 2, where the on the causal graph, the colored nodes and edges stand for the auto-MCI and cross-MCI, respectively, while the straight lines denote instantaneous links and the curved lines with number indicate lagged causal links.

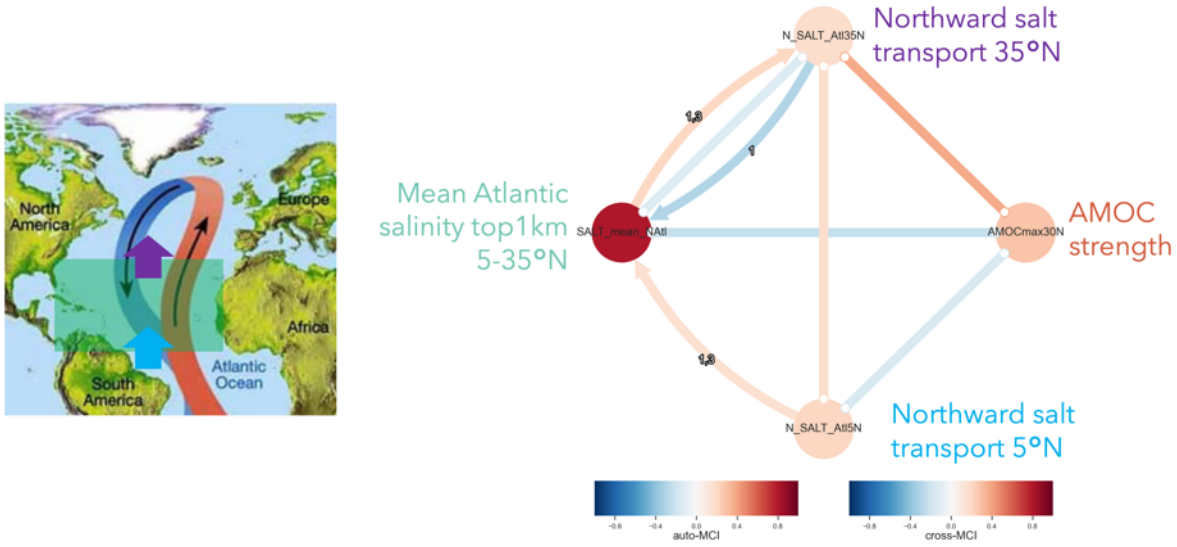

Figure 2: Causal graph of the timeseries of maximum AMOC strength and key variables (right): mean Atlantic salinity averaged between 5-35°N and integrated vertically over the top 1 km (green on map on left), and the total integrated northward advective salt fluxes across 5°N and 35°N (purple and light blue arrows on map on left).

Following the edges counter-clockwise on the causal graph on Fig. 2 reveals that an increase in AMOC strength is associated with a decrease in northward Atlantic salt transport across 5°N, corresponding to an increase in low-salinity Antarctic Intermediate Water advection. This causes the mean tropical Atlantic salinity to decrease, which in turn causes a reduction in northward salt transport at 35°N. This means fresher water advection to key deep water formation areas in the North Atlantic Ocean and is therefore positively linked with the AMOC strength or in other words is associated with a weakening AMOC. A decrease in its strength is associated with increased salinity advection and deep water formation, leading to the AMOC strengthening again. This scheme qualitatively illustrates the salt-oscillator mechanism behind the oscillatory behaviour.

Previous work suggests that the AMOC variability is sensitive to the applied boundary conditions, in particular the greenhouse gas forcing. This is confirmed by our transient MIS3 simulation that uses time variant orbital and greenhouse gas forcing based on Köhler et al. (2017). The bottom panel of Fig. 3 shows that our steady-state MIS3 simulation uses a constant CO_2 value representative of 38 thousand years ago (210.4 ppm) while it varies with time in our transient run, first increasing to about 212 ppm within 300 years, and then gradually decreasing again. Comparing the AMOC strength in both simulations on the top panel of Fig. 3 it is apparent that while the radiative CO_2 forcing is similarly high to that of the steady-state run, oscillations occur in the transient simulation too, but the AMOC becomes stable once the CO2 drops below about 207 ppm.

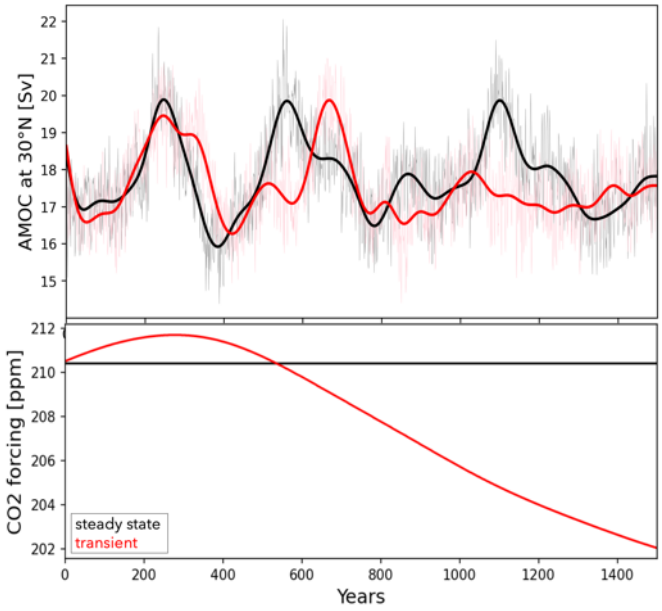

Figure 3: Simulated time series of maximum AMOC strength at 30°N (annual series in thin line, 100 years low-pass filtered series in thick line, top panel) and the applied CO_2 forcing (bottom) in our steady-state (black) and transient (red) MIS3 experiments.

Outlook

In the coming year we are planning to run further transient simulations targeting different periods of the last glacial cycle, such as for Heinrich Stadial I and the Bolling-Allerod.

References

1. Brady, E., Stevenson, S., Bailey, D., Liu, Z., Noone, D., Nusbaumer, J., Otto-Bliesner, B. L., Tabor, C., Tomas, R., Wong, T., Zhang, J., Zhu, J, (2019): *The connected isotopic water cycle in the Community Earth System Model version 1*. Journal of Advances in Modeling Earth Systems, *11, 2547–2566.*

2. Köhler, P., Nehrbass-Ahles, C., Schmitt, J., Stocker, T. F., and Fischer, H. (2017): *A 156 kyr smoothed history of the atmospheric greenhouse gases CO2, CH4, and N2O and their radiative forcing*, Earth System Science Data, 9, 363–387, https://doi.org/10.5194/essd-9-363-2017.
3. Prange, M., Jonkers, L., Merkel, U., Schulz, M., Bakker, P, (2023): *A multicentennial mode of North Atlantic climate variability throughout the Last Glacial Maximum*. Science Advances 9-44, eadh1106, doi: 10.1126/sciadv.adh1106.
4. Runge, J., Bathiany, S., Bollt, E., Camps-Valls, G., Coumou, D., Deyle, E., et al. (2019): *Inferring causation from time series in earth system sciences*. Nature Communications, 10(1), 1–13. https://doi.org/10.1038/s41467-019-10105-3,
5. Runge, J. (2020): *Discovering contemporaneous and lagged causal relations in autocorrelated nonlinear time series data sets*. In Conference on uncertainty in artificial intelligence (pp. 1388–1397).

Presentations

1. T. Kovacs, M. Prange, U. Merkel, D. Latinovic, A. Paul, M. Schulz, Glacial AMOC variability in CESM. PalMod General Assembly, Bremerhaven, 27-29 September 2023.

5.11 *hbk00062:* Retrieval of stratospheric ozone profiles from OMPS observations in limb geometry and long-term trends

HLRN Project ID:	hbk00062
Run time:	IV/2017 – IV/2023
Project Leader:	Dr. Alexei Rozanov
Project Scientists:	Dr. Carlo Arosio, Dr. Alexei Rozanov
Affiliation:	Institute of Environmental Physics, University of Bremen

Overview

Stratospheric ozone recovery is expected during the 21st century according to model studies, as a consequence of the decreasing emission of chlorine-containing ozone depleting substances (ODSs) and the increasing concentration of greenhouse gases in the troposphere. To monitor the status of the ozone layer and the onset of its recovery, satellite measurements are an important tool, as they provide observations with high temporal and spatial resolution. In particular, measurements in limb geometry, as performed by SCIAMACHY (SCanning Imaging Absorption spectroMeter for Atmospheric Chartography) and OMPS-LP (Ozone Mapping and Profiler Suite – Limb Profiler), enable the study of ozone profiles with a vertical resolution of about 3 km. However, single satellite missions are generally too short to assess long-term ozone changes and the merging of several time series is required. Several studies using satellite merged data sets detected positive trends in the upper stratosphere, particularly at mid-latitudes: a hint of the ozone recovery.

In this framework, the main activities within this project are related to the retrieval of ozone profiles from OMPS-LP observations, from 2012 till present. The merging with the SCIAMACHY time series enabled the study of altitude-, latitude- and longitude-resolved ozone changes over the last 20 years. The validation with independent data sets showed a general good quality of the produced data set. Improvements in the retrieval of ozone profiles have been a goal of this project; the release of a new version of Level 1 OMPS-LP data required the re-processing of the entire data set, which improved the stability of time series. The comparison of the obtained trends with simulations from a chemistry transport model (CTM) is an example of the usage of the created data set and is also presented in the report.

Results

The improvement of the retrieved ozone profiles is a goal of this project and the quality of the profiles has been validated against independent measurements. To this aim, ozonesonde measurements are particularly valuable up to 30 km, whereas observations from the MLS (Microwave Limb Sounder) satellite instrument offer a valuable reference from 18 up to 60 km. Over the last years, the agreement with ozonesondes in the lower stratosphere was improved, with average discrepancy within 10%.

An issue that has been tackled in 2023 is the drift affecting OMPS-LP time series with respect to independent satellite observations, e.g. from MLS, that was identified in the last years, particularly in the upper stratosphere. In the left panel of Fig.1, the drift between OMPS-LP and MLS time series is shown as a function of altitude and latitude, in terms of % per decade, over 2012-2023. We notice large positive values up to 5-6 % per decade around 35-40 km. The NASA team has recently implemented some calibration corrections, a wavelength registration adjustment and improved the pointing knowledge of the intrument. The entire data set was re-processed on HLRN with the main aim to mitigate the drift. The result is shown in the right panel of Fig.1: the drift of the time series retrieved using the new version of L1 (2.6)

data has absolute values strongly reduced, within 3 % per decade, with respect to the previous version.

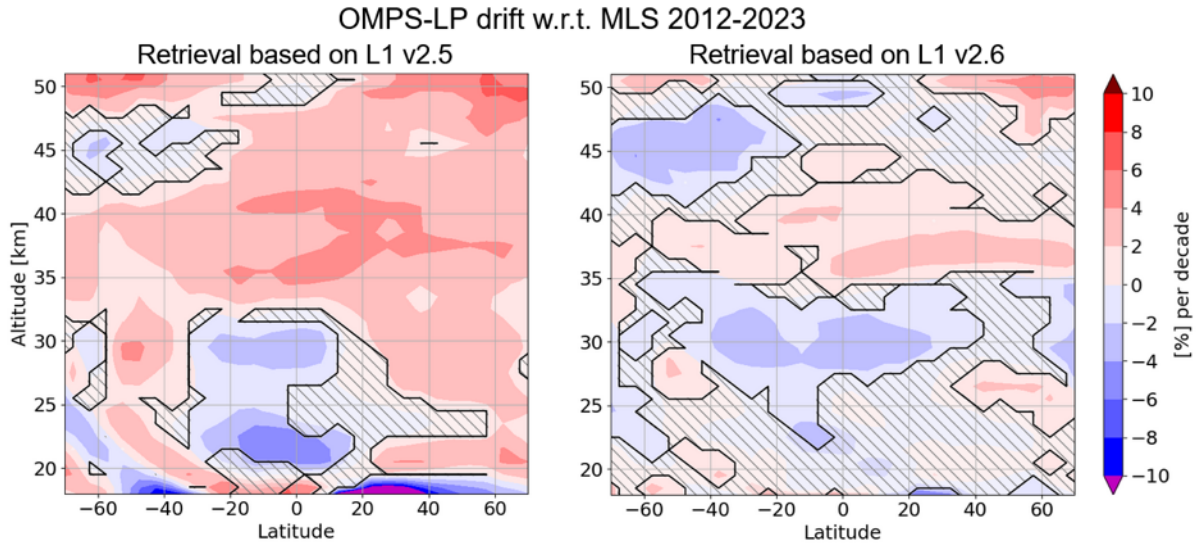

Figure 1: Drift of the OMPS-LP time series with respect to MLS data as a function of latitude and altitude over the period 2012-2021. On the left panel, the ozone retrieval was performed using the older version of L1 data (v2.5), on the right panel, using the new (v2.6) version of the data provided by NASA.

Application of the merged data set

By merging SCIAMACHY and OMPS time series, we obtained an ozone data set (SCIA+OMPS) starting from 2003, vertically resolved every 3.3 km, and spatially binned every 5° latitude and 20° longitude. This enables the study of longitude-resolved structures and changes in the ozone distribution. To compute trends, a standard multi-linear regression approach was used, accounting for proxies like El Nino, QBO and solar activity. Recently a collaboration with the University of Leeds, made possible a comparison of the satellite trends with simulations of the TOMCAT CTM. The interest was to check whether the model reproduces the zonal asymmetries in trends at northern high latitudes and better understand their driving mechanisms. To this aim, we also computed seasonal trends, changes in the temperature field, and investigated changes in the position and strength of the polar vortex.

A good agreement between the CTM and the satellite trends was generally found. Large asymmetries are seen in winter and spring months at northern high latitudes, as displayed in Fig. 2. During summer (JJA, middle column) the trend fields are fairly homogeneous over longitude, displaying significant positive values of about 1 % per decade for SCIA+OMPS and close to zero for TOMCAT. In contrast, during spring (left column) and autumn (right column) the asymmetry is well pronounced. In particular, the strong zonal asymmetry in SCIA+OMPS spring-time trends is very well captured by TOMCAT, with the positive maximum located over the North Atlantic sector. The negative values between Scandinavia and Siberia are also statistically significant (at 2σ level) for both observations and model. A similar bi-polar pattern is also found in SO, but more confined to polar latitudes and shifted in longitude. The good agreement of TOMCAT with observations also holds in this case. Regarding temperature, in summer we find a close-to-zero negative trend, whereas in spring and autumn the pattern is also zonally asymmetric, however no strong correlation with the patterns observed in the ozone trends was found.

These findings and the study of changes in the stratospheric polar vortex, indicate a dynamical origin of the observed asymmetry, possibly related to a strengthening and a shift of the position of the polar vortex.

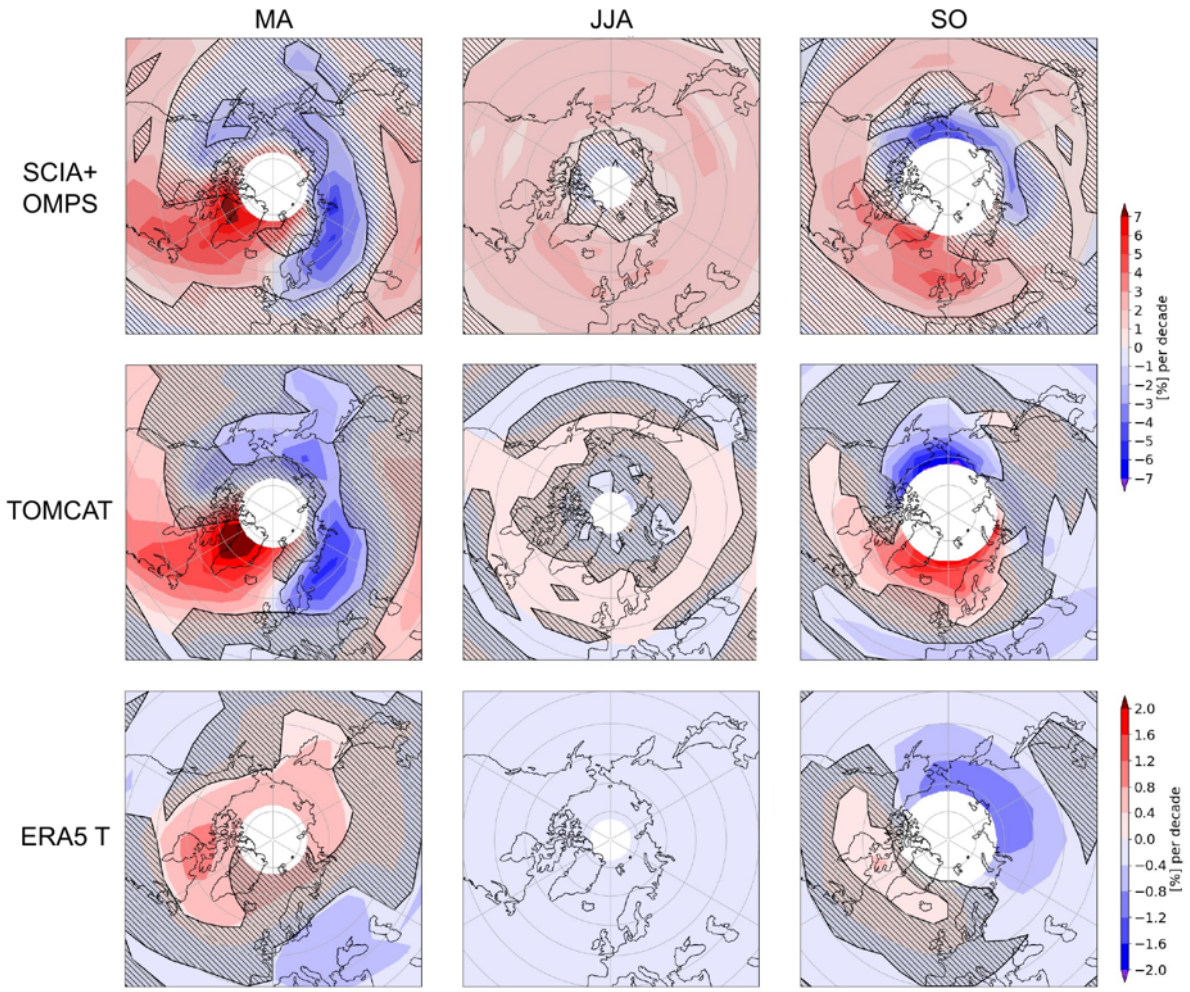

Figure 2: Long-term seasonal trends over 2004-2021 for spring months (MA), summer (JJA) and fall (SO) at 32 km: in the top row ozone trends from the SCIA+OMPS data set, in the second row, ozone trends from TOMCAT, and ont eh bottom temperature trends from ERA5. Shaded areas indicate non-significant values.

Outlook

The outlook for 2024 addresses three main points:

1. Investigate and mitigate the impact of Hunga Tonga volcanic eruption in January 2022 on our ozone retrieval. Test the possibility of improving the data quality in the southern hemisphere over 2022. This has the aim to reduce the artefact identified in ozone profiles, especially during the first 6 months after the eruption and affecting mostly the southern hemisphere.
2. Test and develop a working version of a retrieval algorithm to process observations performed by the new OMPS-LP instrument, which was launched at the beginning of November 2022 onboard the Joint Polar Satellite System-2 (JPSS-2).
3. Extend the current OMPS-LP time series including 2023-24 data to get a SCIA+OMPS merged time series, which will cover almost 22 years, i.e. an entire solar cycle. This enables the study of long-term ozone changes with a reduced impact of solar activity variations.

Publications

1. Arosio, C., et al. “Merging of ozone profiles from SCIAMACHY, OMPS and SAGE II observations to study stratospheric ozone changes”, Atmospheric Measurement Techniques, 12.4, (2019): 2423-2444.
2. Arosio, Carlo, et al. "Assessment of the error budget for stratospheric ozone profiles retrieved from OMPS limb scatter measurements." Atmospheric Measurement Techniques 15.20 (2022): 5949-5967.
3. Weber, Mark, et al. "Global total ozone recovery trends attributed to ozone-depleting substance (ODS) changes derived from five merged ozone datasets." Atmospheric Chemistry and Physics 22.10 (2022): 6843-6859.
4. Arosio, Carlo, et al. "Investigating zonal asymmetries in stratospheric ozone trends from satellite limb observations and a chemical transport model." Authorea Preprints (2023).

Presentations in 2023

1. Arosio, C., et al. Investigating zonal asymmetry in stratospheric ozone trends at northern high latitudes using satellite limb observations and CTM simulations, EGU General Assembly 2023, Vienna, 24–28 Apr 2023, EGU23-7671, 2023 (PICO).
2. Arosio, C., et al..: Investigating the effects of inhomogeneities in surface reflectivity on stratospheric ozone retrieval from limb scattering observations, 12th SPARC Atmospheric Limb Workshop, Brussels, 22-26 May 2023, 2023 (Oral).
3. Arosio, C., et al. Investigating zonal asymmetry in stratospheric ozone trends at northern high latitudes using satellite limb observations and CTM simulations, IUGG General Assembly 2023, Berlin, 11-20 July 2023, 2023 (Oral)

5.12 *hbk00083:* Tipping points in the ecosystem of the 'new Arctic' Ocean

HLRN Project ID:	hbk00083
Run time:	I/2021 – III/2024
Project Leader:	Prof. Dr. B. Rost
Project Scientists:	Dr. L. Oziel
Affiliation:	Alfred-Wegener-Institute, Helmholtz Center for Polar and Marine Research, Bremerhaven, Germany

Overview

The project in itself is now entering a second phase as the first article called "Climate change and terrigenous inputs decrease the efficiency of the future Arctic Ocean's biological carbon pump" is now submitted and under consideration in *Nature Climate Change*[1,2]. The article's abstract is the following:

"The Arctic experiences climate changes that are among the fastest in the world and affect all Earth system components. Despite expected increase in terrigenous inputs to the Arctic Ocean, their impacts on biogeochemical cycles are currently largely neglected in IPCC-like models. We used a state-of-the-art high-resolution ocean biogeochemistry model, that includes carbon and nutrient inputs from rivers and coastal erosion, to produce twenty-first-century pan-Arctic projections. Surprisingly, even with an anticipated rise in primary production across a wide range of emission scenarios, our findings indicate that climate change leads to a counterintuitive 40% reduction in the efficiency of the Arctic's biological carbon pump by 2100, to which terrigenous inputs contribute 10%. Terrigenous inputs will also drive intense coastal CO2 outgassing, reducing the Arctic Ocean's carbon sink by at least 10% (33 TgC yr-1). These unexpected positive feedbacks, mostly due to accelerated remineralization rates, lower the Arctic Ocean's capacity for sequestering carbon."

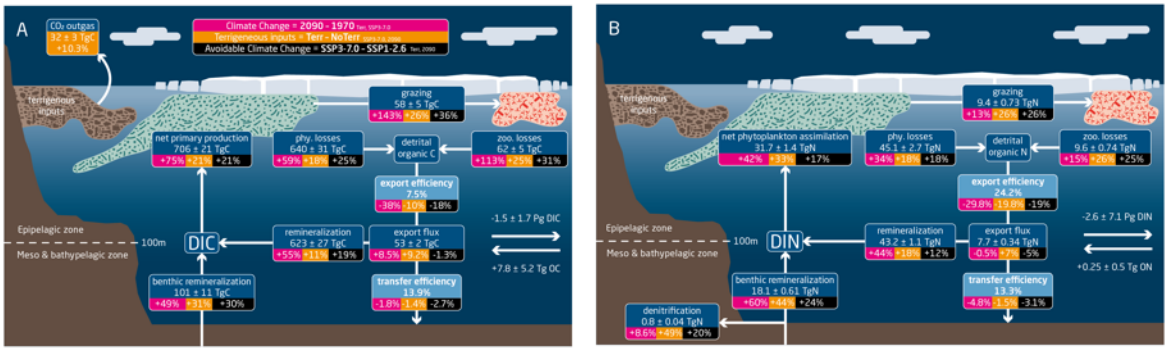

Figure 1: Simplified AO budget for A carbon and B nitrogen. Absolute quantities are expressed in carbon [TgC yr-1] and nitrogen [TgN yr-1] and refer to the baseline simulation Terr (with terrigenous inputs) by the end of the century (2090s). Relative contributions [%] of climate change (2090s relative to 1970s, with Terr, SSP3-7.0 emission scenario) and terrigenous inputs (Terr relative to NoTerr in the 2090s) are shown in red and orange. The avoidable contribution of climate change (SSP3-7.0 relative to SSP1-2.6 in the 2090s) is indicated within brackets. Phytoplankton (phy) losses encompass excretion and aggregation. Zooplankton (zoo) losses encompass mortality, excretion, sloppy feeding and fecal loss. Horizontal arrows on the right-hand side represent the transport with the adjacent seas. DIC and DIN stand for dissolved inorganic carbon and Nitrogen. Detrital organic matter encompasses both dissolved and particulate non-planktonic (detritus) pools.

The expensive high-resolution simulations that were used in this first high impact article (**Fig. 1**) will serve for a second article focusing on both the physical and biological carbon pumps in the Eurasian Arctic. In this region, “Atlantification” and subsequent warming and sea-ice loss are triggering one of the most rapid changes of the global ocean and affect water mass formation, in particular dense water formation. A change in dense water formation could affect the sequestration of carbon since they convey both organic and inorganic carbon, in a context of intense increase of CO_2 uptake and primary production.

Results and outlook

In our projections from several emission scenarios, we observe increase that despite increase warming, freshening and ‘lighter’ dense waters, our moderate to high-emissiom scenarios are projecting increase subdusction of dense waters which propagates further North and East, following the “Atlantification” path (**Fig. 2**). Indeed, surface waters get cooled efficiently in the absence of sea-ice, which forms more dense waters. In parallel, the same surface waters contain more organic and inorganic carbon because of respective increase of CO_2 uptake bythe ocean and primary production. As a result, we found more dense waters with higher carbon concentration on the European continental shelves. The dense waters are flowing out to the basins, cascading down the ocean bottom towards greater depth. Potentially, through those processes, our result will demonstrate that “Atlantification” will increase the sequestration of carbon in the Arctic Ocean.

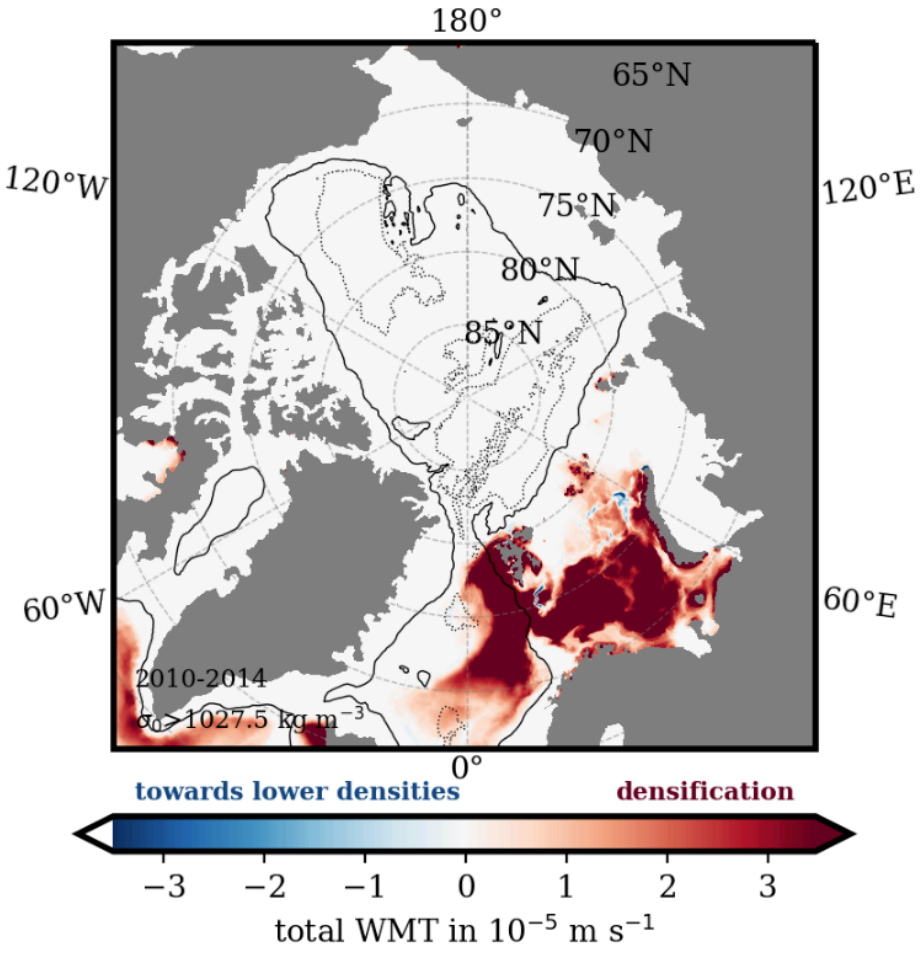

Figure 2: Example of water mass transformation diagnostics showing the areas where densw waters are forming (red areas). Those qualitative diagnostics will be accompanied by quantitative calculation of transport.

Publications

1. Oziel, L., Ö., Gürses, S., Torres-Valdés, C.J.M., Hoppe, B., Rost, O., Karakus, C., Danek, B., Juhls, C., Voelker, N., Koldunov, Q., Wang, M., Iversen, B., Koch, J., Hauck, J. 2024. *Climate Change and terrigenous inputs decrease the efficiency of the future Arctic Ocean's biological carbon pump*. [submitted to Nature Climate Change]

Presentations

2. Oziel, L. et al. *Climate Change and terrigenous inputs decrease the efficiency of the future Arctic Ocean's biological carbon pump*, invited speaker, Nansen Legacy Symposium, Tromsoe, Norway, 2023.

5.13 *hbk00084:* Marine biogenic aerosol precursors in the Arctic Ocean

HLRN Project ID:	hbk00084
Run time:	IV/2021 – III/2023
Project Leader:	Dr. Astrid Bracher
Project Scientists:	A. Bracher[1], M. Zeising, Ö. Gürses, J. Hauck, S. Loza, L. Oziel
Affiliation:	Alfred Wegener Institute, Helmholtz Centre for Polar and Marine Research, [1]also at Institute of Environmental Physics, University of Bremen

Overview

Biogenic aerosols from phytoplankton production localized in leads or open water were shown to act as potential cloud condensation nuclei or ice nuclei in remote regions. As extensive measurements of biogenic aerosol precursors are still scarce, we conduct a modeling study and explicitly simulate acidic dissolved polysaccharides (PCHO) and transparent exopolymer particles (TEP). As such, we integrate processes of algal PCHO exudation during phytoplankton growth or under nutrient limitation and processes of TEP formation into FESOM2.1-REcoM3, a coupled setup that has been optimized to provide a high resolution in the Arctic realm of state-of-the-art ocean circulation, sea ice physics, and marine biogeochemistry. We evaluate the model performance in terms of phytoplankton biomass, particulate organic carbon, PCHO, and TEP with remote sensing products and in-situ measurements. Further, we retrieve trends and regional hotspots of TEP formation in two simulations. Our results are considered to simulate organic aerosol formation and further cloud formation processes in the Arctic realm by our collaboration partners within the DFG Transregional Collaborative Research Centre TR 172 ArctiC Amplification: Climate Relevant Atmospheric and SurfaCe Processes and Feedback Mechanisms (AC)[3].

Results

The preceding efforts of the FESOM development team at AWI Climate Science division and of our developing REcoM team were of major advantage for this study. We could also profit from the project hbk00083 in the setup of the model on the HLRN HPC system and the tuning of initial model conditions. Simulations were caried out for two periods, one spanning the years 1958-2019, and the other 1950-2100, i.e., a total of 211 model years of which the periods 2000-2019 and 2014-2100 were evaluated.

Our model results suggest, so far, a clear seasonal succession of phytoplankton blooms (increased phytoplankton carbon, increased total Chlorophyll a), a release of PCHO, TEP production and remineralization. Computed climatological data of total Chlorophyll *a*, PCHO, and TEP are in good comparison to observation data, where these were available. In early summer, TEP formation closely follows the phytoplankton blooms, i.e., in Fram Strait and on the Siberian shelves. During summer, elevated TEP concentrations are found in the entire Arctic Ocean, which fit in-situ observation data from several campaigns. Further, there is a gradient of TEP from the shelves towards the Arctic Ocean basins during summer. In autumn, TEP are remineralized and concentrations decline. A rise of concentration in summer and quick decline in autumn is in accordance with observation data.

The first 30-year simulation reveals clear diverging trends in TEP (Fig. 1). In the Fram Strait, Barents Sea, and the Eurasian Basin, TEP concentrations mostly decline over time, while increases are observed in other parts of the Arctic Ocean, particularly in the Kara, Laptev, and

Beaufort Seas. The increase in TEP concentrations is most probably related to an increase in Net Primary Productivity (NPP) with a coinciding decrease in available nitrate concentration in the upper 30 m of the water column. This results in a stronger nutrient limitation of phytoplankton growth and leads to the exudation of organic carbon in accordance with the carbon overflow hypothesis.

The second simulation until the end of the century suggests a strong influence of the retreating sea ice edge on the formation of TEP (Fig. 2). There is a decrease of TEP in contemporary open water areas, as such, in the Fram Strait, Barents and Kara Seas along an overall NPP decrease in these regions. On the contrary, an increase of TEP is simulated in other Arctic seas and basins, which will become open water areas at the end of the century. A preliminary analysis of the simulation results suggest that this increase occurs along a NPP increase and decreasing silicate availability.

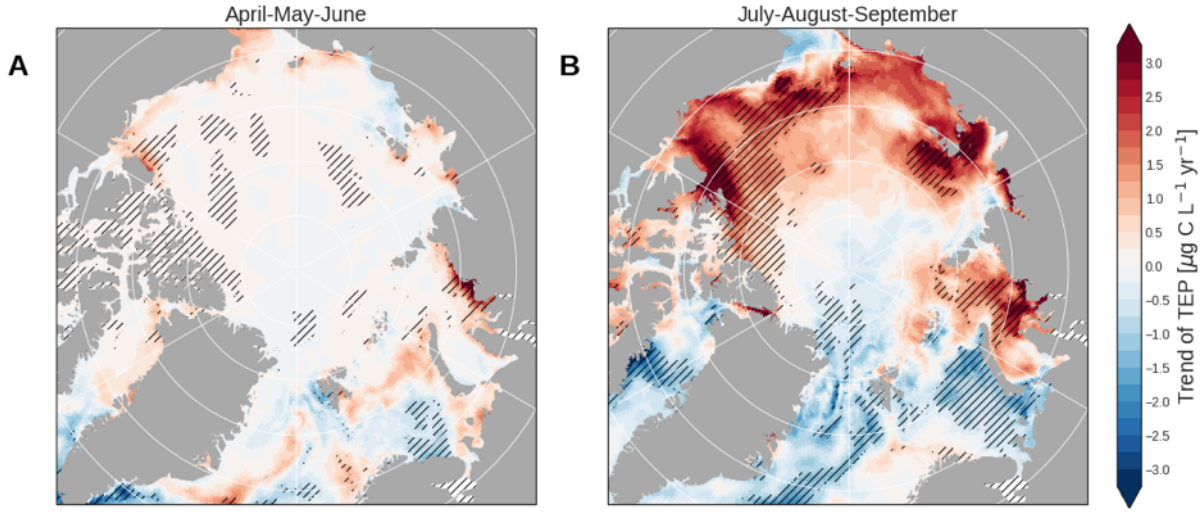

Figure 1: Maps of the trend of the period 1990-2019 of the simulated volume-weighted mean TEP concentration (0-30 m) of the months April-June (A) and July-September (B). Areas over which trends are significant (t-test, $p < 0.05$) are overlaid with hatching.

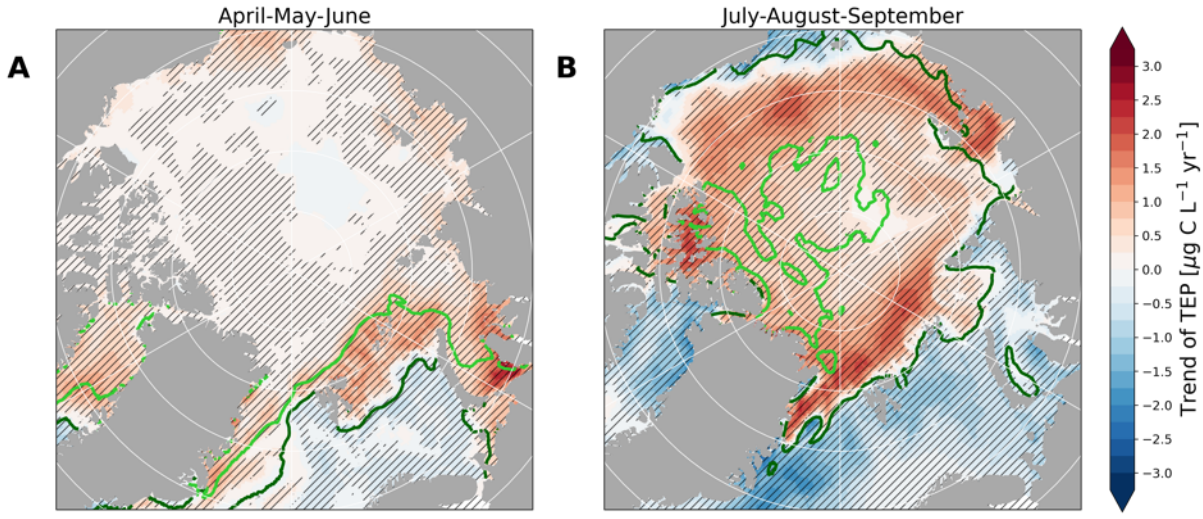

Figure 2: Maps of the trend of the period 2015-2100 of the simulated volume-weighted mean TEP concentration (0-30 m) of the months April-June (A) and July-September (B). Areas over which trends are significant (t-test, $p < 0.05$) are overlaid with hatching. Sea ice edge (mean SIC < 25%) of 2015-2020 depicted in dark green, and of 2095-2100 in light green.

Outlook

In our research, we integrated processes of PCHO and TEP formation into the ocean general circulation biogeochemistry model FESOM2.1-REcoM3 to study the production of biogenic aerosol precursors in the Arctic Ocean. This simulation resulted in a first description of TEP on large spatial and temporal scales in the Arctic realm, which can complement the sparse observation data available in this remote region.

As this is a first step to simulate TEP in the Arctic Ocean, the full complexity of TEP cycling is not yet represented in the model parametrization. Additionally, observational caveats of this study include the scarcity of sampling campaigns as well as the broad spatial and temporal range of studies and their differences in sampling depths and methodologies. These make it difficult to construct consistent time series for biogeochemical parameters from observational studies, which therefore limit the model evaluations.

However, this research paves the way for the implementation of these processes in Earth System Models and for research on the impact of marine biogenic aerosol precursors on the atmosphere in the context of intense climate change. The representation of marine organic aerosols in models could have large implications in a warming climate, by altering atmospheric radiative transfer through influences on cloud formation.

Publications, Presentations and Posters

1. Zeising, M., Oziel, L., Gürses, O., Hauck, J., Heinold, B., Losa, S., Thoms, S., van Pinxteren, M., Völker, C., Zeppenfeld, S., and Bracher, A.: *Wide-spread Occurrence and Increasing Trend of Biogenic Aerosol Precursors in the 3 Arctic Ocean Simulated by an Ocean Biogeochemistry Model*. Under review for publication in JGR Biogeoscience.
2. Zeising, M., Oziel, L., Hauck, J., Heinold, B., Losa, S., Thoms, S., van Pinxteren, M., Zeppenfeld, S., and Bracher, A. (2023/06/22). *Modeling Biogenic Aerosol Precursors in the Arctic Ocean: Occurrence patterns and long-term trends*. Poster, Helmholtz PoF Topic 6 Symposium. Bremerhaven, Germany.
3. Bracher, A., Richter, A., Blechschmidt, A., Bougoudis, I., Burrows, J., Losa, Svetlana, Pefanis, V., Zeising, M., and Zilker, B. (2023/06/27). *Atmospheric composition and ocean color feedback to Arctic amplification*. Poster, (AC)3 Evaluation Phase II. Cologne, Germany.
4. Zeising, M., Oziel, L., Hauck, J., Heinold, B., Losa, S., Thoms, S., van Pinxteren, M., Völker, C., Zeppenfeld, S., and Bracher, A. (2023/09/19). *Decadal trends in Arctic Biogenic Aerosol Precursors*. Conference Talk, International Conference for YOUNG Marine Researchers – ICYMARE. Oldenburg, Germany.
5. Zeising, M., Oziel, L., Hauck, J., and Bracher, A. (2023/12/05). *End-of-century Prediction of Marine Biogenic Aerosol Precursors*. Poster, (AC)3 General Assembly. Leipzig, Germany.

5.14 *hbk00085:* Modellierung des Einsetzens der letzten Eiszeit

HLRN-Projektkennung:	hbk00085
Laufzeit:	III/2023 – II/2024
Projektleiter:	Dr. M. Prange
Projektbearbeiter.	Dr. D. Latinovic
Institut / Einrichtung:	MARUM – Zentrum für Marine Umweltwissenschaften, Universität Bremen

Überblick

Das letzte Interglazial im Marinen Isotopenstadium (MIS) 5.5 zählt zu den wärmsten Phasen der jüngeren Erdgeschichte. Für diese Phase vor etwa 125.000 Jahren wurde eine globale Mitteltemperatur von fast einem Grad Celsius über dem vorindustriellen Wert rekonstruiert. Es wird angenommen, dass aufgrund teilweise geschmolzener Eisschilde in Grönland und der Antarktis der globale Meeresspiegel mit hoher Wahrscheinlichkeit 6-9 Meter höher lag als heute. Gegen Ende des MIS 5.5, zwischen etwa 120 und 115 Tausend Jahren vor heute, führte eine Abkühlung in den hohen Breiten schließlich zum Ende des Interglazials und dem Anwachsen kontinentaler Eisschilde, obgleich die atmosphärische Kohlendioxid-Konzentration erst verzögert ab etwa 115.000 Jahren vor heute abnahm. Ein deutlicher Rückgang des Meeresspiegels deutet in diesem Zeitraum auf ein signifikantes Eiswachstum über den Kontinenten hin. Für 110.00 Jahre vor heute, im MIS 5.4, wurde schließlich ein erster Meeresspiegel-Tiefstand von ca. 30 m unter dem heutigen Niveau rekonstruiert (Abb. 1). Eisschild-Rekonstruktionen weisen dabei auf erste bedeutende Vereisungen im Nordosten Kanadas und der Barents-Kara-See-Region hin.

Eine grundlegende Herausforderung beim Verständnis der Klimavariabilität über lange Zeiträume hängt mit den Mechanismen und Rückkopplungsprozessen im Erdsystem während vergangener Eiszeiten zusammen. Obwohl Klimamodelle eine Abkühlung der hohen Breiten gegen Ende des MIS 5.5 simulieren können, bleibt unklar, ob diese Abkühlungen in Bezug auf ihre Intensität, räumliche Verteilung und zeitliche Entwicklung realistisch dargestellt werden und ob gekoppelte Klima-Eisschildmodelle die rekonstruierten Vergletscherungen und die daraus resultierenden Meeresspiegeländerungen erfolgreich simulieren können. Unser Ziel in diesem Projekt ist es, mithilfe eines komplexen Klimamodells (CESM1.2; https://www.cesm.ucar.edu), das mit dem Eisschildmodell PISM gekoppelt ist (https://www.pism.io), die Phase des Einsetzens der letzten Eiszeit zu simulieren und dabei wichtige Rückkopplungsprozesse zu identifizieren.

Das Modell wird mit einer horizontalen Auflösung von 2 Grad für das Atmosphären-Landmodellgitter betrieben, während das Ozean-Meereisgitter eine räumlich variable Gitterweite von etwa 1 Grad in zonaler Richtung und bis zu 0,3 Grad in meridionaler Richtung aufweist. Die vertikale Struktur des Atmosphärenmodells besteht aus 30 Schichten, während der Ozean in der Vertikalen mit 60 Niveaus diskretisiert wird. Für das Eisschildmodell wird ein Gitter mit einer Auflösung von 20 km verwendet. Um das raumzeitliche Verhalten der nordhemisphärischen Eisschilde und deren Wechselwirkungen mit dem Atmosphäre-Ozean-System zu untersuchen, werden transiente Simulationen durchgeführt. Mithilfe einer asynchronen Koppelungstechnik können rechenzeitsparende beschleunigte Modellläufe ermöglicht werden.

Das Projekt ist Teil der durch das BMBF-finanzierten nationalen Klimamodellierungsinitiative PalMod-II.

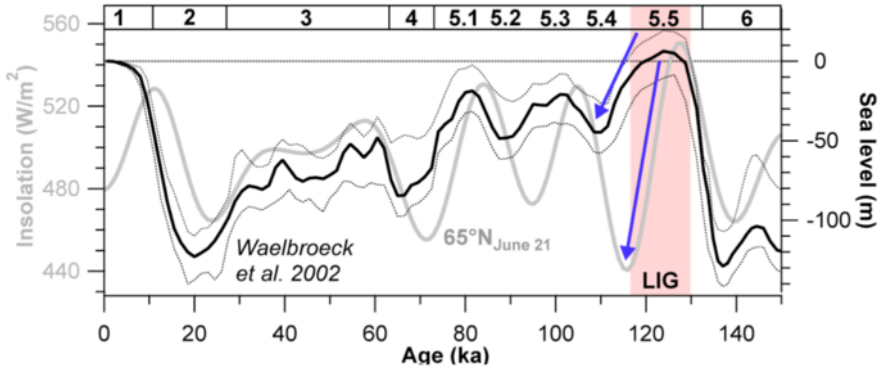

Figure 1: Rekonstruktion des globalen Meeresspiegels (schwarz) mit Unsicherheiten (gepunktet) über die letzten 150.000 Jahre. Darüber geplottet ist die sommerliche boreale Sonneneinstrahlung (grau). Das letzte Interglazial (LIG) ist rosa gekennzeichnet. Die blauen Pfeile heben die Abnahmen im Meeresspiegel und der solaren Einstrahlung am Ende des LIG hervor. Die verschiedenen Marinen Isotopenstadien (MIS) sind am oberen Rand der Abbildung angegeben (MIS 1 bis MIS 6).

Ergebnisse

Die wichtigsten Ergebnisse des Projekts aus den bisherigen Modellexperimenten lassen sich wie folgt zusammenfassen:

- Das gekoppelte Klima-Eisschild-Modell ist im Prinzip in der Lage, eine orbital getriebene Abkühlung in hohen Breiten und den Beginn der letzten Eiszeit zu simulieren.
- Änderungen der Treibhausgaskonzentrationen spielen eine untergeordnete Rolle für das Einsetzen der letzten Eiszeit, die in erster Linie durch Veränderungen der Achsenschiefe und der Präzession der Erde verursacht wurde (Erdorbitalparameter).
- Die Konfiguration (Initialisierung) der grönländischen Eisschildmodellkomponente im letzten Interglazial spielt eine untergeordnete Rolle für die nachfolgende Eisschildentwicklung außerhalb Grönlands.
- Eine genauere Analyse zeigt Unterschiede zwischen der simulierten und der rekonstruierten Eisschildverteilung, insbesondere ist das simulierte Eisvolumen (und damit der Meeresspiegelrückgang) kleiner als das rekonstruierte.

Grund für den geringen Eisaufbau in einigen Regionen sind Ungenauigkeiten in der Simulation des Oberflächentemperaturfeldes. Eine detaillierte Analyse ergab, dass die größten Abweichungen zwischen dem simulierten Eisaufbau und den Rekonstruktionen in Regionen auftreten, in denen signifikante Unterschiede zwischen den simulierten Oberflächentemperaturen des Kontrolllaufs (aktuelles Klima) und den Beobachtungen (Klimatologie) festgestellt wurden, was als "climate biases" bekannt ist. Ein Beispiel hierfür ist das östliche Kanada, wo das Modell zu hohe Sommertemperaturen simuliert, oder Sibirien, wo das Modell einen "cold bias" aufweist. Um dieses Problem weiter zu beleuchten und ggfs. zu beheben wurde eine Klimakorrektur („climate bias correction“) eingeführt. In dieser Korrektur werden simulierte Temperaturanomalien des Paläozustands gegenüber dem heutigen simulierten Klimazustand berechnet und auf ERA5-Reanalyse-Temperaturfelder addiert. Für Niederschlag wurde derselbe additive Ansatz gewählt sowie alternativ ein multiplikativer Ansatz. Es hat sich aber in weiteren Experimenten gezeigt, dass Niederschlagskorrekturen nur einen geringen Einfluss auf die Ergebnisse haben, sondern vielmehr Temperaturkorrekturen ausschlaggebend sind. Transiente Simulationen des Eiszeitbeginns mit Temperaturkorrektur konnten somit einen Eisaufbau liefern, der besser mit Rekonstruktionen übereinstimmt als die nicht-korrigierten Simulationen. Eine Darstellung der

nordhemisphärischen Verteilung der Eismassen zum Zeitpunkt 112 ka vor heute, als das Eisvolumen sein vorläufiges Maximum erreichte, wird in Abb. 2 für eine korrigierte und eine nicht-korrigierte Simulation gezeigt. Im nicht-korrigierten Lauf (Abb. 2a) erstrecken sich die Eismassen über den Kanadisch-Arktischen Archipel, die Baffin-Insel, die Kara-Barentssee-Region und die ostsibirischen Inseln. Im Vergleich zu Rekonstruktionen zeigt das Modell eine Unterschätzung der Vereisung in der Barents-Kara-See-Region und fehlende Vergletscherung in den Gebieten Quebec-Labrador, Keewatin und Skandinavien. Im Experiment mit Bias-Korrektur (Abb. 2b) bleibt das gesamte Eisvolumen ähnlich, jedoch gibt es in bestimmten Regionen einige signifikante Unterschiede zum nicht-korrigierten Lauf. Insbesondere ist der Eisaufbau in der Region der ostsibirischen Inseln moderater. Zudem zeigt sich eine erste leichte Vergletschung im nördlichen Quebec, was ebenfalls eine Verbesserung der Simulation darstellt. Im transienten Lauf mit Bias-Korrektur wurden dieselben Modellparameter wie im nicht-korrigierten Lauf verwendet. Daher wurde mit einer weiteren Neukalibrierung des Eisschild-Modells auf Basis des bias-korrigierten Klimas begonnen. Anschließend wurde ein transienter, bias-korrigierter Lauf mit dem rekalibrierten Modell durchgeführt. Dabei wurde ein Meeresspiegelrückgang von ca. 12 Metern simuliert. Obwohl dieser Wert im Vergleich zu den in Rekonstruktionen noch immer relativ gering ist, ist er dennoch konsistent innerhalb der vorhandenen Unsicherheiten.

Im weiteren Verlauf des Projekts werden weitere Sensitivitätsexperimente mit Parameterkalibrierungen durchgeführt und die transienten Simulationen bis ins MIS 5.2 (vgl. Abb. 1) fortgesetzt.

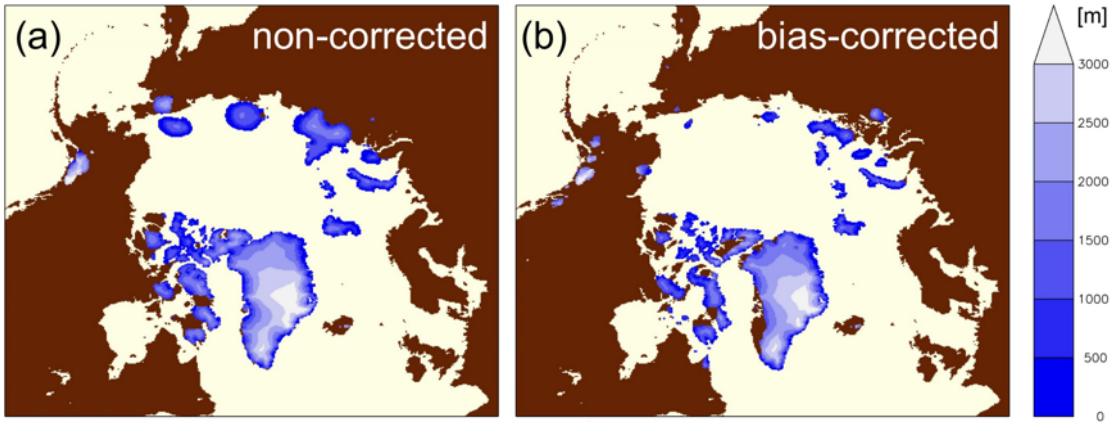

Figure 2: Simulierte Eisverteilung in der Nordhemisphäre aus beschleunigt-transienten gekoppelten Klima-Eisschild-Simulationen mit CESM-PISM für das Zeitintervall 123-110 ka. Gezeigt sind die Eishöhen für 112 ka aus dem Lauf (a) ohne Klimakorrekturen und (b) mit Klimakorrekturen („temperature bias correction“).

Publikationen

1. Crow, B., L. Tarasov, M. Schulz, M. Prange, *Uncertainties originating from GCM downscaling and bias correction with application to the MIS-11c Greenland Ice Sheet*, Climate of the Past, 20, 281-296 (2024).

5.15 *hbk00090:* Paleoclimate Applications of Mixing Parameterizations in an Earth System Model

HLRN Project ID:	hbk00090
Run time:	II/2023 – I/2024
Project Leader:	Prof. Dr. Michael Schulz, Dr. André Paul
Project Scientists:	Heves Pilatin, Siva Kattamuri
Affiliation:	MARUM – Center for Marine Environmental Sciences, University of Bremen

Overview

Studying past climates is crucial for understanding the changes in the global climate system over time and for projecting future climate scenarios. Nevertheless, reconstruction of the ocean circulation and mixing processes of past climates is challenging due to the uncertainties in paleoclimate records. Tidal mixing in ocean models is represented by ocean mixing parameterizations that govern turbulent mixing based on fundamental physical principles. Although baroclinic tidal energy (internal waves) is the main source of mixing in the deep ocean (half of 2 TW mechanical energy required to maintain the global abyssal stratification), many of these parameterizations do not focus on internal wave energetics (Wilmes et al., 2021). Instead, they use constant diffusivities (Munk, 1966) or depth-dependent diffusivities (Bryan and Lewis, 1979; Cummins et al., 1990) to represent the tidal-induced mixing in the interior ocean. Olbers & Eden (2013) introduced the Internal Wave Dissipation, Energy, and Mixing (IDEMIX) model to parameterize the energy dissipated from the internal wave breaking using the radiative transfer equation. IDEMIX is an energetically consistent mixing parameterization where all the resolved and parameterized forms of internal wave energy are linked without any spurious sources and sinks in the wave field.

In this study, we performed simulations for two extreme past climate simulations the Last Glacial Maximum (~21 ka, LGM) and mid-Createcous (~90 Ma) with an energetically consistent framework by using the IDEMIX scheme in the Community Earth System Model (CESM) to evaluate the tidal mixing and global overturning circulation.

Last Glacial Maximum (~21 ka)

Being the most recent glacial period of Earth's history where the global ice-sheet coverage reached a maximum extent, the LGM is an important and one of the most studied paleo times. The large volume of ice caused an approximately 130 m drop in sea level and exposure of the continental shelves, enabling the tidal dissipation energy that sinks in the present-day shelf seas to shift to the open ocean during the LGM (e.g., Egbert et al., 2004; Schmittner et al., 2015; Wilmes et al., 2019, 2021). Following this hypothesis, the LGM ocean is expected to be more turbulent and well-ventilated in the abyssal and possibly have a much stronger overturning circulation in the North Atlantic compared to the pre-industrial (PI) (Schmittner et al., 2015; Wilmes et al., 2019). In this study, we test this hypothesis for the global circulation and marine biogeochemical processes of LGM by using IDEMIX in the climate model. The new experiments with IDEMIX were started by using the initial conditions from existing LGM simulations performed with the compute project *hbk00059*.

mid-Cretaceous (~90 Ma)

The mid-Cretaceous is known for being one of the warmest phases in the last 500 million years. With a different continental distribution and higher atmospheric CO_2 concentration compared to the present day, temperatures were higher and the global mean sea level was elevated by around 160 m (Lunt et al., 2016; Muller et al., 2008) during this period. This caused the continental shelves to be submerged, creating shallow regions where tidal energy could be dissipated. The objective of this sub-project is to understand the effect of tidal energy dissipation on ocean mixing and circulation for the geophysical conditions of this period by using IDEMIX in CESM. The boundary conditions for the coupled model setup had to be prepared from scratch and the simulations were spun up for over 3000 model years to reach quasi-equilibrium.

Results

The vertical diffusivity in PI and LGM is maximized in the deep ocean (by two to three orders of magnitude) with the IDEMIX parameterization (**Figure 1**), supporting the IDEMIX concept on the enhanced energy transfer from internal wave breaking to dissipation over the rough bathymetry. While the turbulence is localized only at the abyssal of the northern tropics without IDEMIX, the model produces more diverse and boosted mixing everywhere at the ocean bottom with IDEMIX. This indicates that the PI and LGM tides do not make a notable difference in the mixing between two oceans using the default parameterization (K-Profile parameterization, Large et al., 1994). However, when IDEMIX is applied, the LGM tides which are stronger than the PI tides, produce a more vigorous ocean. The effect of IDEMIX can be seen not only at the bottom but also in the upper ocean. At the locations where the tidal dissipation energy is strong, the vertical diffusivity increases through the entire water column (e.g., mid-Atlantic ridges and subpolar regions).

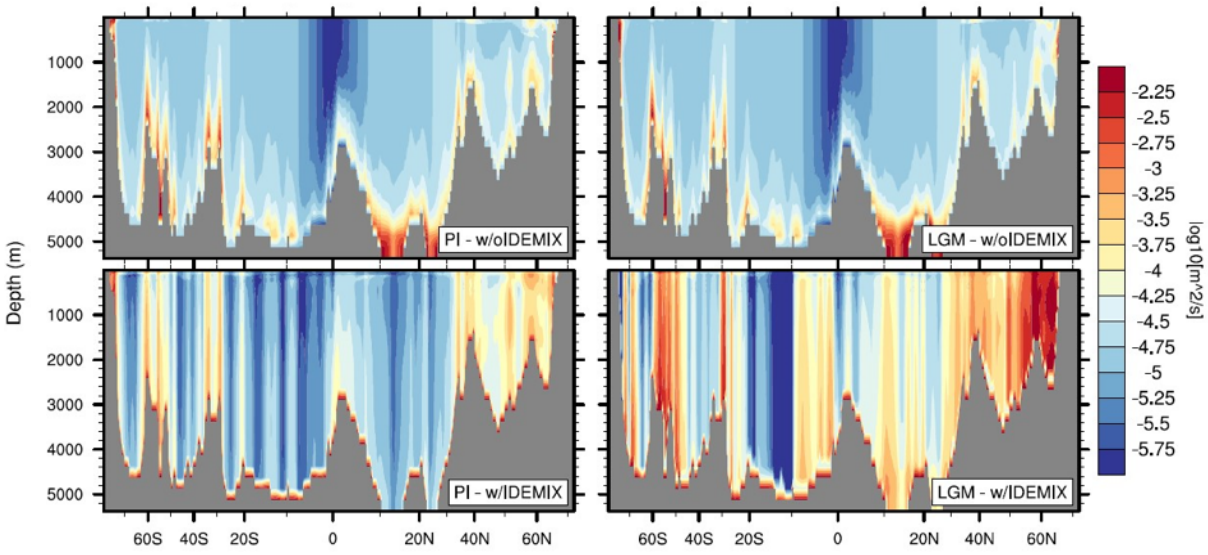

Figure 1: Vertical diffusivity transects along 30°W for PI and LGM ocean without IDEMIX (top) with IDEMIX (bottom)

The preliminary results from two mid-Cretaceous simulations with and without IDEMIX parameterization are compared here (**Figure 2**). IDEMIX calculates diffusivity throughout the water column in the ocean thus producing a diverse distribution. Whereas in the absence of a tidal mixing component, the constant background mixing parameters create layers of homogeneous diffusivity along the depth of the ocean. Also, IDEMIX increases diffusivity over rough topography and decreases it over smooth topography compared to a constant background diffusivity experiment. But despite the change in diffusivity, both experiments yield

a similar overturning circulation pattern (**Figure 3**) where a pronounced wind-driven circulation can be observed close to a surface and an overall weak overturning in the deep ocean. This could mean that the circulation is driven by factors other than the changes in the vertical diffusivity in the deep ocean.

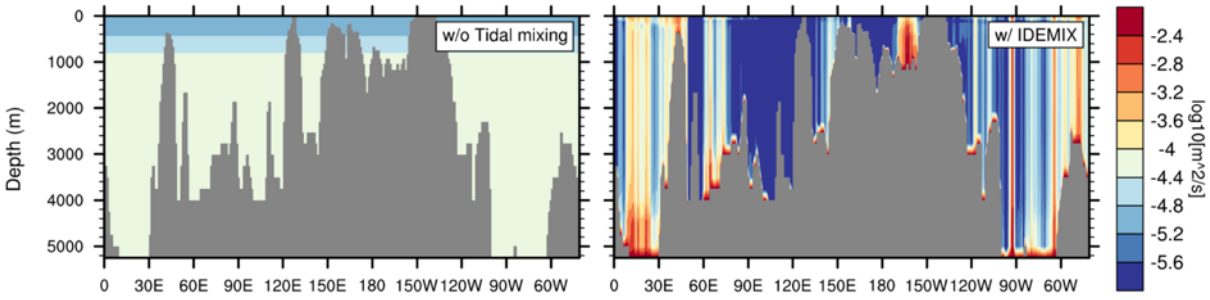

Figure 2. Profile of vertical diffusivity at 63°S in mid-Cretaceous simulations without the tidal mixing component (left) and with IDEMIX (right)

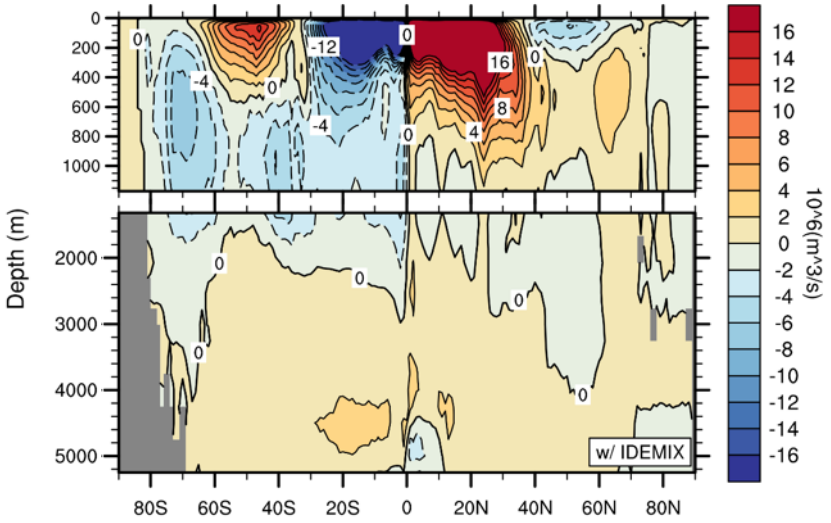

Figure 3: Global Meridional Overturning Circulation for mid-Cretaceous simulation with IDEMIX

Presentations

1. Siva Kattamuri, André Paul, Friederike Pollmann, Michael Schulz. *Modelling the ocean circulation of the mid-Cretaceous using the Community Earth System Model (CESM) and IDEMIX*. EGU General Assembly 2023, Vienna, 23-28 April 2023.
2. Heves Pilatin, André Paul, Friederike Pollmann, Michael Schulz; *Studying ocean circulation and biogeochemical processes during the Last Glacial Maximum*. EGU General Assembly 2023, Vienna, 23-28 April 2023.

References

Bryan, K., and L. J. Lewis (1979), A water mass model of the World Ocean, *J. Geophys. Res.*, 84(C5), 2503–2517, doi:10.1029/JC084iC05p02503.

Danabasoglu, G., Lamarque, J.-F., Bacmeister, J., Bailey, D. A., DuVivier, A. K., Edwards, J., et al. (2020). The Community Earth System Model Version 2 (CESM2). *Journal of Advances in Modeling Earth Systems*, 12, e2019MS001916. https://doi.org/10.1029/2019MS001916

Egbert, G. D., R. D. Ray, and B. G. Bills (2004), Numerical modeling of the global semidiurnal tide in the present day and in the last glacial maximum, *J. Geophys. Res.*, 109, C03003, doi:10.1029/2003JC001973.

Large, W. G., J. C. McWilliams, and S. C. Doney (1994), Oceanic vertical mixing: A review and a model with a nonlocal boundary layer parameterization, *Rev. Geophys.*, 32(4), 363–403, doi:10.1029/94RG01872.

Lunt, D. J., Farnsworth, A., Loptson, C., Foster, G. L., Markwick, P., O'Brien, C. L., et al. (2016). Palaeogeographic controls on climate and proxy interpretation. *Climate of the Past*, 12(5), 1181–1198. doi:10.5194/cp-12-1181-2016

Müller, R. D., Sdrolias, M., Gaina, C., Steinberger, B., & Heine, C. (2008). Long-Term Sea-Level Fluctuations Driven by Ocean Basin Dynamics. *Science*, 319(5868), 1357–1362. https://doi.org/10.1126/science.1151540

Olbers, D. and Eden, C. (2013): A Global Model for the Diapycnal Diffusivity Induced by Internal Gravity Waves, Journal of Physical Oceanography, 43 (8), pp. 1759-1779. doi: 10.1175/JPO-D-12-0207.1

Schmittner, A., J. A. M. Green, and S.-B. Wilmes (2015), Glacial ocean overturning intensified by tidal mixing in a global circulation model. *Geophys. Res. Lett.*, 42, 4014–4022. doi: 10.1002/2015GL063561.

Walter H. Munk, Abyssal recipes, *Deep Sea Research and Oceanographic Abstracts*, Volume 13, Issue 4, 1966, Pages 707-730, ISSN 0011-7471, doi:10.1016/0011-7471(66)90602-4.

Wilmes, S.-B., Green, J. A. M. & Schmittner, (2019) A. Glacial ice sheet extent effects on tidal mixing and the global overturning circulation - Model Output. *Zenodo* doi:10.5281/zenodo.1139242

Wilmes, SB., Green, J.A.M. & Schmittner, A. Enhanced vertical mixing in the glacial ocean inferred from sedimentary carbon isotopes. *Commun Earth Environ* 2, 166 (2021). doi:10.1038/s43247-021-00239-y

5.16 *hbk00094:* The effects of Ocean Alkalinity Enhancement on the anthropogenic CO2 concentrations in the 21st century

HLRN Project ID:	hbk00094
Run time:	III/2023 – II/2024
Project Leader:	Prof. Dr. Björn Rost[1]
Project Scientists:	Tanvi Nagwekar[2], Dr. Cara Nissen, Dr. Judith Hauck
Affiliation:	Alfred Wegener Institute, Helmholtz Center for Polar and Marine Research, Bremerhaven, Germany.
	[1]principal investigator, also at the University of Bremen, [2]project administrator

Overview

The rise in atmospheric CO_2 concentrations due to the burning of fossil fuels and land use change leads to elevated global temperatures causing detrimental changes in the climate. Without reduction and control in the carbon emissions, global temperatures will exceed the Paris Agreement's 2°C limit (UNFCCC, 2015). Hence, to limit temperature increases and mitigate climate change, significant carbon emission reductions and exploration of various Carbon Dioxide Removal (CDR) methods are necessary (Friedlingstein et al., 2011). The oceans are a large carbon reservoir as CO_2 dissolves in and reacts with seawater (Zeebe and Wolf-Gladrow, 2001), and they act as a sink for anthropogenic CO_2 emissions (Gruber et al., 2019). The Southern Ocean and the North Atlantic are of crititcal importance as the formation of intermediate, deep and bottom waters occurs there, which is the bottle-neck of ocean carbon uptake. The subducting water masses in these regions can sequester carbon in the interior ocean on decadal to centennial timescales (Gruber et al., 2019; Sarmiento & Gruber, 2002).

Owing to the importance of the oceans in global carbon cycling, various marine CDR methods are being actively assessed. One such method is Ocean Alkalinity Enhancement (OAE; Hartmann et al., 2013). The rate at which CO_2 is naturally drawn down by the oceans due to its buffer capacity as a result of silicate rock weathering is two orders of magnitude too slow to compensate the current emission rates (Bach et al., 2019). Hence, the idea behind OAE is to accelerate this natural CO_2 uptake of the oceans by enhancing alkalinity through dissolution of processed alkaline minerals e.g., olivine or calcium carbonate (Hauck et al., 2016; Keller et al., 2014; Köhler et al., 2013). In response to the OAE, the carbonate system's equilibria are shifted, promoting the conversion of dissolved CO_2 into bicarbonate ions, thereby reducing the partial pressure of CO_2 at the sea surface which increases the influx of CO_2 from the atmosphere into the ocean (Hauck et al., 2013; Wolf-Gladrow et al., 2007).

In this project, our goal is to assess the efficiency of OAE with olivine dissolution in deep and bottom water formation areas in the Southern Ocean, Labrador Sea and the Norwegian Sea in comparison to the efficiency of global OAE, using FESOM2.1-REcoM3 simulations (Hauck et al., 2020; Scholz et al., 2019) forced with atmospheric output from the AWI Climate Model under the high-emission scenario SSP3-7.0 (Semmler et al. 2020). We run the OAE simulations in a setup with high resolution ~10 km in deep and bottom water formation regions.

Results

Previously, we have completed all the changes in the model code which were necessary for implementing OAE. The usage of the high-resolution mesh (BOLD) aids us to better understand the ocean dynamics in the polar oceans, which are the focus of our regional OAE experiments. This helps to study the impact of small-scale processes on ocean carbon uptake compared to simulations already carried out on a coarse resolution mesh (CORE). We completed a 104 years physics-only spin-up and have an exisiting 150 years spinup for biogeochemical fields on CORE mesh which is interpolated to the BOLD mesh. With these initial conditons, we finished the historical run from 1950 to 2014. Considering the first 40 years from the historical run as further spin-up time, physical and biogeochemical tracers have experienced a total of 144 and 40 years of spin-up on the high-resolution mesh, respectively. **In this reporting period**, using the spin-up we simulated the future scenario simulation from 2015-2100 under SSP3-7.0 emission scenario (Control simulation; without addition of olivine). The experiments for global and subduction regions OAE were branched off in 2030 from the control simulation (Figure 1a). Olivine deposition is accompanied by addition of nutrients like iron and silicic acid along with alkalinity enhancement. We have conducted separate simulations for only alkalinity addition and for the addition of alkalinity combined with nutrients, both globally and in subduction regions. This enables us to discern the effects of alkalinity enhancement alone versus with nutrients on global and regional carbon uptake and storage efficiency. The global OAE simulations (2030-2100) are completed and the subduction region OAE simulations are ongoing (completed until year 2070; Figure 1a).

For the equal amount of olivine deposition globally (3 Pg olivine per year), the change in the CO_2 flux averaged over 2090-2099 due to the addition of alkalinity (GLO-ALK) relative to a control experiment without OAE is slightly higher on the CORE mesh (0.89 PgC/yr) than on the BOLD mesh (0.84 PgC/yr; Figure 1b). In the experiments with alkalinity+nutrient addition (GLO-ALK-NUT), the change in the CO_2 flux is equal (1.24 PgC/yr) for both setups (Figure 1b). This can be explained with differences across the setups in the evolution of absolute CO_2 fluxes in the control simulations, with CO_2 fluxes being marginally higher on the CORE mesh than on the BOLD mesh (by 0.1-0.2 PgC/yr; Figure 1a). For the OAE in subduction regions, the change in the CO_2 flux over 2060-2069 relative to the control is higher on the BOLD mesh (0.1 PgC/yr) than on the CORE mesh (0.06 PgC/yr; SUB-ALK experiment). Similarly, the SUB-ALK-NUT experiments show a higher carbon uptake on the BOLD mesh (1.4 PgC/yr) than on the CORE mesh (0.29 PgC/yr; Figure 1b). On the BOLD mesh, the subduction regions in the Southern Ocean are larger compared to the the ones on the CORE mesh (40.41 million km^2 on BOLD and 24.29 million km^2 on CORE mesh). These larger subduction regions lead to a higher amount of olivine deposition on the BOLD setup than the CORE setup (0.36 Pg olivine per year for BOLD mesh as compared to 0.22 Pg olivine per year for the CORE mesh). Thus, this explaines the higher CO_2 uptake on the BOLD mesh in the subduction regions as compared to the CORE mesh.

The CDR potential is calculated as the difference in the annual air-sea CO_2 flux between the OAE experiment and the CTRL simulation without OAE and divided by the total annual amount of olivine added in the surface ocean (PgC per Pg olivine). The CDR potential is similar for both setups both for global OAE and OAE in subduction regions (0.28-0.29 PgC per Pg olivine when only alkalinity is added; Figure 1d). Similarly, for experiments with nutrient addition, the global CDR potential is equal for BOLD and CORE setup (0.29 PgC per Pg olivine). In contrast, the SUB-ALK-NUT on the BOLD setup has a slightly higher CDR potential (1.4 PgC per Pg olivine) than the CORE setup (1.3 PgC per Pg olivine; Figure 1d). However, the CDR potential in the SUB-ALK-NUT experiments decreases with time for both setups (Figure 1c). In summary, while the subduction regions are as efficient for carbon uptake as the global ocean when only alkalinity is added, the subduction regions have a higher potential than the global ocean due to increased iron fertilization from olivine addition in the Southern Ocean.

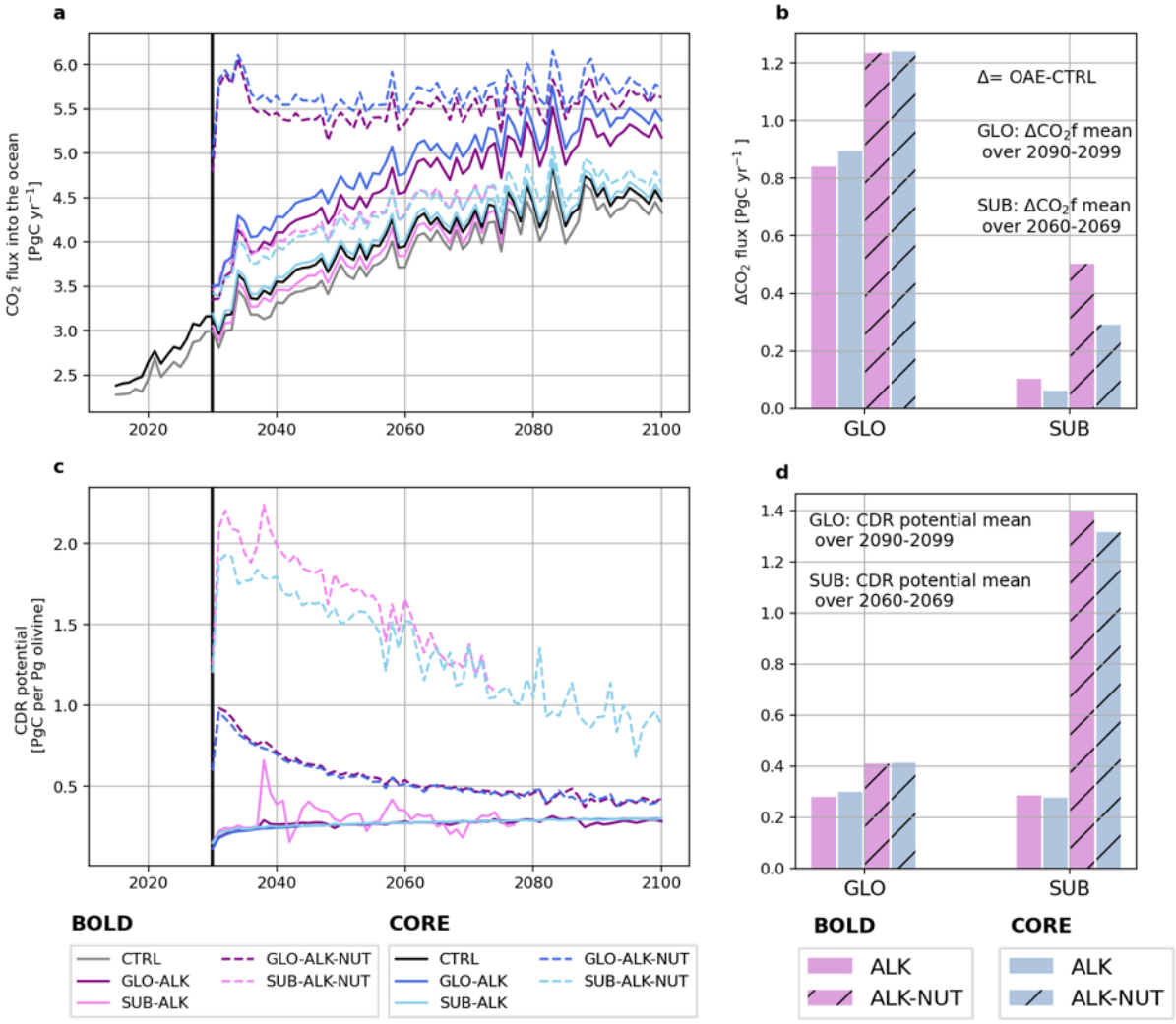

Figure 1: (a) Timeseries for oceanic CO_2 uptake [PgC/yr] in the different OAE experiments (see Figure legend and text). Positive values indicate a flux into the ocean. Shades of purple represent simulationsfor the BOLD setup and shades of blue represent simulations for the CORE setup. **(c)** Timeseries for CDR potential [PgC per Pg olivine]. **(b)** Bar plots representing the change in the CO_2 flux relative to the control simulation without OAE (ΔCO_2 flux) average dover 2090-2099 for the global OAE experiments and averaged over 2060-2069 for the subduction regions OAE experiments. **(d)** Bar plots representing CDR potential for global and subduction regions averaged over the same years as ΔCO_2 flux. Solid bars show simulations with alkalinity addition only and hatched bars show simlations with combined alkalinity and nutrient addition.

Spatially, the change in the CO_2 flux relative to the CTRL without OAE is evenly distributed in the areas where olivine is deposited for all simulations with only alkalinity addition (Figure 2a,b). For simulations with both alkalinity and nutrients added, the Southern Ocean shows the highest increase in carbon uptake for global OAE and OAE in the three subduction regions combined (Figure 2c,d). Nutrient fertilization in the Southern Ocean results in higher productivity and thus higher carbon uptake than in the other ocean regions. This pattern agrees with the change in the CO_2 flux simulated for OAE on the CORE mesh (Nagwekar et al., 2024, in review).

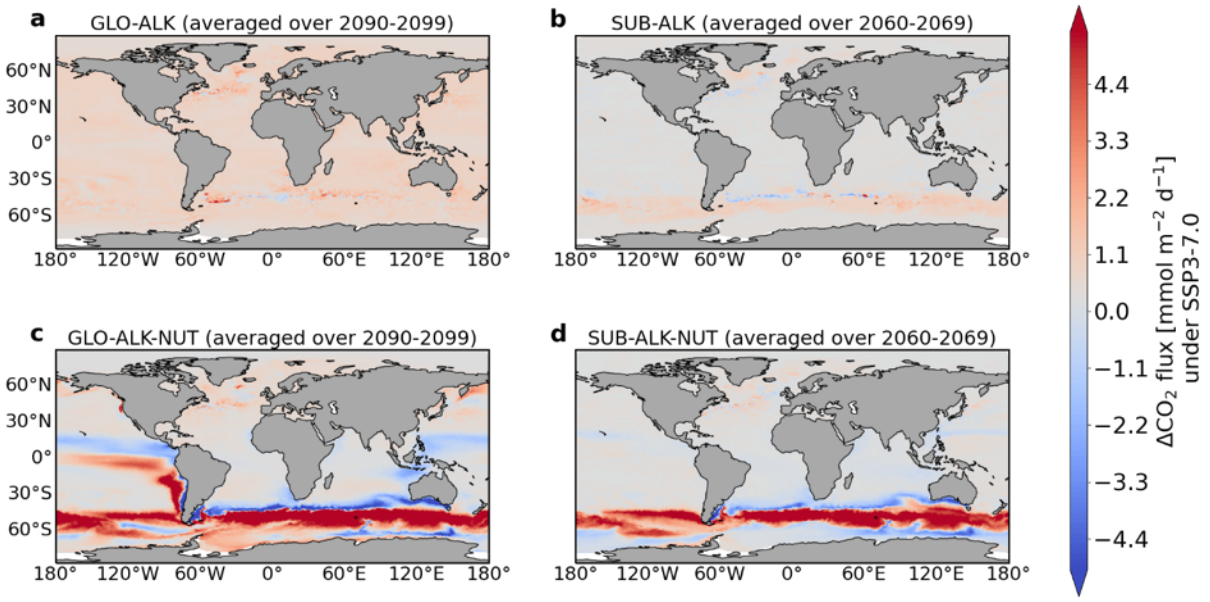

Figure 2: Spatial patterns for the difference in the CO_2 flux with respect to CTRL (ΔCO_2 flux) on the BOLD mesh averaged over 2090-2099 for **(a and c)** GLO-ALK and GLO-ALK-NUT and averaged over 2060-2069 for **(b and d)** SUB-ALK and SUB-ALK-NUT.

Outlook

Over the upcoming months, we will complete the OAE simulations in the subduction regions. We will also continue the analysis of the high-resolution simulations (BOLD mesh) to estimate the long-term efficiency of OAE, carbon storage and transfer capacity of the subduction regions as compared to the coarse resolution simulations (CORE mesh). This will include an analysis of regionally integrated fluxes in addition to the global analysis presented here. We will then assess the effects of small-scale processes, such as eddies on the overall CDR potential using the high-resolution simulations.

References:

Bach, L. T., Gill, S. J., Rickaby, R. E. M., Gore, S., & Renforth, P. (2019). CO2 Removal with Enhanced Weathering and Ocean Alkalinity Enhancement: Potential Risks and Co-benefits for Marine Pelagic Ecosystems. *Frontiers in Climate*, *1*. doi:10.3389/fclim.2019.00007

Friedlingstein, P., Solomon, S., Plattner, G.-K., Knutti, R., Ciais, P., & Raupach, M. R. (2011). Long-term climate implications of twenty-first century options for carbon dioxide emission mitigation. *Nature Climate Change*, *1*(9), Article 9. doi:10.1038/nclimate1302

Gruber, N., Clement, D., Carter, B. R., Feely, R. A., van Heuven, S., Hoppema, M., Ishii, M., Key, R. M., Kozyr, A., Lauvset, S. K., Lo Monaco, C., Mathis, J. T., Murata, A., Olsen, A., Perez, F. F., Sabine, C. L., Tanhua, T., & Wanninkhof, R. (2019). The oceanic sink for anthropogenic CO 2 from 1994 to 2007. *Science*, *363*(6432), 1193–1199. doi:10.1126/science.aau5153

Hartmann, J., West, A. J., Renforth, P., Köhler, P., De La Rocha, C. L., Wolf-Gladrow, D. A., Dürr, H. H., & Scheffran, J. (2013). Enhanced chemical weathering as a geoengineering strategy to reduce atmospheric carbon dioxide, supply nutrients, and mitigate ocean acidification: ENHANCED WEATHERING. *Reviews of Geophysics*, *51*(2), 113–149. doi:10.1002/rog.20004

Hauck, J., Köhler, P., Wolf-Gladrow, D., & Völker, C. (2016). Iron fertilisation and century-scale effects of open ocean dissolution of olivine in a simulated CO_2 removal experiment. *Environmental Research Letters*, *11*(2), 024007. doi:10.1088/1748-9326/11/2/024007

Hauck, J., Völker, C., Wang, T., Hoppema, M., Losch, M., & Wolf-Gladrow, D. A. (2013). Seasonally different carbon flux changes in the Southern Ocean in response to the southern annular mode. *Global Biogeochemical Cycles*, *27*(4), 1236–1245. doi:10.1002/2013GB004600

Keller, D. P., Feng, E. Y., & Oschlies, A. (2014). Potential climate engineering effectiveness and side effects during a high carbon dioxide-emission scenario. *Nature Communications*, *5*(1), 3304. doi:10.1038/ncomms4304

Köhler, P., Abrams, J. F., Völker, C., Hauck, J., & Wolf-Gladrow, D. A. (2013). Geoengineering impact of open ocean dissolution of olivine on atmospheric CO_2, surface ocean pH and marine biology. *Environmental Research Letters*, *8*(1), 014009. doi:10.1088/1748-9326/8/1/014009

Nagwekar, T., Hauck, J., & Nissen, C. (2024; In review). Ocean Alkalinity Enhancement in the deep water formation regions under low and high emission pathways

Sarmiento, J. L., & Gruber, N. (2002). Sinks for Anthropogenic Carbon. *Physics Today*, *55*(8), 30–36. doi:10.1063/1.1510279

Scholz, P., Sidorenko, D., Gurses, O., Danilov, S., Koldunov, N., Wang, Q., Sein, D., Smolentseva, M., Rakowsky, N., & Jung, T. (2019). Assessment of the Finite-volumE Sea ice-Ocean Model (FESOM2.0) – Part 1: Description of selected key model elements and comparison to its predecessor version. *Geoscientific Model Development*, *12*(11), 4875–4899. doi:10.5194/gmd-12-4875-2019

UNFCCC. (2015). *United Nations Framework on Climate Change (UNFCCC): Adoption of the Paris Agreement, 21st Conference of the Parties.* https://unfccc.int/resource/docs/2015/cop21/eng/l09r01.pdf

Wolf-Gladrow, D. A., Zeebe, R. E., Klaas, C., Körtzinger, A., & Dickson, A. G. (2007). Total alkalinity: The explicit conservative expression and its application to biogeochemical processes. *Marine Chemistry*, *106*(1), 287–300. doi:10.1016/j.marchem.2007.01.006

Publications and Presentations

Additional model experiments and the analysis of completed experiments are on-going, therefore there is no publication or presentation of the results yet.

5.17 *hbk00095:* Application of ensemble data assimilation for improved prediction of ocean ecosystem indicators

HLRN Project ID:	hbk00095
Run time:	III/2022 – II/2024
Project Leader:	Dr. Lars Nerger
Project Scientists:	Sophie Vliegen, Dr. Yuchen Sun
Affiliation:	Alfred-Wegener-Institut Helmholtz-Zentrum für Polar- und Meeresforschung, Bremerhaven

Overview

This project studies the effect of assimilating observations of ocean physics and biology onto the prediction of ecosystem indicators like particulate organic carbon, trophic efficiency, or dissolved oxygen. The ocean circulation model NEMO will be used in the NEMO-NORDIC configuration for the North- and Baltic Seas. The model is coupled to the ocean-biogeochemical model ERGOM. For the data assimilation, ensemble-based filters will be applied that are provided by the Parallel Data Assimilation Framework PDAF (Nerger and Hiller, 2013, https://pdaf.awi.de). The direct combination of NEMO-ERGOM with PDAF provides a highly-scalable data assimilation system that strongly benefits from the computational resources of the HLRN. Next to studying the influence of assimilating different ocean physics and biology observations onto the prediction of the ecological indicators, the effects of combined assimilation of physical and biological observations and of the application of linear ensemble Kalman filters and nonlinear particle-based filters will be assessed.

The work of this project is part Project SEAMLESS - Services based on Ecosystem data AssiMiLation: Essential Science and Solutions (https://www.seamlessproject.org) funded by the EU Horizon-2020 program. The aim of this project is to perform research to improve new and improved indicators of climate-change impacts and food security in marine ecosystems through the application of data assimilation. These developments will later be provided to the EU Copernicus Marine Service CMEMS (http://marine.copernicus.eu) which runs different operational marine forecasting centers. These developments will later be provided to the EU Copernicus Marine Service CMEMS (http://marine.copernicus.eu) which runs different operational marine forecasting centers.

Model System

In this project we use the ocean circulation model NEMO (Madec et al. 2008). NEMO is a widely used model for research but it is also used operationally at CMEMS. The particular variant of NEMO we use here is NEMO-NORDIC (Hordoir et al. 2019) in an upgraded version, which is based on NEMO 4.0 and uses a resolution of 1 nautical mile and 56 model layers. The Baltic Monitoring and Forecasting Center (BAL-MFC) performs operational services with this model. The configuration covers the full North Sea and Baltic Sea. The high resolution for the large regional domain provides a large potential for scaling by using domain-decomposition. In addition, the model setup uses the IO-Server XIOS to allow for efficient parallel IO. The biogeochemistry model is ERGOM (Neumann 2000, Maar 2011). The model simulates biogeochemical progresses and includes bacteria, two phytoplankton groups as well nutrients, zooplankton and detritus. In addition, a carbonate cycle allows to simulate the partial pressure of CO_2, pH, and particulate carbon.

In preparation of the project, we have already coupled PDAF directly into NEMO using the approach discussed by Nerger and Hiller (2013). By inserting subroutine calls that modify the model to become an ensemble model and by including an assimilation step, this approach allows for the best scalability and less disk output. In particulate, by keeping the ensemble information in memory the complete ensemble only needs to be written into files for model restarts. The dynamic ensemble integrations will be important for accurate error variance and covariance estimations for the data assimilation. During the last year, satellite observations of sea surface temperature (SST) and of total surface chlorophyll-a (CHL) provided by CMEMS are assimilated. The assimilation is performed daily using an ensemble of 30 model state realizations. The system runs fully parallel. Thus, the data assimilative model is configured to run 30 instances of NEMO-ERGOM, each using 2 compute nodes of the HLRN.

Results

The data assimilation is started at February 1, 2015 and runs until May 31, 2015. Figure 1 shows the observed and modeled surface chlorophyll (CHL) concentration on May 1. As Fig. 1e shows, on May 1, the observations nearly only available in the transition zone to the North Sea and in the central part of the Baltic Sea. Figure 1a shows the concentration without data assimilation (free run) with increased conccentrations in the central Baltic. The panels b to d of Fig. 1 show the effect when assimilating only single observation types, or both jointly. Assimilating only SST data has a limited effect on the chlorophyll. The overall best result is obtained when both data types are jointly assimilated (Fig. 1d).

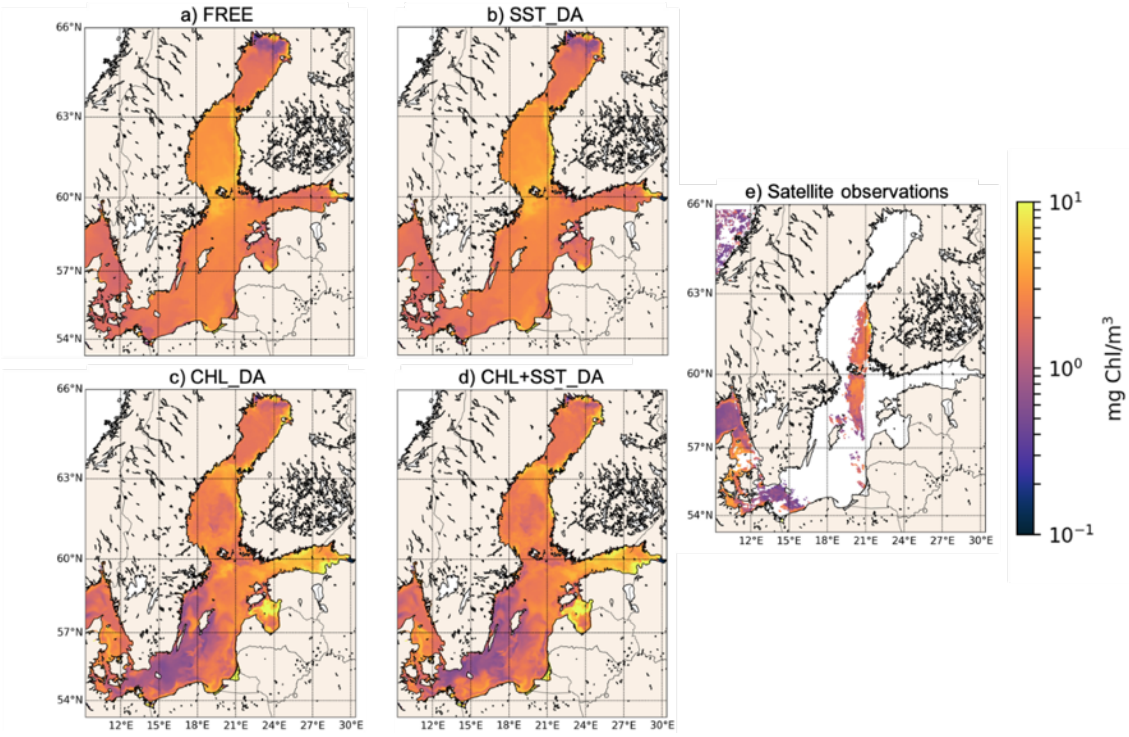

Figure 1: Chlorophyll in the Baltic Sea on May 1, 2015. Shown are (a) the free run and forecasts from experiments (b) assimilation of only SST data (SST_DA), (c) assimilation of only chlorophyll data (CHL_DA), (d) combined assimilation (CHL+SST_DA), and (e) the observed chlorophyll concentration.

A particular focus of the project is on the station 'Arkona Basin' which is located at (13.87°E, 54.88°N) in the Southern Baltic just north of the island of Rügen. Figure 2 shows the development of the surface chlorophyll concentration and SST at this station for the period January to May 2015. The free run shows that a phytoplankton bloom starts already at the beginning of February. Compared to the observations, the model overestimates the

concentrations during the bloom. The assimilation of chlorophyll data reduces this overestimation. The temperature is overall already well represented by the model. However, theassimilation of SST data reduces the deviation of the model from the satellite data.

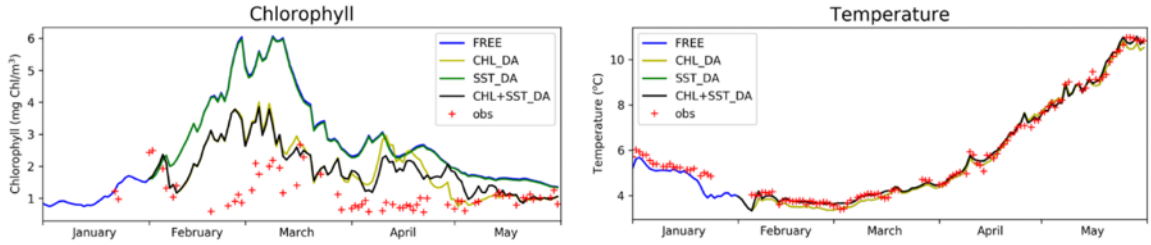

Figure 1: Development of the concentration of surface chlorophyll (left) and surface temperature (light) at the station Arkona. The lines show the different experiments: (blue) free ensemble run; (light green) assimilation of chlorophyll, (dark green) assimilation of SST; (black) combined assimilation of chlorophyll and SST. The red crosses show the satellite observations.

Presentations

Y. Sun, S. Vliegen, L. Nerger. Assimilation of satellite temperature and chlorophyll observations for improved ecosystem predictions in the Baltic Sea. *18th International EnKF Workshop 2023*, Norheimsund, Norway, May 2-5, 2023

S. Vliegen, Y. Sun, L. Nerger. Assessment of weakly and strongly coupled data assimilation in ocean-biogeochemical modeling. *International Symposium on Data Assimilation*, Bologna, Italy, October 16-20, 2023.

L. Nerger, Y. Sun, S. Vliegen. Improving ocean ecosystem predictions by coupled data assimilation of physical and biogeochemical observations. *10th EuroGOOS International Conference*, Galway, Ireland, October 2-5, 2023

References

Nerger, L., Y. Sun, S. Vliegen (2023). Improving ocean ecosystem predictions by coupled data assimilation of physical and biogeochemical observations. in *Proceedings of the 10th EuroGOOS International Conference. European Operational Oceanography for the ocean we want - Addressing the UN Ocean Decade challenges*. 3-5 October 2023, Galway, Ireland. Eparkhina, D., Nolan, J.E. (Eds). EuroGOOS, Brussels, Belgium. hdl:10793/1883

Nerger, L., Hiller, W. (2013). Software for Ensemble-based Data Assimilation Systems - Implementation Strategies and Scalability. *Computers and Geosciences*, 55, 110-118. doi:10.1016/j.cageo.2012.03.026

Madec, G., 2012: NEMO ocean engine, Version 3.3. Note du Pôle de modélisation, Institut Pierre-Simon Laplace (IPSL), 27.

Hordoir, R., et al., 2019, Nemo-Nordic 1.0: a NEMO-based ocean model for the Baltic and North seas – research and operational applications, Geoscientific Model Development, 12, 363-386, https://doi.org/10.5194/gmd-12-363-2019

Neumann T (2000) Towards a 3D-ecosystem model in the Baltic Sea. J Mar Syst 25:405–419

Maar, M., E. F. Moller, J. Larsen, K. S. Madsen, Z. Wan, J. She, L. Jonasson, and T. Neumann, 2011: Ecosystem modelling across a salinity gradient from the North Sea to the Baltic Sea. Ecological Modelling, 222, 1696–1711.

The SEAMLESS project has received funding from the European Union's Horizon 2020 research and innovation programme under grant agreement No. 101004032

5.18 *hbk00096:* Tropical Climate Variability of the Past

HLRN Project ID:	hbk00096
Run time:	IV/2022 – IV/2023
Project Leader:	Dr. Ute Merkel
Project Scientists:	Donghao Li
Affiliation:	MARUM - Zentrum für Marine Umweltwissenschaften, Universität Bremen

Overview

It is still under debate how future anthropogenic climate change will impact the tropics and their role in the global climate system and how tropical climate variability will respond to a warmer mean climate state. Insights into such conditions warmer than today can be achieved from fossil shallow-water corals which represent one of the most valuable climate archives. They allow to reconstruct climate variability beyond the instrumental record and for various climatic periods in the past.

A synthesis by Felis (2020) of coral proxy records for several warm periods in the past (130-118 and 6-2 kiloyears before present), i.e. from the Last Interglacial and from the mid-to-late Holocene, suggests different characteristics of seasonality and interannual-to-multidecadal variability during the course of these warm episodes. Sea-surface temperature as well as sea-water salinity information derived from tropical fossil corals, however, might arise from a superposition of local-to-regional processes and tropical climate modes connecting the Atlantic, Pacific and Indian Ocean basins. The mechanisms shaping the coral signals are only partially understood so far. Furthermore, the limited length of coral records is often restricted to only a few decades and may lead to misinterpretations of coral-derived shorter-term variability, e.g. on interannual timescales, which may be superposed by low-frequent variability operating on inter-decadal to centennial timescales.

Global earth-system model simulations bear the potential to put local coral signals into a larger-scale perspective of tropical climate dynamics. They also allow to provide a more detailed picture of the response to paleoclimatic boundary conditions, such as greenhouse-gas concentrations and orbital settings, for past warm periods. In particular, such simulations can shed light on the hydrologic cycle and contribute to the understanding of climate modes, such as the El Niño/Southern Oscillation phenomenon (ENSO) in the tropical Pacific for selected periods of the past. This is of particular relevance since previous modelling efforts have shown ambiguous results with respect to the strength of ENSO under future climate warming scenarios (Brown et al., 2020).

To this end, this project focusses on conducting high-resolution simulations using the water isotope-enabled Community Earth System Model (iCESM) version 1.2 for the Holocene and the Last Interglacial. A specific characteristic of iCESM1.2 consists in tracking stable water isotope ratios through all the components of the hydrologic cycle, thereby taking into account the physics of fractionation during condensation and evaporation processes. The project aims at insights into the tropical hydrologic cycle on interannual-to-multidecadal timescales and atmospheric teleconnections and at disentangling ENSO sensitivity from a paleoclimatic perspective.

The experiments in this project are conducted at a comparatively high resolution in the paleoclimate modelling context. A horizontal resolution of 1° in the atmosphere and land components and nominally 1° in the ocean (0.5° and 1.125° in the latitudinal and longitudinal

directions, respectively) are used. The vertical discretization is configured to 30 levels in the atmosphere and 60 levels in the ocean model component. Instead of long transient simulations at coarser resolution, a timeslice approach is followed in order to account for the higher computational needs at higher model resolution. This allows to better resolve the spatio-temporal scales recorded in the fossil coral material against which the model results will be compared.

The project is part of the DFG Priority Programme SPP 2299 “Tropical Climate Variability & Coral Reefs”.

Results

As a first step, a high-resolution (1°) multi-centennial pre-industrial control simulation with iCESM1.2 has been conducted at NHR@ZIB in order to test the role of the horizontal resolution for a better representation of the mean (hydro-)climate and its variability both globally and in the tropical Atlantic-Pacific realm. To this end, a coarser-resolution (2°) iCESM1.2 simulation also conducted at NHR@ZIB is used for comparison. Multi-year averages of precipitation patterns over the tropical Pacific realm for the boreal summer season (Fig. 1, top panels) demonstrate the importance of higher horizontal resolution to represent detailed regional-scale rainfall characteristics, e.g. in topographically complex regions such as northwestern South America or the Maritime Continent. The analysis of simulated precipitation patterns with regard to model biasses against reanalysis data (Fig. 1, bottom panels) is subject of ongoing work.

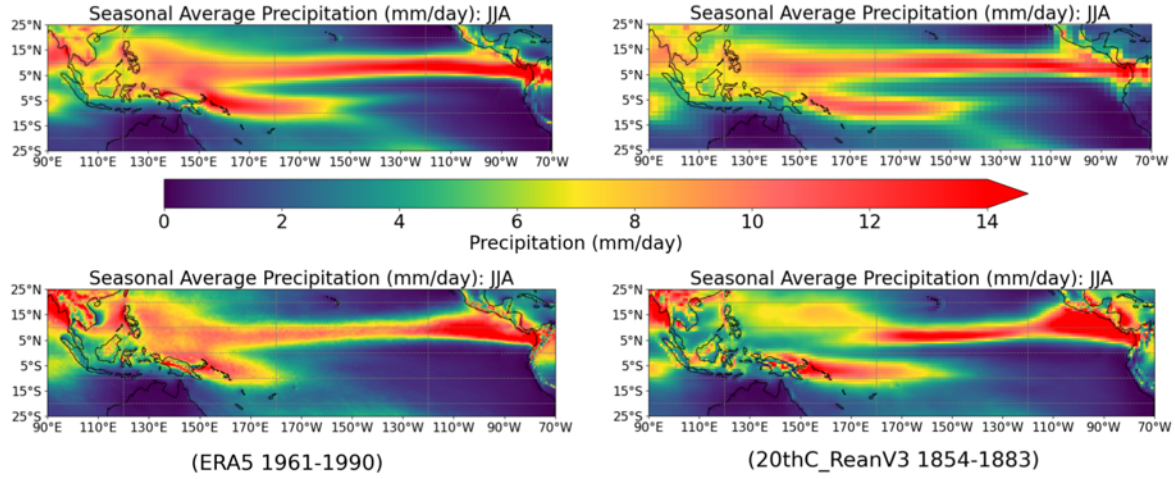

Figure 1: Simulated seasonal mean precipitation [in mm/day] for boreal summer (June-August, JJA) in pre-industrial control simulations of the iCESM1.2 at a horizontal resolution of 1° (upper left) and 2° (upper right) in the atmosphere. For model evaluation, simulated results are compared to reanalysis data of the European Center for Medium Range Weather Forecast (ERA5; bottom left) and the NOAA/CIRES/DOE 20th Century Reanalysis (V3) datasets (bottom right).

A first iCESM1.2 simulation for the mid-Holocene centered at 6 kiloyears before present (6 ka BP) has been done following the corresponding protocol of the Paleoclimate Modelling Intercomparison Project (PMIP) for reductions in greenhouse gas concentrations and seasonal and latitudinal changes in insolation (Otto-Bliesner et al., 2017). Based on a preliminary analysis, the multi-year annual-mean surface temperature response at 6 ka with respect to the pre-industrial reference state exhibits the largest anomalies over high northern and southern latitudes (Fig. 2) and a large-scale cooling over most continental regions of the northern hemisphere tropics and subtropics. When compared to PMIP results (Brierley et al., 2020), our high-resolution iCESM1.2 simulation is largely consistent with both the PMIP3-CMIP5 and PMIP4-CMIP6 multi-model ensemble mean response to the 6 ka forcing. In general, the

simulation bears strong ressemblance to the larger high-latitude anomalies found in the PMIP3-CMIP5 ensemble except for the mid-latitudinal North Atlantic cooling simulated by iCESM1.2.

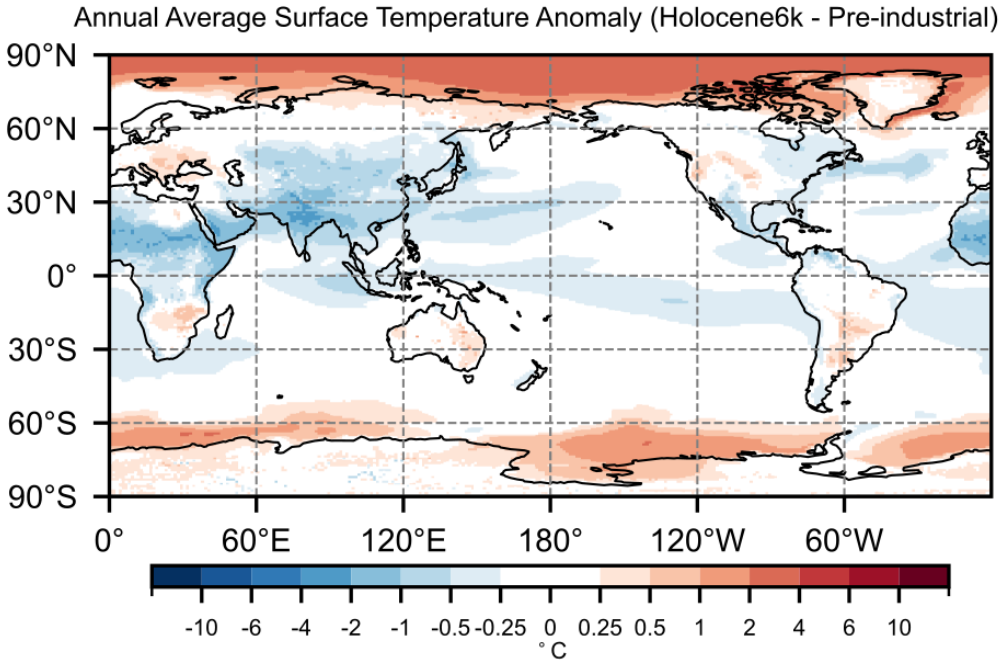

Figure 2: Annual mean changes of surface temperature [in °C] for the mid-Holocene with respect to pre-industrial conditions as simulated by the iCESM1.2 model (1° resolution). Results shown are based on multi-year annual averages.

Outlook

The expected outcome of the project is two-fold. On the one hand, characteristics of tropical mean climate and variability will be studied through appropriately designed sensitivity experiments with iCESM1.2. For this purpose, the set of model experiments envisaged for this project will be further extended and will be analyzed in more depth. On the other hand, the proxy-forward modelling by stable water-isotope enabling in iCESM1.2 has the potential of allowing a direct comparison to hydroclimate information provided by fossil coral records. In the framework of the DFG Priority Program SPP 2299, this will offer the opportunity for proxy-model intercomparison and collaboration with the coral experts within SPP 2299. Our simulations will help to interpret signals of variability recorded by tropical corals during warm periods in the past.

Presentations

1. T. Felis, M. Pfeiffer, **J. Hargreaves**, and SPP 2299 team members (incl. D. Li and U. Merkel), EGU General Assembly, Vienna, April 2023 (Poster)
2. **D. Li** and U. Merkel, *Tropical Atlantic-Pacific hydroclimate, variability and teleconnections during the Last Interglacial and the Holocene - Insights from earth-system modelling and corals,* Topical Meeting of the DFG Priority Programme SPP 2299, Bremen, June 2023 (Talk)
3. **T. Felis** and SPP2299 team members (incl. D. Li and U. Merkel), *Tropical Climate Variability and Coral Reefs - A Past to Future Perspective on Current Rates of Change at Ultra-High Resolution (SPP 2299),* GeoBerlin 2023 - Geosciences Beyond Boundaries - Research, Society, Future, Berlin, September 2023 (Talk)

4. **D. Li** and U. Merkel, *Tropical Atlantic-Pacific hydroclimate, variability and teleconnections during the Last Interglacial and the Holocene - Insights from earth-system modelling and corals,* Status Seminar of the DFG Priority Programme SPP 2299, Bremen, November 2023 (Talk)
5. **T. Felis** and SPP 2299 team members (incl. D. Li and U. Merkel), *Tropical Climate Variability and Coral Reefs - A Past to Future Perspective on Current Rates of Change at Ultra-High Resolution (SPP 2299)*, American Geophysical Union 2023 Fall Meeting, December 2023 (Talk)
6. **D. Li** and U. Merkel, *Tropical Atlantic-Pacific hydroclimate, variability and teleconnections during the Last Interglacial and the Holocene - Insights from earth-sytem modelling and corals,* Status Seminar of the DFG Priority Programme SPP 2299, Bremen, November 2023 (Talk)

(presenting person marked in bold)

References

1. T. Felis (2020), Extending the instrumental record of ocean-atmosphere variability into the last interglacial using tropical corals, *Oceanography,* **33** (2), doi:10.5670/oceanog.2020.209.
2. J. R. Brown et al. (2020), Comparison of past and future simulations of ENSO in CMIP5/PMIP3 and CMIP6/PMIP4 models, *Climate of the Past,* **16**, 1777-1805, doi:10.5194/cp-16-1777-2020.
3. C. M. Brierley et al. (2020), Large-scale features and evaluation of the PMIP4-CMIP6 midHolocene simulations, *Climate of the Past*, **16**, 1847–1872, doi:10.5194/cp-16-1847-2020.
4. B. L. Otto-Bliesner et al. (2017), The PMIP4 contribution to CMIP6 - Part 2: Two interglacials, scientific objective and experimental design for Holocene and Last Interglacial simulations, *Geoscientific Model Dev.*, 10, 3979-4003, doi:10.5194/gmd-10-3979-2017.

5.19 *hbk00097:* Improved Projections of the Antarctic Ice Sheet Contribution to Sea Level Rise until 2100 using Coupled Ice Sheet-Ice Shelf-Ocean Modelling

HLRN Project ID:	hbk00097
Run time:	I/2023 – IV/2024
Project Leader:	Prof. Dr. Torsten Kanzow
Project Scientists:	R. Timmermann, O. Richter, V. Teske, J. Barnes
Affiliation:	Alfred-Wegener-Institut für Polar- und Meeresforschung / University Bremen

Overview

In the context of the EU Horizon 2020 project PROTECT (PROjecTing sEa-level rise: from iCe sheets to local implicaTions), the aim of this project is to provide well-constrained projections of the Antarctic ice sheet contribution to sea level rise until 2100, under scenarios of high interest to stakeholders. To achieve this, we couple two state-of-the-art numerical models, a global ocean circulation model (FESOM) that resolves the complex geometry of ice-shelf cavities and an ice-flow model (Úa) simulating dynamics of the Antarctic Ice Sheet. For the first time, we run Antarctic-wide coupled ice-ocean simulations using unstructured grids in both components, which allows for a particularly high resolution near the grounding lines. Projections until 2100 will be produced using the high-impact scenario SSP585 and also a mitigation scenario.

Coupled projections are complemented with stand-alone ice-sheet simulations to inform on the uncertainty arising from the use of melt parameterisations in longer-range projections.

Results

We performed global ocean/pan-Antarctic Ice Sheet hindcast simulations for the historical period 1979-2018, using atmospheric forcing derived from the ERAinterim reanalysis. After inversion, the ice model is stepped forward in time for 20 years using constant ice shelf basal melt rates from the FESOM spin-up (mean of the last 5 years). During this relaxation period ice dynamics adjust to inconsistencies between inversion inputs and forcing. Ice shelf basal melt rates and cavity geometry are then updated at an annual interval to simulate the target period of 39 years.

We extended the coupled hindcast simulation by a future projection using an atmospheric warm anomaly derived for the time span 2090-2100 (relative to the average over mean 1990-2000) from results obtained for the SSP5-8.5 scenario from the AWI climate model (AWI-CM; Semmler et al., 2020). In a second step, we repeated these experiments using Úa in its standalone configuration with parameterized melt rates, as is common practice in state-of-the-art standalone ice sheet simulations. We employed the semi-local melt parameterisation proposed by Favier (2019) and Jourdain et al. (2022), which has been used in several of the standard ice sheet projections of the Ice Sheet Model Intercomparison Project for CMIP6 (ISMIP6). We calibrated the ice-shelf basal melt parameterisation to present-day climate using ocean conditions and melt rates from the FESOM spin-up for the coupled hindcast simulation (using the mean of the last five years). Given that the most rapidly changing glaciers are in the Amundsen Sea, we tuned the parameterization for this region. To exclude potential effects of basin-to-basin teleconnections, all other ice shelves in this simulation remained coupled to FESOM.

Figure 1 compares the mean depth distribution of parameterised melt rates with the source data used for the calibration. The distributions are very similar, confirming that the general design of the parameterization and our calibration are appropriate.

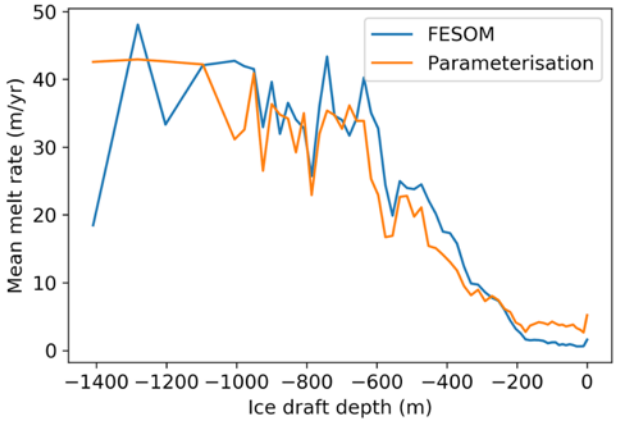

Figure 1: Evaluation of the semi-local melt rate parameterisation after calibration for present-day climate. Coloured lines indicate ice-shelf basal melt rates averaged over different depths in the Amundsen Seas as simulated by FESOM (5-year mean at the end of the spin-up for the hindcast) and by the parameterisation calibrated with FESOM results.

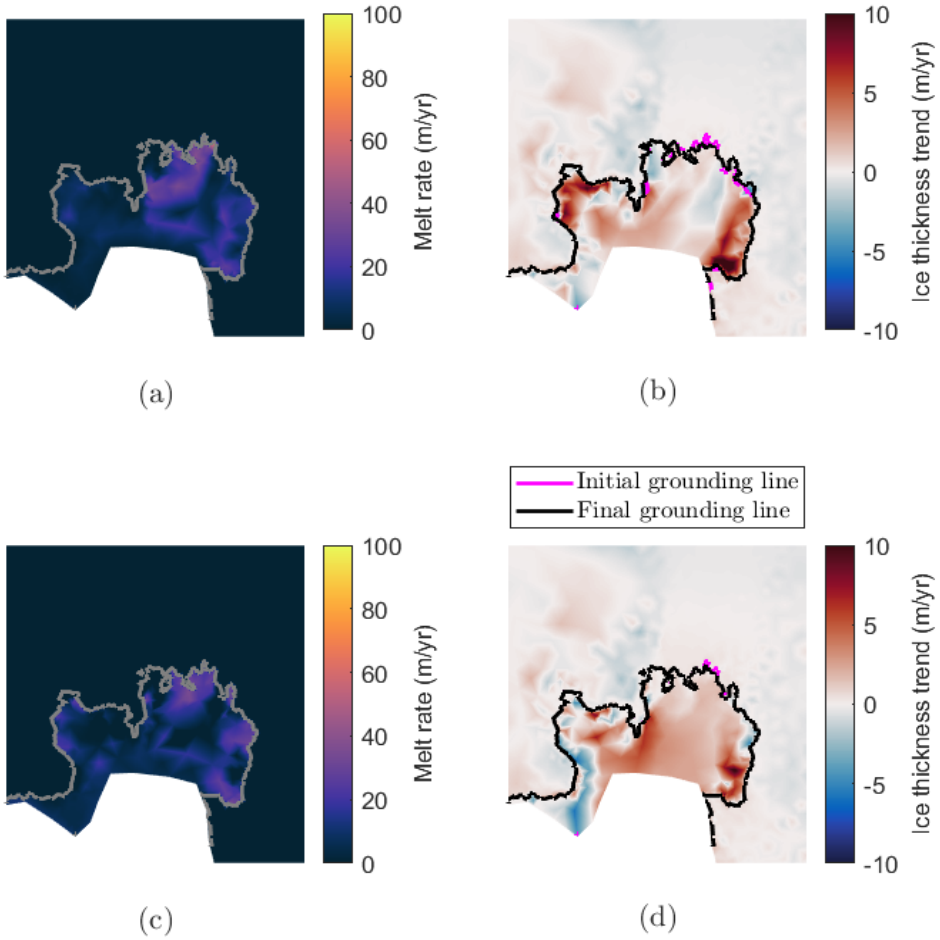

Figure 2: Effect of ice-ocean coupling for Pine Island Glacier in present-day climate. For the coupled simulation: (a) ice-shelf basal melt rates at the beginning of the coupled experiment, (b) mean ice thickness trend over the 39 years of integration. Panels (c) and (d) indicate the equivalent results from the Úa stand-alone simulation.

A comparison between coupled (FESOM-Úa) and standalone (Úa with parameterized melt rates) hindcast simulations indicates that for present-day climate, i.e. in the situation that the parameterization has been tuned for, coupled and standalone approaches agree very well (Figure 2). Basal melt rates are very similar in terms of magnitude and distribution; ice thickness trends are not identical but similar in magnitude and sign. Rates of grounding-line migration are small but to a large extent consistent between the two experiments.

For future climate, the discrepancy between the coupled ice sheet-ocean simulation and the Úa-only experiment with parameterized melt rates increases (Fig. 3). Melt rates in the coupled simulation are larger (Fig. 3a); ice thickness shows a clear negative trend (Fig. 3b) and the simulated grounding line retreats substantially. In contrast, the standalone experiment with parameterized melting yields basal melt rates very similar to the present-day situation (Fig. 3c); ice shelf thickness trends (Fig. 3d) are opposite in sign compared to the coupled model over large parts of the ice shelf.

An important quantity for the ice sheet's contribution to sea-level rise is its volume above floatation (VAF). Simulated VAF trends for the catchment basin of Pine Island Glacier are negative throughout the four experiments analysed here. For present-day climate the VAF trend in the FESOM-Úa coupled simulation is about 20% larger than for standalone Úa with parameterized melt rates. This discrepancy increases to 41 % for the future climate projection.

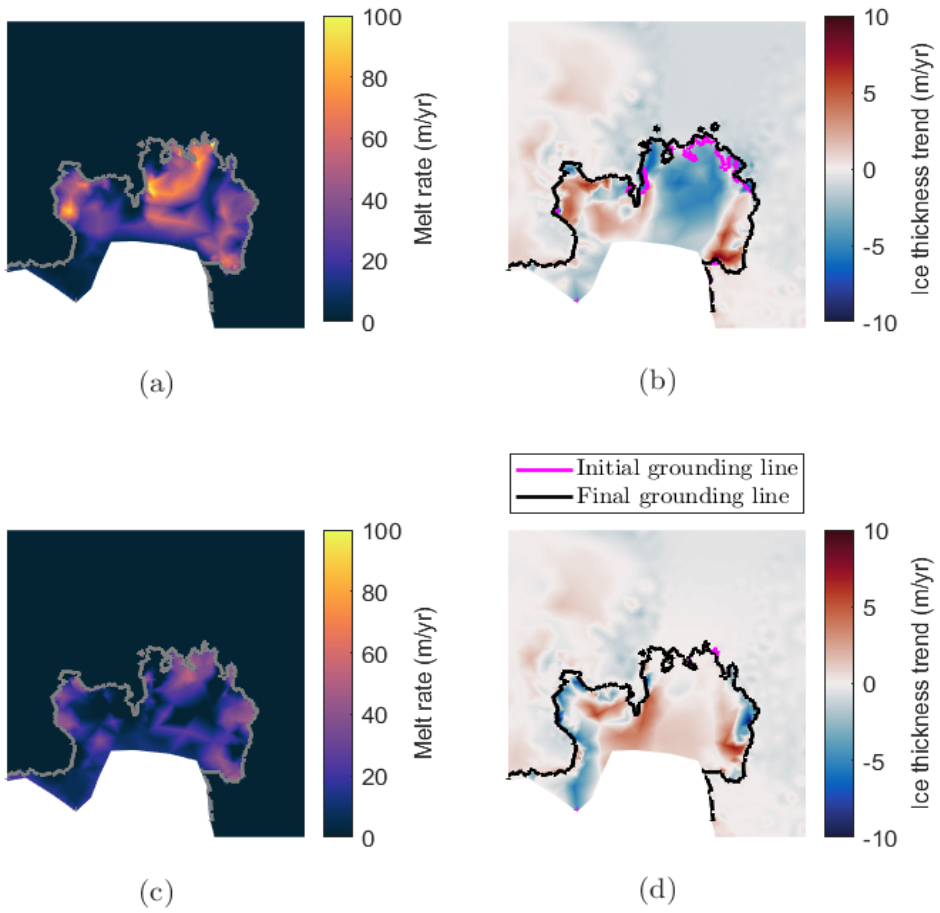

Figure 3: Effect of ice-ocean coupling for Pine Island Glacier in future climate. For the coupled simulation: (a) ice-shelf basal melt rates at the beginning of the coupled experiment, (b) mean ice thickness trend over the 39 years of integration. Panels (c) and (d) indicate the equivalent results from the Úa stand-alone simulation.

We conclude that even with a semi-local parameterization that has been well calibrated and has proven to give appropriate results for present-day climate, the projection of parameterized basal melt rates into a future (warmer) climate state is not reliable. Even though coupled ice sheet-ocean models impose a considerable challenge to available computing resources particularly due to the long time scales that are relevant to ice sheet processes, we find that they are essential to achieve robust forecasts of the future contribution of the Antarctic Ice Sheet to sea-level rise.

Outlook

As a next step, we plan to run the coupled model in transient scenario experiments for different climate scenarios until the end of the 21st century.

Publications

1. O. Richter, R. Timmermann, G.H. Gudmundsson, and J. De Rydt, *Coupling framework (1.0) for the Úa ice sheet model and the FESOM-1.4 z-coordinate ocean model in an Antarctic domain*, Geoscientific Model Development (in prep.)

Presentations

2. O. Richter, *The power of unstructured grids: Coupled Antarctic ice sheet-ocean modelling using Úa-Fesom v1.0*, FRISP workshop, Stalheim, Norway, 19-22 June 2023,

6.20 *hbk00098:* Climate Data Record of Stratospheric Aerosols

HLRN Project ID:	hbk00098
Run time:	I/2023 – I/2024
Project Leader:	Dr. A. Rozanov
Project Scientists:	Dr. C. Arosio, Dr. C. Pohl
Affiliation:	Institute of Environmental Physics, University of Bremen

Overview

Stratospheric aerosols play an important role in the Earth system and in the climate. Through the scattering of solar radiation back to space and by heating the stratosphere through the absorption of thermal infrared radiation upwelling from the troposphere, stratospheric aerosols impact the radiative forcing and thus the energy balance of the Earth's atmosphere. By providing a surface for heterogeneous reactions, which release halogens, stratospheric aerosols contribute to the catalytic depletion of ozone. One of the characteristics widely used to describe the amount of stratospheric aerosol is its extinction coefficient. At a first approximation, the aerosol extinction coefficient can be used to estimate the radiative forcing and thus quantify implications for ozone and climate change. While several data sets of the stratospheric aerosol extinction coefficient exist, there were only a few studies jointly analyzing aerosol records from multiple instruments. The most widely known aerosol climatology using merged aerosol data from different satellite instruments is GloSSAG. This climatology intentionally minimizes the number of instruments used while focusing on the data coverage. As a consequence, the data sets from the European instruments at Envisat (SCIAMACHY, GOMOS) and joint NASA/NOAA Suomi NPP OMPS mission are not included. In the framework of the ESA-CREST project (https://eo4society.esa.int/projects/crest/) a collaboration between the Finnish Meteorological Institute and the University of Bremen was established to create a merged long-term multi-mission aerosol record with the main objective to increase the reliability of the data set by including multiple instruments measuring similar atmospheric quantities in the post-2000 period. In the course of the project, biases in the underlying data sets from SCIAMACHY and OMPS-LP were identified and a development of improved algorithms initiated. Promising results were obtained for a limited number of test runs. This project aims at a processing of the entire measurement data form SCIAMACHY and OMPS-LP, creation of the improved data sets of the aerosol extinction coefficients and performing comparisons with independent data sets. The ultimate goal of this project is including the improved results in the final merged data set.

Results

A new algorithm to retrieve vertical profiles of the aerosol extinction coefficient from the limb-scatter measurements made by the NASA OMPS-LP instrument has been developed at the University of Bremen. The retrieval uses the limb radiances at 869 nm. The algorithm employs the normalization of the limb radiances to the solar irradiance in contrast to the normalization by a limb measurement at an upper tangent height, which is used by most of the other published limb-scatter retrievals. In addition, the effective surface albedo is retrieved simultaneously with the aerosol extinction coefficient. The new retrieval approach was applied to OMPS measurements from 2012 to 2023 to generate a long-term global data set of the stratospheric extinction coefficient. The new data product, referred to as V2.1, was evaluated by comparing with independent data from SAGE-III/ISS [1] and OSIRIS [2] instruments.

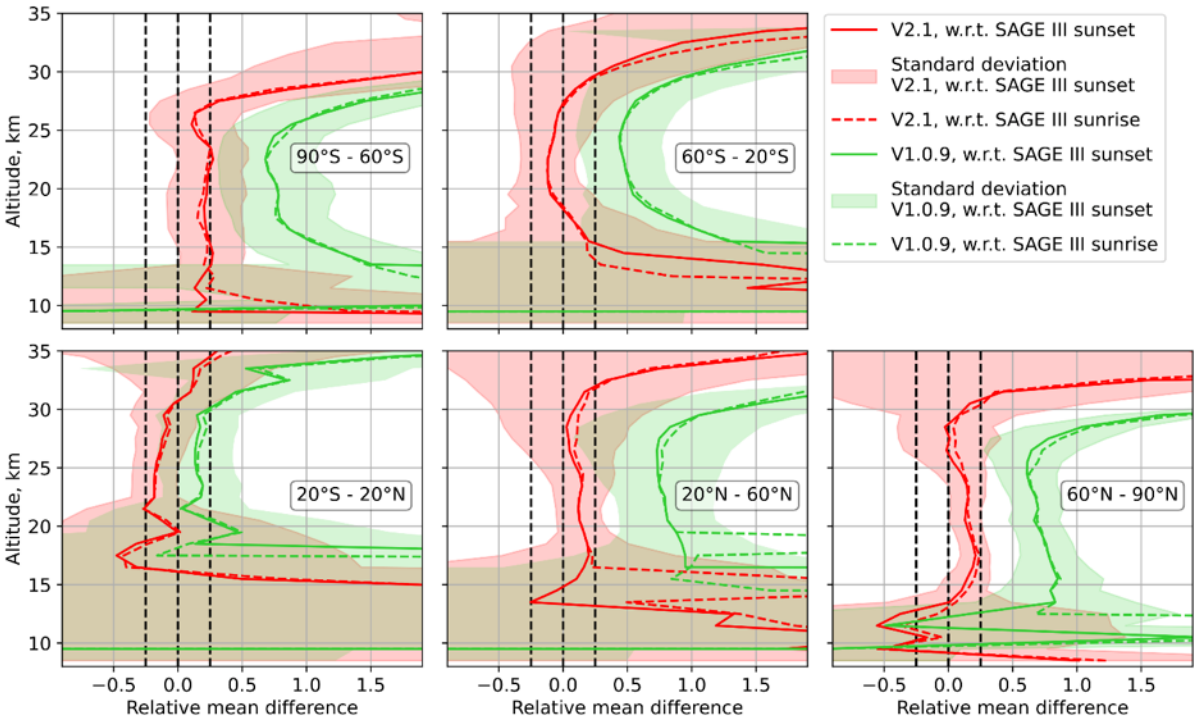

Figure 1. Comparison of V2.1 and V1.0.9 OMPS-LP retrieval results with collocated SAGE III/ISS data for 2018 for different latitude bands. The vertical black dashed lines mark zero and ±25% levels.

Here, we show only a comparison with SAGE III/ISS data for the year 2018 (selected arbitrary). Comparisons for the other years and for the OSIRIS instrument are presented in [3]. A comparison for the current V2.1 aerosol extinction product and for the precursor product V1.0.9 with collocated data from SAGE III/ISS is shown in Figure 1 for different latitude ranges. The relative difference shown in the plots was calculated as (OMPS-LP – SAGE_III)/SAGE_III. The comparisons were done independently for SAGE III/ISS sunset (solid lines) and sunrise (dashed lines) measurements. For reasons of clarity, the standard deviation of the differences is shown only for collocations with the SAGE III/ISS sunset measurements. The plot demonstrates that V2.1 retrieval generally shows lower values than those from V1.0.9 significantly reducing differences to the SAGE III/ISS results for most of the latitude bands. In the tropics, the agreement with SAGE III/ISS data is similar for both V2.1 and V1.0.9 results with differences changing from mostly positive for V1.0.9 to mostly negative for V2.1. Typically, V2.1 OMPS-LP retrieval agrees within 25% with SAGE III/ISS data between 18 and 30 km. Only in high southern latitudes the agreement starts degrading already above 27 km. In the lower stratosphere, a good agreement is seen down to about 13 km in the northern extra-tropics (about 16 km for sunrise collocations in the northern mid-latitudes), down to 15 km in the southern mid-latitudes and down to 8(12) km for sunset(sunrise) collocations in the southern high latitudes. A similar agreement is found for other years (see [3]) with exception of the southern middle and high latitudes, where larger (but still typically within 20%) negative differences with respect to SAGE III/ISS are observed. The larger differences for these years are explained by a stronger aerosol loading in caused by the Australian wildfires (2020) and Hunga Tonga - Hunga Ha'apai eruption (2022).

The V2.1 OMPS-LP aerosol extinction data set was used to analyze the evolution of the aerosol plume after the Hunga Tonga - Hunga Ha'apai eruption occurred in Jenuary 2022. The temporal evolution of 10 days zonal mean values as a function of the altitude for different latitude bands and as a function of the latitude at different altitudes are shown in Figure 2. It is seen that a strong aerosol plume is seen almost immediately after the eruption. The maximum of the aerosol plume reaches the altitude of about 26 km and a perturbation of the aerosol

level is seen up to 35 km altitude. The stratosphere is strongly perturbed in tropics and southern middle and high latitudes while only a small amount of aerosols penetrates into northern mid-latitudes. To the end of the analyzed record (December 2023), the stratosphere still did not relax to the pre-eruption state.

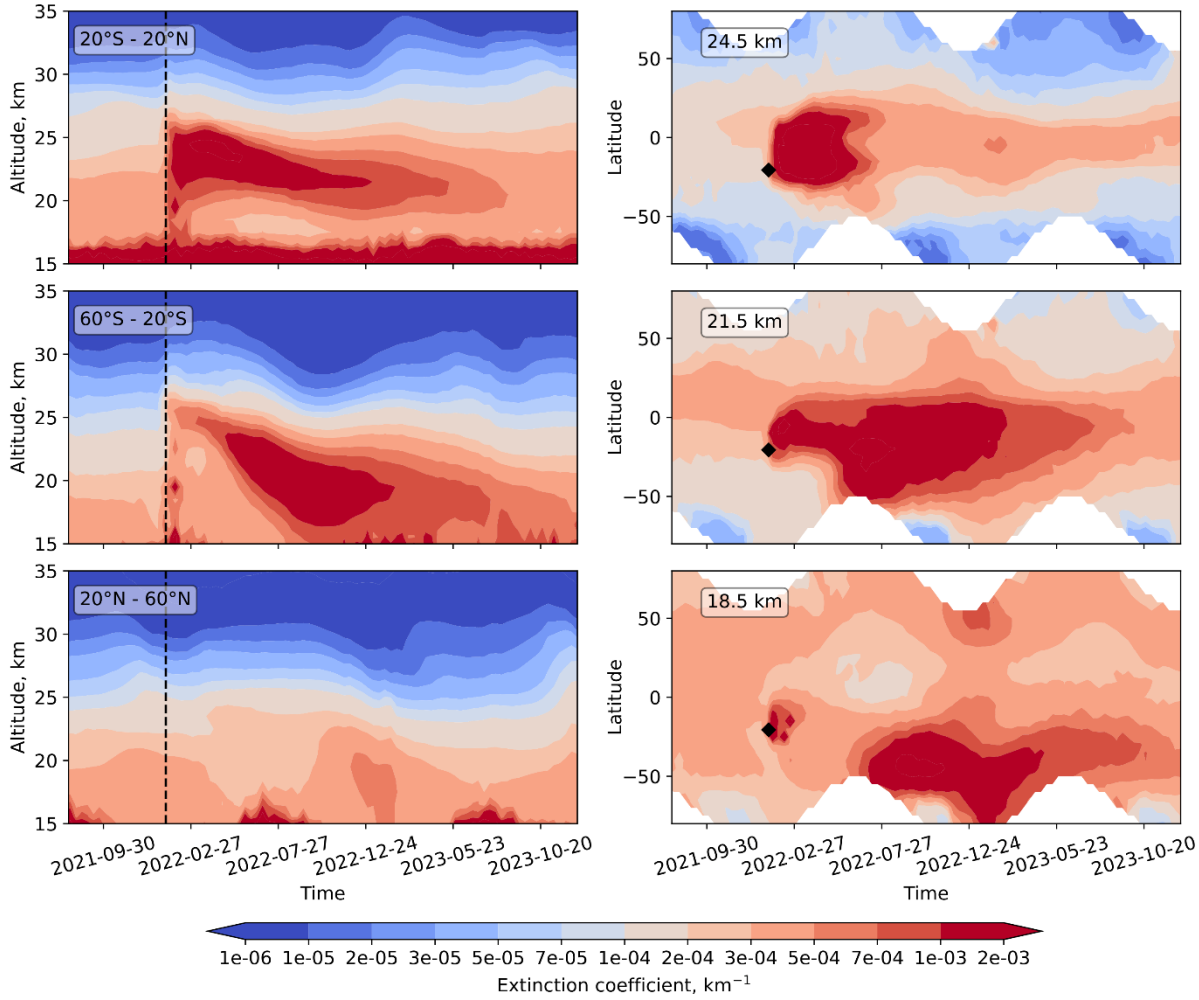

Figure 2. Evolution of the aerosol plume in different latitude bands and at different altitude levels. Left panels: 10 days zonal mean aerosol extinction coefficient at 869 nm in different latitude bands (from top to bottom): 20°S - 20°N, 60°S - 20°S, 20°N--60°N. The black dashed line mark the time of the strongest Hunga-Tonga eruption (January 15th, 2022). Right panels: 10 days zonal mean aerosol extinction coefficient at 869 nm at different altitude layers (from top to bottom): 24.5, 21.5, 18.5 km. The black rhombus marks the position of the Hunga Tonga - Hunga Ha'apai volcano and date of its strongest eruption.

A new retrieval approach (V3.0) was also developed for the retrieval of the vertical profiles of the aerosol extinction coefficient from SCIAMACHY [4] limb-scatter measurements. The retrieval uses the limb radiances at 750 nm. Similar to the OMPS-LP V2.1 data product, SCIAMACHY V3.0 retrieval also employs normalization to the solar irradiance spectrum. In addition, a surface albedo retrieved from the collocated nadir measurements is used in the retrieval as a fixed parameter. This could not be done for OMPS-LP instrument as the matching nadir instrument, OMPS-NM, does not cover the spectral range of the aerosol retrieval. In the framework of this project, the SCIAMACHY V3.0 data product was generated for the entire operational period of the SCIAMACHY instrument (2002 - 2012). The validation results for this data product show that the agreement with SAGE II data is typically similar to that found with the precursor version (V1.4) of the SCIAMACHY aerosol extinction data product. For southern

mid-latitudes the differences with respect to SAGE II data for V3.0 and V1.4 SCIAMACHY retrievals have the same magnitude but change the sign, see Figure 3. In addition, most of the outliers identified in the comparison of V1.4 extinction data with independent measurements are not seen in the comparisons for the V3.0 product anymore (see Figure 4).

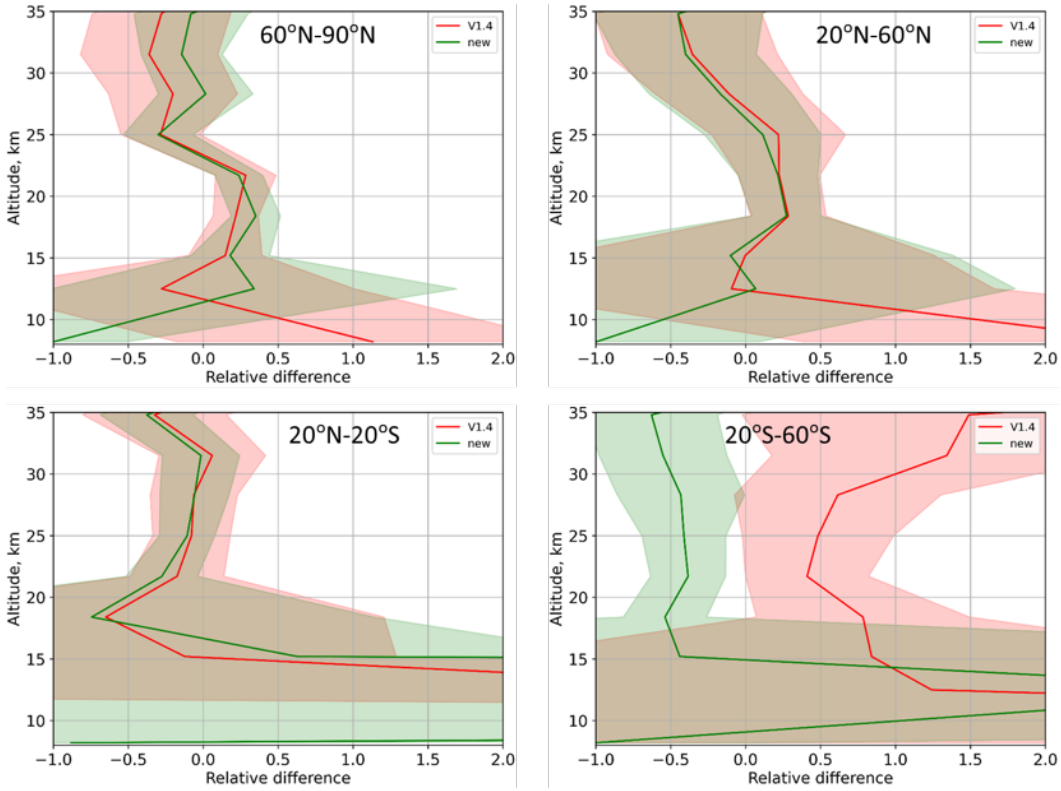

Figure 3: Comparison of V3.0 and V1.4 SCIAMACHY retrieval results with collocated SAGE II data for 2004 for different latitude bands. The relative difference was calculated as (SCIAMACHY – SAGE II)/SAGE II.

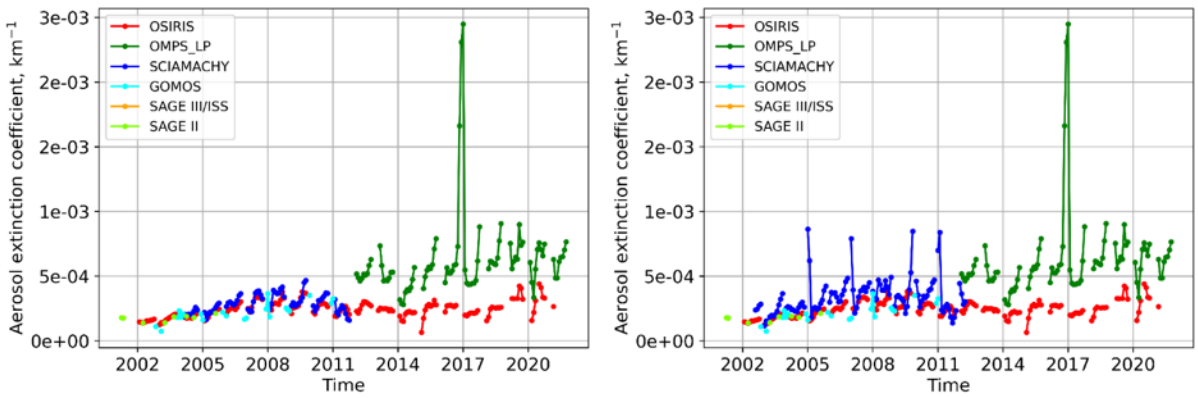

Figure 4: Aerosol extinction coefficient time series from different space borne instruments at an altitude of 18.4 km in a 10° latitude bin around 75N. Left panel: V3.0 SCIAMACHY retrievals (blue line). Right panel: V1.4 SCIAMACHY retrievals (blue line). Please note, all time series with exception of SCIAMACHY are the same in both panels. The green line shows an older version of OMPS-LP data.

Outlook

The project is intended to be continued to extend the OMPS-LP V2.1 extinction coefficient time series and investigate the potential to improve SCIAMACHY V3.0 retrieval in the southern mid-latitudes. Preliminary investigations show that an underestimation of the effective surface

reflectance is responsible for the low bias in V3.0 of the SCIAMACHY aerosol extinction coefficients. To improve the quality of the retrievals a better estimation of the effective surface reflectance needs to be obtained, potentially by including it in the fit procedure similar to the OMPS-LP algorithm.

Publications

1. A. Orfanoz-Cheuquelaf, C. Arosio, Rozanov, A., M. Weber, A. Ladstätter-Weisenmayer, J. P. Burrows, A. M. Thompson, R. M. Stauffer, and D. E. Kollonige, *Tropospheric ozone column dataset from OMPS-LP/OMPS-NM limb-nadir matching*, Atmospheric Measurement Techniques Discussions, 2023, 1 - 28, 2023.
2. A. Rozanov, C. Pohl, C. Arosio, A. Bourassa, K. Bramstedt, E. Malinina, L. Rieger, and J. P. Burrows: *Retrieval of stratospheric aerosol extinction coefficients from OMPS-LP measurements*, EGUsphere [preprint], https://doi.org/10.5194/egusphere-2024-358, 2024.
3. V. F. Sofieva, Rozanov, A., Szelag, J.P. M. Burrows, C. Retscher, R. Damadeo, D. Degenstein, L. A. Rieger, and Bourassa A., *A Climate Data Record of Stratospheric Aerosols*, Atmospheric Measurement Techniques Discussions, 2024, submitted.
4. V. F. Sofieva, M. Szelag, J. Tamminen, D. Fussen, C. Bingen, F. Vanhellemont, N. Mateshvili, A. Rozanov and C. Pohl, *Multi-wavelength dataset of aerosol extinction profiles retrieved from GOMOS stellar occultation measurements*, Atmospheric Measurement Techniques Discussions, pp. 1 - 18, 2023.
5. V. F. Sofieva, M. Szelag, J. Tamminen, C. Arosio, Rozanov, A., M. Weber, D. Degenstein, A. Bourassa, D. Zawada, M. Kiefer, A. Laeng, K. A. Walker, P. Sheese, D. Hubert, M. van Roozendael, C. Retscher, R. Damadeo, and J. D. Lumpe, *Updated merged SAGE-CCI-OMPS+ dataset for the evaluation of ozone trends in the stratosphere*, Atmospheric Measurement Techniques, 16, no. 7, 1881 - 1899, 2023.

Presentations

1. Rozanov, A., Pohl, C., Arosio, C., Bourassa, A., Bramstedt, K., Damadeo, R., Rieger, L., Burrows, J.P.: *Retrieval of stratospheric aerosol extinction coefficients from OMPS-LP measurements*, 12th Atmospheric Limb Workshop, Brussels, 22-26 May 2023, 2023.
2. Sofieva, V. F., Szelag, M., Tamminen, J., Fussen, D., Bingen, C., Vanhellemont, F., Rozanov, A..: *Multi-wavelength dataset of aerosol extinction profiles retrieved from GOMOS stellar occultation measurements*, 12th Atmospheric Limb Workshop, Brussels, 22-26 May 2023, 2023.
3. Sofieva, V. F., Rozanov, A., Szelag, M., Retscher, C., *Climate data record of stratospheric aerosols*, 12th Atmospheric Limb Workshop, Brussels, 22-26 May 2023, 2023.
4. von Savigny, C. and the VolImpact Team, *Overview of the joint research project VolImpact, invited keynote talk*, PAGES Volcanic Impacts on Climate and Society Workshop, Bern, Switzerland, May 24, 2023.

PhD Thesis

1. A. Orfanoz-Cheuquelaf, *Retrieval of total and tropospheric ozone columns from OMPS-NPP*, PhD thesis, University of Bremen, 2023.

References

1. W. P. Chu, M. Patrick McCormick, Joseph M. Zawodny, and Lemuel E. Mauldin III, *Stratospheric aerosol and gas experiment II*I, in: Earth Observing Systems II, William L. Barnes, (Ed.), vol. 3117, pp. 11 - 18, SPIE. International Society for Optics and Photonics, 1997.

2. E. J. Llewellyn, N. D. Lloyd, D. A. Degenstein, R. L. Gattinger, S. V. Petelina, A. E. Bourassa, J. T. Wiensz, E. V. Ivanov, I. C. McDade, B. H. Solheim, J. C. McConnell, C. S. Haley, C. von Savigny, C. E. Sioris, C. A. McLinden, E. Griffioen, J. Kaminski, W. F. J. Evans, E. Puckrin, K. Strong, V. Wehrle, R. H. Hum, D. J. W. Kendall, J. Matsushita, D. P. Murtagh, S. Brohede, J. Stegman, G. Witt, G. Barnes, W. F. Payne, L. Piché, K. Smith, G. Warshaw, D. L. Deslauniers, P. Marchand, E. H. Richardson, R. A. King, I. Wevers, W. McCreath, E. Kyrölä, L. Oikarinen, G. W. Leppelmeier, H. Auvinen, G. Mégie, A. Hauchecorne, F. Lefévre, J. de La Nöe, P. Ricaud, U. Frisk, F. Sjoberg, F. von Schéele, and L. Nordh, *The OSIRIS instrument on the Odin spacecraft*, Canadian Journal of Physics, 82, no. 6, 411 - 422, 2004.
3. A. Rozanov, C. Pohl, C. Arosio, A. Bourassa, K. Bramstedt, E. Malinina, L. Rieger, and J. P. Burrows: *Retrieval of stratospheric aerosol extinction coefficients from OMPS-LP measurements*, EGUsphere [preprint], https://doi.org/10.5194/egusphere-2024-358, 2024.
4. H. Bovensmann, J. Burrows, M. Buchwitz, J. Frerick, S. Noel, V. Rozanov, K. Chance, and A. Goede, *SCIAMACHY: Mission objectives and measurement modes*, J. Atmos. Sci., 56, 127 - 150, 1999.

6.21 *hbk00099:* Ocean - ice shelf interaction at the 79 North Glacier: Sensitivity to bathymetry and environmental conditions

HLRN Project ID:	hbk00099
Run time:	II/2023 – I/2024
Project Leader:	Prof. Torsten Kanzow[1,2]
Project Scientists:	Dr. Claudia Wekerle[2], Dr. Qiang Wang[2], Dr. Ralph Timmermann[2]
Affiliation:	[1]University Bremen and [2]Alfred Wegener Institute Helmholtz Center for Polar and Marine Research

Overview

Mass loss from the Greenland ice sheet has been one of the largest contributors to global sea-level rise over the past decades. However, processes that lead to this mass loss are not yet fully understood. In this project, we focus on the floating ice tongue of the 79 North Glacier (79NG) located in Northeast Greenland. It features the largest of the three remaining floating ice tongues of Greenland, stretching over 80 km in length in a 20 km wide fjord. The 79NG and its neighbouring glacier, the Zachariæ Isstrøm (ZI), drain the Northeast Greenland Ice Stream which covers 12% of the Greenland Ice Sheet area. Its complete melt would lead to a 1.1-m global sea level rise. In contrast to the ZI, which lost its floating ice tongue in the 2010s, the extent of the 79NG has not changed significantly. However, the ice tongue has been thinning in the past two decades.

In the past project phase, we developed a setup of the Finite-volumE Sea ice-Ocean Model (FESOM2.1) which resolves the cavity of the 79NG with a horizontal resolution of 700 m. Apart from a reference simulation covering the years 1960-2021, we carried out a suite of sensitivity experiments to investigate the role of subglacial discharge, ocean temperature, basal drag coefficient and winds on basal melt rates. Our simulations revealed an upward trend and interannual variability of the basal melt over the past 50 years, driven mainly by ocean warming in the Atlantic Intermediate Water (AIW) layer. Furthermore, we investigated the drivers of AIW temperature variability on the NEG continental shelf. These results were described in two papers published in JGR Oceans and Nature Communications. We are very grateful for the computing time granted by HLRN, which allowed us to conduct the computationally expensive simulations our work is based on.

Results

Circulation and melt below the 79NG ice tongue (Wekerle et al. 2024)

In this study we present a FESOM2.1 simulation that resolves the cavity of 79NG with 700 m mesh resolution, spanning the years 1960-2021. This model setup seamlessly connects the global and regional ocean circulation to the circulation in the cavity.

The ocean circulation in the cavity of the 79NG has so far been unknown, except that the inflow and outflow have been observed. As the cavity is covered by an ice tongue of several 100 m thickness, it is thus observationally very hard to access. A goal of our study was therefore to reveal the ocean circulation in the cavity. Our FESOM2.1 simulation shows that warm and salty Atlantic Intermediate Water (AIW, defined as waters with T>1°C) enters the cavity through its deepest channel as a bottom-intensified gravity current (Fig. 1a). The current accelerates down the slope of a sill located at the main entrance, reaching flow speeds greater than 0.3

ms^{-1}. The warm AIW then circulates cyclonically around the cavity. In particular, the jet turns north, loops into the entrance of Dymphna Sound and continues along the northern slope of the cavity. On its way towards the grounding line, the jet decelerates and becomes broader. The flow is thus clearly affected by rotation, deviating strongly from a two-dimensional estuarine circulation. The inflow of AIW results in ocean temperatures above the freshwater freezing point in the cavity throughout the year, which leads to strong and persistent melting at the base of the ice tongue. The simulated long-term mean basal melt rate is highest with a maximum value of 85 m yr^{-1} close to the grounding line (Fig.1b), where the ice tongue is thickest.

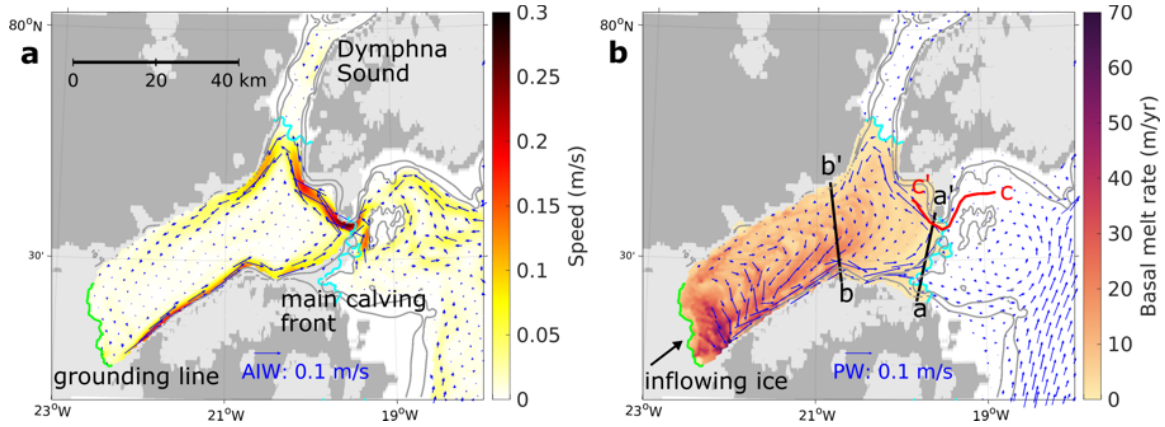

Figure 1: Cavity circulation and basal melt rate. a) Simulated velocity (blue arrows and colours) in the AIW layer (defined by T>1°C), and b) melt rate at the base of the floating ice tongue (colours) and velocity in the upper water column (T<1°C, blue arrows). Lines indicate the grounding line (green), calving front (cyan) and 100 m/200 m isobaths (grey). The grey and light grey background shows bare land and grounded ice, respectively. The model results were averaged over the time period 1970-2021.

Basal melt of the ice tongue is driven both by the ocean via transport of warm AIW into the glacier's cavity and by the atmosphere via subglacial discharge. Both drivers of basal melt have increased in recent decades and available observations are insufficient to judge which of the two drivers dominate. In this study, we disentangled the impact of both processes in a dynamically consistent way. We found that the simulated annual mean basal melt of the 79NG is significantly correlated with the AIW temperature at the calving front for the time period 1970-2021 (r=0.85, Fig. 2). In contrast, we did not obtain a significant correlation between basal melt and subglacial discharge (r=0.22). Thus, the ocean via inflow of AIW is the main driver of basal melt.

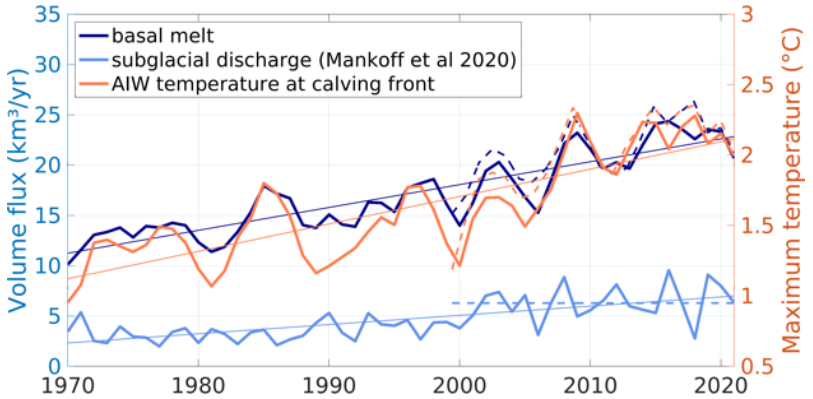

Figure 2: Annual mean basal melt rate (dark blue) and maximum AIW temperature in the water column at the calving front of the glacier (orange) simulated by FESOM2.1. Annual mean subglacial discharge entering the cavity at the grounding line of the glacier (light blue). Note that basal melt and subglacial discharge share the same y-axis. Thin coloured lines show the respective linear trends of the time series for the time period 1970-2021. Solid and dashed lines correspond to the reference experiment (REF) and a sensitivity experiment with climatological subglacial discharge (CLIM), respectively.

Interannual variability of Atlantic Intermediate Water (McPherson et al. 2023)

Increased oceanic heat transport plays a key role in the accelerated mass loss of Greenland's marine-terminating glaciers. The melt rate of major glaciers in Northeast Greenland (NEG) is controlled by ocean variability, in particular warm Atlantic Intermediate Water (AIW), on the continental shelf. In this study we investigated the drivers of AIW temperature variability on the NEG continental shelf by using a high-resolution configuration of the ocean sea-ice model FESOM2.1. The simulation was carried out for the years 1960--2021, forced by atmospheric data from JRA-55. The mesh resolution on the NEG continental shelf was set to 2-3 km in order to resolve the complex bathymetry there.

We characterized the seasonal to decadal variability of AIW, which features both pronounced interannual fluctuations and a long-term warming trend. A major source of AIW is the Atlantic Water (AW) originating from the West Spitsbergen Current that recirculates in Fram Strait. AW anomalies are advected westwards and partly control the AIW temperatures on the continental shelf. We showed that increased AIW temperatures are connected to pronounced northern and central branches of recirculating AW in Fram Strait. The strengthening of these pathways brings more warmer AIW onto the northern part of the NEG continental shelf. There, it circulates anti-cyclonically and results in shelf-wide warming. We connected the changes in the AW circulation to the regional atmospheric forcing. A composite analysis revealed that the strengthening of the northern AW branches is likely caused by anticyclonic wind anomalies over the Barents Sea that drive an enhanced northward AW transport in Fram Strait.

Outlook

In the next project phase, we plan to investigate the future evolution of the 79NG. We propose to conduct simulations driven by atmospheric forcing derived from the CMIP6 simulation result of the coupled climate model AWI-CM, comprising the historical period (1958-2014) and the SSP585 future scenario (2015-2100). We further plan to couple the ocean sea ice model FESOM2.1 to the ice sheet model ISSM. This will allow us to account for a changing geometry of the ice tongue.

Publications

1. R. McPherson, C. Wekerle and T. Kanzow, Shifts of the Recirculation Pathways in central Fram Strait drive Atlantic Intermediate Water Variability on Northeast Greenland shelf. *Journal of Geophysical Research: Oceans* (2023).
2. C. Wekerle, R. McPherson, W.-J. von Appen, Q. Wang, R. Timmermann, P. Scholz, S. Danilov, Q. Shu and T. Kanzow, Atlantic Water warming increases melt below Northeast Greenland's last floating ice tongue. *Nature Communications* (2024).

Presentations

1. C. Wekerle, Ocean heat flux drives basal melt of the 79°North Glacier*, VEPOSSSS online seminar*, April 5, 2023.
2. C. Wekerle, Atmosphere or ocean - What drives basal melt at Greenland's largest floating ice tongue, the 79°North Glacier? *FRISP meeting*, Norway, June 22, 2023.
3. C. Wekerle, High-resolution simulations of the ocean circulation beneath the 79° North Glacier, *Sea level conference*, Hamburg, June 6, 2023.

6.22 *hbp00058:* Exploring the mechanistic process of vitamin B_{12} acquisition by human gut bacteria

HLRN Project ID:	hbp00058
Run time:	III/2022 – II/2023
Project Leader:	Professor Dr. Ulrich Kleinekathöfer
Project Scientists:	Kalyanashis Jana
Affiliation:	School of Science, Constructor University

Overview

Vitamin B_{12}, also known as cobalamin, represents one of the most intricate organometallic cofactors and vitamins. It stands as a crucial nutrient for numerous Gram-negative bacteria, including *E. coli*, *B. thetaiotaomicron*, and others. In *E. coli*, the uptake of vitamin B12 involves the outer membrane (OM) protein BtuB. On the other hand, the B_{12} acquisition process in the Gram-negative bacterium B. *thetaiotaomicron* is notably intricate, relying on multiple vitamin B_{12} binding proteins such as BtuB, BtuG, and BtuH. The outer membrane protein BtuB collaborates with the surface-exposed lipoprotein BtuG in transporting vitamin B_{12}, competing with the intrinsic factor (IF) that serves a similar role in transporting B_{12} within the human body.[1,2] Recent studies have revealed that the lipoprotein BtuG exhibits a remarkable ability to bind vitamin B_{12} with femtomolar affinity. This high binding affinity enables BtuG to effectively facilitate the intake of vitamin B_{12} and compete with the intrinsic factor (IF) for binding to the outer membrane (OM) protein BtuB. In light of these findings, we conducted computational studies utilizing the newly crystallized BtuBG crystal structure and the cyanocobalamin bound BtuG protein of *B. thetaiotaomicron*.

The primary objective of these computational studies was to investigate the mechanism of cyanocobalamin (CNCbl) acquisition by BtuG within the BtuBG protein complex. Additionally, the focus extended to understanding the process of CNCbl transport from the active site of BtuG to the active site of BtuB. By utilizing computational modeling techniques, it was aimed to unravel the intricate molecular interactions governing the uptake and transport of vitamin B_{12} across bacterial membranes. Specifically, the computational investigation delved into elucidating the structural dynamics of the BtuBG protein complex and the molecular mechanisms underlying CNCbl recognition and binding by BtuG. Furthermore, the study sought to delineate the conformational changes necessary for CNCbl transfer from BtuG to BtuB, shedding light on the intricate interplay between these key proteins in facilitating the uptake and transport of vitamin B_{12}.Overall, the utilization of computational approaches alongside structural data has provided valuable insights into the molecular details of vitamin B_{12} acquisition and transport processes mediated by the BtuBG protein complex in *B. thetaiotaomicron*. These findings contribute to a deeper understanding of bacterial nutrient acquisition strategies and hold implications for the development of novel therapeutic interventions targeting bacterial metabolism and pathogenesis.[3]

Cyanocobalamin (CNCbl) and Hydroxocobalamin (HOCbl) are frequently employed for supplementation, along with methylcobalamin (MeCbl) and adenosylcobalamin (AdoCbl), to address vitamin B_{12} deficiency in the human body.[4] The binding constants obtained experimentally for cyanocobalamin (CNCbl) or hydroxocobalamin (HOCbl), both featuring small axial ligands (CN or OH), with transporters are found to be comparable to that of adenosylcobalamin (AdoCbl), which contains a relatively large axial group of adenosyl. Existing literature reports predominantly highlight the binding and translocation of CNCbl

through proteins in the outer membrane of Gram-negative bacteria. In this context, our computational exploration was conducted to extensively examine the binding affinity of all forms of cyanocobalamin (Me, Ado, HO, or CN) toward the surface-exposed BtuG protein. Furthermore, the study delved into the intricate processes of lid closing by BtuG and the subsequent translocation of cyanocobalamin through the BtuBG molecule. This investigation marks the first comprehensive examination of these molecular interactions, shedding light on the specificities of cyanocobalamin binding to the BtuG protein and its subsequent translocation through the BtuBG complex.

Moreover, *Bacteroidetes* in the human gut rely on a variety of proteins for the acquisition of vitamin B_{12}, with BtuH being one of the key proteins instrumental in facilitating the uptake of vitamin B_{12} in gut *Bacteroidetes*.[5] "This opens up an exciting avenue to investigate the structural dynamics of the recently resolved CNCbl-bound BtuH protein through unbiased MD simulations. Additionally, we aim to determine the binding free energy of CNCbl towards BtuH using well-tempered metadynamics (WTMtD) simulations. Furthermore, our plan involves exploring how the BtuH protein captures CNCbl from an arbitrary position by initially placing the CNCbl approximately 10-15 Å away from the binding site. To achieve this, we will leverage the BtuBGH cryo-EM structure for unbiased MD simulations, focusing on unraveling the structural dynamics of the BtuBGH complex. The comprehensive system encompasses the outer-membrane protein BtuB, along with the surface-exposed lipoproteins BtuG and BtuH. In our pursuit of these objectives, a combination of unbiased molecular dynamics (MD) simulations, enhanced sampling techniques, applied field simulations, and umbrella sampling will be employed to provide a thorough exploration of the intricate processes mentioned above.[6]

We would like to note that a fraction of the allocated compute time was dedicated to a study on the assembly of transmembrane pores from mirror-image peptides, an article recently published.[7]

Results

The MD simulation studies have unveiled a remarkable ability of the BtuG molecule to effectively draw vitamin CNCbl from nearby positions to its active site, facilitated by robust electrostatic and noncovalent interactions (Figure 1). An analysis of the electrostatic potential map showcased the BtuG's negatively charged binding pocket, demonstrating a clear capacity to attract the highly dipolar CNCbl molecule. Employing multiple-walker well-tempered metadynamics (WTMtD), binding free energies were calculated, aligning well with the experimental dissociation constant of approximately 10^{-14} M. Furthermore, investigations into the BtuG lid opening process, utilizing both biased and unbiased MD simulations, unveiled that BtuG undergoes a movement away from BtuB via a hinge loop, exhibiting an opening of up to 40°. To facilitate the acquisition of CNCbl from the surrounding environment, unbiased simulations were initiated with a starting structure featuring a 40° open conformation, with CNCbl positioned outside the BtuG protein. The BtuG lid demonstrated a rapid closure, reaching an angle of approximately 20°, allowing the CNCbl molecule to access the BtuG active site cavity within 1µs. Lastly, the study delved into the conformational dynamics of the CNCbl-bound BtuBG complex, elucidating the translocation process of CNCbl from the active site cavity of BtuG to BtuB. In the close state of the CNCbl-bound BtuBG, BtuG exhibited a weaker binding affinity to CNCbl compared to the CNCbl-BtuG interaction. This observation was attributed to several loop rearrangements, enabling CNCbl molecules to move toward the BtuB cavity more effectively. Furthermore, vitamin B_{12} bound BtuB3G3 cryoEM structure (obtained from loci 3 of *B. thetaiotaomicron*) was considered for unbiased simulation to explore the CNCbl translocation process. It was observed that the EL8 loop BtuB3 OM protein facilitates the translocation process via a repulsive force (Figure 1).

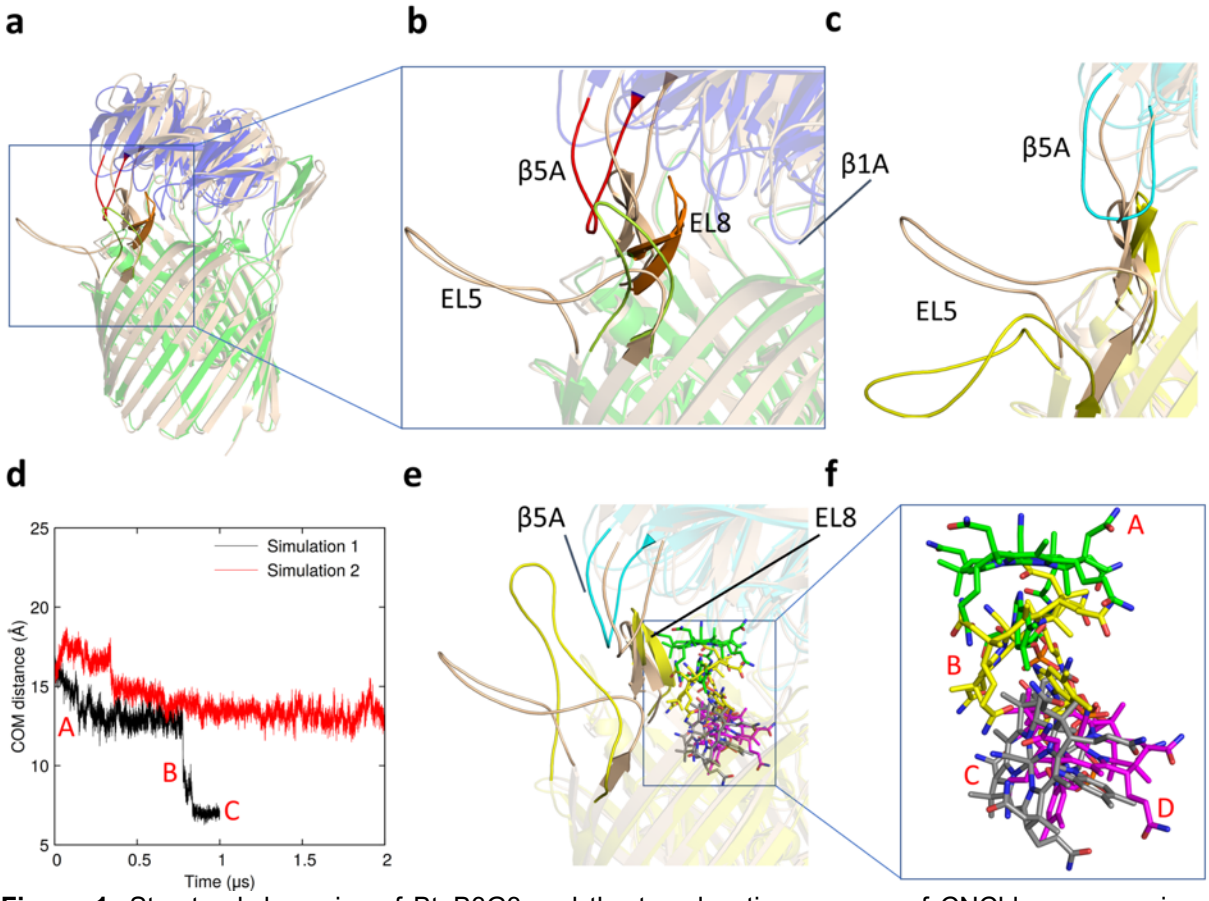

Figure 1: Structural dynamics of BtuB3G3 and the translocation process of CNCbl. **a.** comparison between the BtuB2G2 crystal structure (BtuB2 in green and BtuG2 in blue) and the BtuB3G3 cryoEM structure (shown in wheat), with vitamin B_{12} omitted for clarity. **b**. Close-up depicting differences in the conformations of the EL8 loops of BtuB and the β5A loops of BtuG (BtuB2 EL8 in orange; BtuG2 β5A in red; BtuG2 EL5 in green). **c**. Loop rearrangements in BtuB3G3 observed before (wheat) and after (lime for BtuB3; cyan for BtuG3) an unbiased MD simulation in the absence of vitamin B_{12}. **d.** Unbiased MD simulations based on the CNCbl-bound BtuB3G3 structure. Translocation of the CNCbl molecule was observed in simulation 1. Shown is the center of mass (COM) distance between CNCbl and the BtuB3 binding site. **e-f.** Overview of the CNCbl translocation process during simulation 1. The initial structure of BtuB3G3 is depicted in wheat, while the final structure is shown in lime for BtuB3 and cyan for BtuG3. Notably, there is an inward displacement of EL8 in BtuB3 and an outward displacement of β5A in BtuG3 at the simulation's conclusion. CNCbl is colored green in the BtuG3 binding site (A) and magenta in the BtuB3 binding site (D). An intermediate conformation from MD simulation 1 is depicted in yellow (B), and the final conformation is illustrated in grey (C).

MeCbl and AdoCbl bound BtuBG simulations

Initial exploration of MeCbl and AdoCbl affinity toward BtuG was conducted through multiple-walker well-tempered metadynamics (WTMtD) simulations. The subsequent ligand unbinding from the BtuG active site, as revealed by WTMtD simulations, demonstrated that the binding affinities of Me-Cbl and AdoCbl closely resemble that of CN-Cbl. Further simulations involved MeCbl-bound BtuBG protein in a POPE bilayer membrane, investigating the translocation of Me-Cbl through the BtuBG channel. The associated free energy for this translocation process exhibited similarities to that observed for CNCbl. WTMtD simulations illustrated that MeCbl undergoes a tilted movement toward the BtuB cavity and reorients within the BtuBG channel during this energetically favorable translocation process.

Extensive exploration of the AdoCbl translocation process was conducted through multiple-walker well-tempered metadynamics (WTMtD) simulations. Both unbiased and WTMtD

simulations of AdoCbl-bound BtuBG indicated a challenging translocation process due to its large size, despite having a binding affinity similar to that of CNCbl for the BtuG protein. To gain a detailed molecular-level understanding, a mutation study was undertaken, emphasizing the significance of acidic amino acid residues in CNCbl binding. Subsequent investigations involved exploring the binding affinity of AdoCbl and MeCbl with the E55A and Q336A mutated-BtuG, providing further insights into the intricacies of the binding interactions.

Outlook

The recently resolved crystal structure of the CNCbl binding protein, BtuH, opens up avenues for exploring its binding affinity to CNCbl, as well as the stability and role of the BtuGH and BtuBGH complexes in the CNCbl transport process. Previous findings have indicated the significant influence of Ca^{2+} and Na^{+} ions in the CNCbl binding cavity of BtuH, with a distinct orientation of CNCbl compared to its orientation in the BtuG protein.

In this context, we aim to investigate the stability of CNCbl-bound BtuH in the presence of various ion configurations, including two Ca^{2+}, two Na^{+}, only one Ca^{2+}, only one Na^{+}, and without any ion, using unbiased molecular dynamics (MD) simulations. The binding affinity of CNCbl with BtuH will be quantified and compared with CNCbl-BtuG interactions, along with the experimentally determined dissociation constant. Experimental evidence suggests a lower binding affinity with BtuH compared to BtuG. This disparity in binding affinities raises the intriguing possibility of CNCbl transport from the BtuH binding site to the BtuG binding site. Calculating the free energy associated with the CNCbl transport process will provide valuable insights into this dynamic molecular mechanism.

References

1 S. J. Hickman, R. E. M. Cooper, L. Bellucci, E. Paci and D. J. Brockwell, Gating of TonB-dependent transporters by substrate-specific forced remodelling, *Nat. Commun.*, 2017, **8**, 14804.

2 A. G. Wexler, W. B. Schofield, P. H. Degnan, E. Folta-Stogniew, N. A. Barry and A. L. Goodman, Human gut Bacteroides capture vitamin B 12 via cell surface-exposed lipoproteins, *Elife*, 2018, **18**, 7.

3 J. Abellon-Ruiz, K. Jana, A. Silale, A. M. Frey, A. Baslé, M. Trost, U. Kleinekathöfer and B. van den Berg, BtuB TonB-dependent transporters and BtuG surface lipoproteins form stable complexes for vitamin B12 uptake in gut Bacteroides, *Nat. Commun.*, 2023, **14**, 4714.

4 R. Obeid, S. N. Fedosov and E. Nexo, Cobalamin coenzyme forms are not likely to be superior to cyano- and hydroxyl-cobalamin in prevention or treatment of cobalamin deficiency, *Mol. Nutr. Food Res.*, 2015, **59**, 1364–1372.

5 E. E. Putnam, J. Abellon-Ruiz, B. J. Killinger, J. J. Rosnow, A. G. Wexler, E. Folta-Stogniew, A. T. Wright, B. van den Berg and A. L. Goodman, Gut Commensal Bacteroidetes Encode a Novel Class of Vitamin B 12 -Binding Proteins, *MBio*, , DOI:10.1128/mbio.02845-21.

6 J. D. Prajapati, U. Kleinekathöfer and M. Winterhalter, How to Enter a Bacterium: Bacterial Porins and the Permeation of Antibiotics, *Chem. Rev.*, 2021, **121**, 5158–5192.

7 S. Krishnan R, K. Jana, A. H. Shaji, K. S. Nair, A. D. Das, D. Vikraman, H. Bajaj, U. Kleinekathöfer and K. R. Mahendran, Assembly of transmembrane pores from mirror-image peptides, *Nat. Commun.*, 2022, **13**, 5377.

6.23 *hb00067:* Relaxation and Multiplication in Bi doped Graphen

HLRN Project ID:	hbp00067
Run time:	III/2020 – I/2024
Project Leader:	Prof. Thomas Frauenheim
Project Scientists:	Yuxiang Liu
Affiliation:	BCCMS, University of Bremen

Overview

Carrier multiplication (CM), which involves the generation of multiple excitons from the absorption of a single photon, offers a groundbreaking avenue for enhancing photovoltaic conversion efficiency. Graphene has emerged as a promising candidate for CM due to its unique attributes, including a linear band structure, strong electron-electron scattering, and weak electron-phonon couplings. In this proposal, we present an investigation into CM properties in doped graphene. Theoretical simulations using nonadiabtic molecular dynamics combined (NAMD) with real-time time-dependent density functional theory (rt-TDDFT) method reveal that doping level can lead to remarkable differences in CM conversion efficiency. In n-doped graphene, raising the Fermi level from 0.40 eV to 0.78 eV through nitrogen atom doping elevates the CM quantum yield from 1.41 to 1.89. In alignment with these findings, measurements from time and angle-resolved photoemission spectroscopy (TR-APRES) on n-doped graphene also confirm the strong correlation between doping levels and CM conversion efficiency. These results underscore the efficacy of manipulating the performance of graphene in optoelectronic devices through the strategic tuning of doping levels.

Results

We employed the NAMD with rt-TDDFT method to explore the influence of doping levels on the CM process in graphene. To create n-doped graphene with varying doping levels, we replaced two, four, and six carbon atoms with nitrogen atoms in a $6\sqrt{3} \times 6\sqrt{3}$ graphene supercell. Nitrogen atoms clearly introduce extra electrons into the system, shifting the Fermi level away from the Dirac point by 0.40 eV, 0.58 eV, and 0.78 eV, respectively. To stimulate the excited carrier relaxation process, we generated a pair of electron-hole by moving an electron from the valence bands to the conduction bands at 300 K, with an excitation energy of approximately 3.52 eV. In the case of pristine (undoped) graphene, the linear band structure results in a symmetric excitation, where the excess energies of both the electron and hole ΔE_e and ΔE_h) are equal to 1.76 eV. Here, the excess energy is defined as the energy difference between excited carriers and Fermi level. In the case of N-doped graphene, due to the shifted Fermi levels, the electron excess energies are 1.36 eV, 1.18 eV and 0.98 eV in 2N-doped, 4N-doped and 6N-doped graphene, respectively.

In general, CM process in graphene can be categorized into two types. In the first scenario, CM occurs through the scattering of additional electrons from the valence bands to the conduction bands, and this interband transition is commonly referred to as $carrier$ $multiplication$. On the other hand, when we consider carriers relative to the Fermi level, CM takes place through Coulomb-induced scattering electrons from Fermi sea over the Fermi level, and this intraband transition is defined as *hot carrier multiplication*. Studies have shown that CM primarily involves interband scattering at low Fermi energy levels ($E_F < 0.1$ eV), while intraband scattering becomes more significant in the CM process at higher Fermi energy levels ($E_F > 0.15$ eV)[1]. In other words, *hot carrier multiplication* tends to dominate the CM process

in strongly doped graphene. In the following sections, we will refer to CM as *hot carrier multiplication.*

To illustrate the influence of doping levels on CM, we conducted simulations to assess the CM quantum yield (QY) in various N-doped graphene configurations. As depicted in Figure1, strongly n-doped graphene indeed leads to more efficient CM. Specifically, the CM QY increases from 1.41 to 1.89 as the Fermi level is raised from 0.40 eV to 0.78 eV. Notably, for pristine graphene, CM is not observed, contradicting previous theoretical predictions [2]. In undoped graphene, excited holes and electrons both occupy higher energy regions, suggesting the occurrence of Auger recombination. Simultaneously, a portion of excited holes and electrons also distribute in lower energy regions, which are related to the CM process or phonon-assisted cooling relaxation. The absence of CM in pristine graphene can be attributed to the equilibrium between CM and Auger recombination rates. Both theoretical and experimental research have shown that higher carrier concentration conditions favor Auger recombination, which competes with the CM process [3,4]. Winzer reported that the CM rate and Auger recombination rate reach equilibrium very quickly when the initial carrier density is in the range of $10^{13} cm^{-2}$, while the carrier concentration in our simulation is exactly $3 \times 10^{13} cm^{-2}$. Therefore, the absence of CM in pristine graphene results from higher carrier concentration inducing more efficient Auger recombination. In contrast, n-doped graphene favors the CM process. It's evident that a portion of the excited holes occupies the doped states, and the more strongly n-doped the graphene, the more excited holes occupy these doped states. In strongly n-doped graphene, photoexcited electrons can readily find scattering partners in the Fermi sea, leading to their involvement in the CM process due to the larger scattering phase space. As a result, the CM process prevails over Auger recombination, dominating the carrier relaxation dynamics.

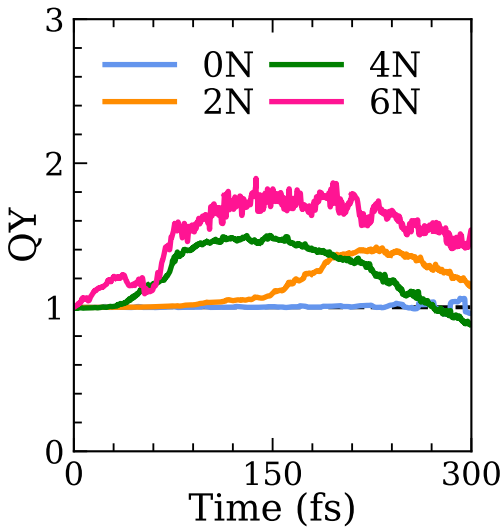

Figure1: CM QY of graphene with different doping levels. The electron-hole pair is generated by phonon with energy of 3.52 eV at 300K.

Outlook

In next phase, we will investigate CM in Bi-doped graphene based on theoretical quantum machnical methods.

Publications

Q. Liu*, X. Y. Lu*, Y. X. Liu*, Z. Li, P. Yan, et al, *Carrier Relaxation and Multiplication in Bi doped Graphene*. Small, 2023, 2206218.

Presentations

1. Andrea Tomadin, Sam M Hornett, Hai I Wang, Evgeny M Alexeev, Andrea Candini, Camilla Coletti, Dmitry Turchinovich, Mathias Kläui, Mischa Bonn, Frank HL Koppens, et al., *The ultrafast dynamics and conductivity of photoexcited graphene at different Fermi energies*, Science Advances, 4, no. 5, eaar5313, 2018.
2. Torben Winzer, Andreas Knorr, and Ermin Malic, *Carrier multiplication in graphene*, Nano Letters,10, no. 12, 4839–4843, 2010.
3. Isabella Gierz, Jesse C Petersen, Matteo Mitrano, Cephise Cacho, IC Turcu, Emma Springate, Alexander St¨ohr, Axel K¨ohler, Ulrich Starke, and Andrea Cavalleri, *Snapshots of non-equilibrium Dirac carrier distributions in graphene*, Nature Materials, 12, no. 12, 1119–1124, 2013.
4. Torben Winzer and Ermin Malić, *Impact of Auger processes on carrier dynamics in graphene,* Physical Review B, 85, no. 24, 241404, 2012

6.24 *hbp00068:* Enhanced sampling methods for constructing free energy surfaces of antibiotic permeation through porins

HLRN Project ID:	hbp00068
Run time:	IV/2020 – IV/2024
Project Leader:	Professor Dr. Ulrich Kleinekathöfer
Project Scientists:	Abhishek Acharya
Affiliation:	Constructor University

Overview

Understanding the process of antibiotic entry into bacterial cell holds the promise of enabling the design on novel drugs that can enter more efficiently into bacteria and hence show improved antibacterial efficacy. Designing new antibacterials is one of the principal goals of the drug development community especially as reported rates of infections with bacterial species possessing multidrug resistance only increase with every passing year [1]. Discerning the atomic details and energetics of the permeation process is possible through all-atom molecular modeling of the various diffusion channels that play a key role in the entry process. The overarching goal of this present project to employ advanced sampling methods towards the study of the permeation pathways of different antibiotics through the OmpF porin (Figure 1A) and its homologs. Previous work components within this project already demonstrated the utility of temperature accelerated sliced sampling (TASS) in unraveling the details of ciprofloxacin (CIP) permeation process and the associated channel loop dynamics, especially in the L3-FS (F118 – S125) segment of loop L3 (Figure 1B) [2, 3].

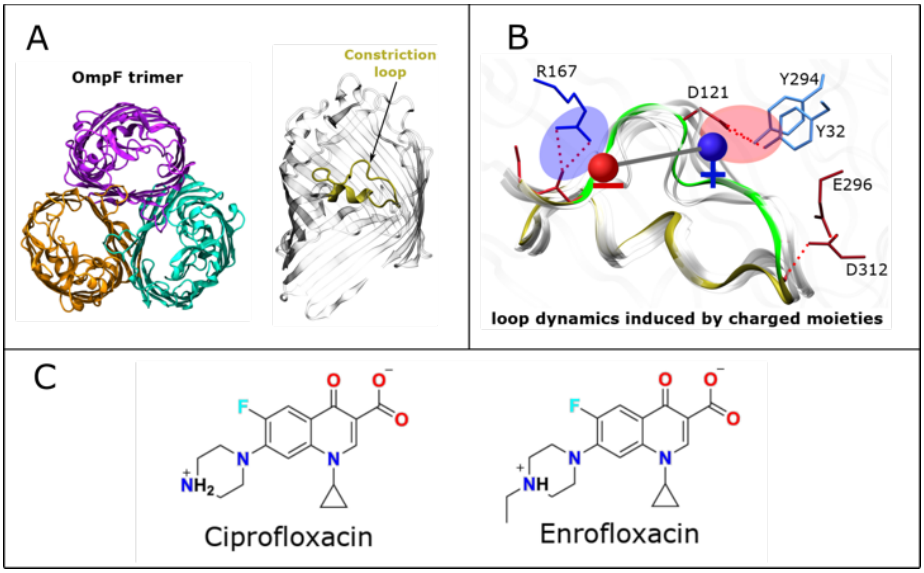

Figure 1: A. A cartoon representation of the OmpF channel trimer. Adjacent is shown a monomer with the constriction loop at the center of the channel (in yellow). This L3 loop forms the constriction zone at the center responsible for the key barrier to permeation. **B.** Induced conformational dynamics of loop L3 under the influence of charged moieties on the antibiotic molecule. The L3 configuration corresponding to the crystal structure is colored green, and alternate conformations of the loop are colored in grey. The zwitterionic antibiotic is represented as a dipole. **C.** The ciprofloxacin and the enrofloxacin molecule. Note that enrofloxacin differs from ciprofloxacin in that it has an additional ethyl substituent on the positively charged amine moiety. The image is reproduced with permission from Ref. 4. (Copyright 2023. American Chemical Society).

In the next step, we performed simulations of enrofloxacin (ENR) transport through OmpF. The results of these simulations and comparison with ciprofloxacin permeation pathway suggested the possibility of two distinct permeation mechanisms: L3 dynamics dependent (L3D-D) and L3 dynamics independent (L3D-I) mechanism [4].

Results

Foremost, the free energy estimation for ENR and comparison vis-à-vis the CIP estimates suggest that ENR permeation is possible only via path II (Figure 2A). We estimated a barrier of 13.5 kcal/mol which is greater that the CIP barrier of 11.5 kcal/mol. Moreover, the analysis of the metastable states associated with the observed permeation paths suggested that; a) there is a presence of strong affinity sites both at the *cis* side (state V) and the *trans* side (state VII) along the ENR permeation pathway, and b) the presence of a bulky ethyl moiety on the ENR molecule precludes the possibility of the interactions of the positively charged amine group with the negative residue of the L3 loop due to steric hindrance (Figure 2B, left panel). The presence of the affinity sites at both sides of the constriction zone explains the experimentally observed $k_{on,cis}$ and $k_{on,trans}$ values that are similar in magnitude. The observed absence of ENR interactions with the negative charged L3 residues, in particular D121, is of importance to the permeation mechanism. In case of ENR, we find reduced L3 conformational fluctuations compared to CIP (Figure 2B, right panel). In case of CIP, the amine group interacts strongly with the D121 residue of the L3 and induces conformational changes in the loop as indicated by the greater root mean square fluctuations of the L3-FS segment.

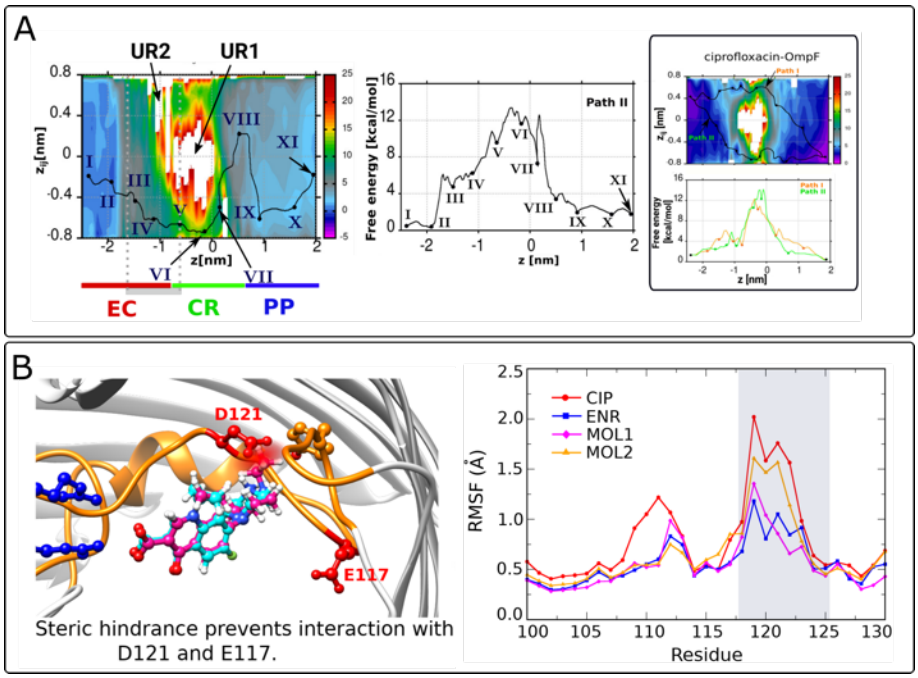

Figure 2: **A.** Left: Two-dimensional free energy surface in the *z*-vs-z_{ij} space and the minimum free energy path (MFEP) obtained using the zero-temperature string method. The three regions of the channel: extracellular region (EC), constriction region (CR) and periplasmic region (PP) of the channel are indicated by a bar together with the pre-orientation region (in gray). Center: The free energy along the MFEP (path II) is shown. Right: The free energy landscape and the associated permeation paths for CIP permeation is shown for reference. Here, *z* denotes the *z*-axis projection of the center of mass distance between the antibiotic molecule and the channel, and z_{ij} describes the antibiotic orientation with respect to the pore axis. **B.** Left: ENR interactions with with D113, E117 and D121 not feasible due to the steric block from the ethyl moiety. Right: Root mean squared fluctuation plots (RMSF) of the C-α atoms of the L3 loop calculated from simulations of CIP, ENR, MOL1 and MOL2 permeation. The L3-FS segment is indicated by the gray shaded reagion (F118-S125). The image is reproduced with permission from Ref. 4. (Copyright 2023. American Chemical Society).

Additionally, we also simulated the permeation of molecules MOL1 (negatively charged) and MOL2 (positively charged) and observed the associated L3-FS fluctuations. For MOL1, we observed low conformational fluctuations, like ENR, and for MOL2, larger fluctuations similar to CIP. Finally, we performed TASS simulations of carbenicillin (CBN; negatively charged) and puromycin (PUR; positively charged) that are clinically relevant antibiotics in use. We observed larger L3-FS fluctuations in case of PUR compared to CBN (Figure 3). These simulations also reiterated the aforementioned findings of a larger L3 conformational dynamics in case of molecules that possess a positively charged, whereas molecules with only negatively charged moieties do not induce such fluctuations. We term the former as L3D-D and the latter as L3D-I pathway.

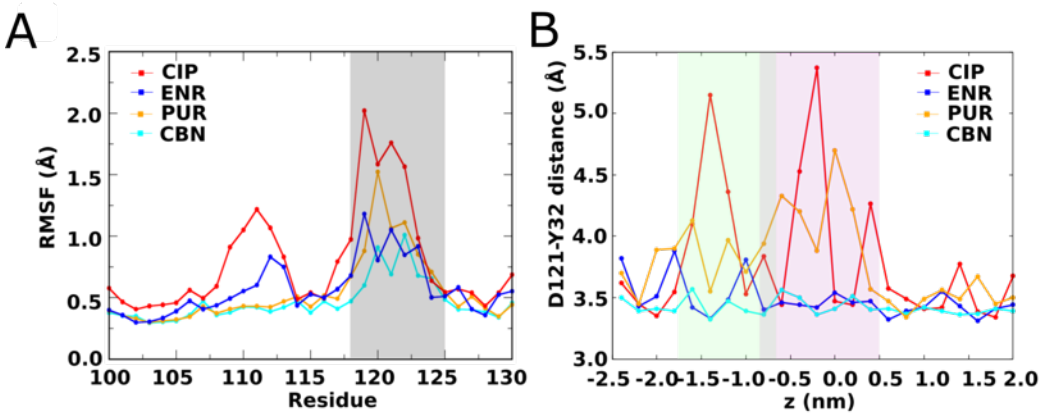

Figure 2: A. Root mean squared fluctuation plots (RMSF) of the C-α atoms of the L3 loop calculated from simulations of CIP, ENR, PUR and CBN permeation though OmpF. The L3-FS segment is indicated by the gray shaded reagion (F118-S125). **B.** The average hydrogen bond distance between D121 and Y32 residues that undergoes fluctuations under the influence of strong D121 interactions with the positive charge of the antibiotic. The image is reproduced with permission from Ref. 4. (Copyright 2023. American Chemical Society).

Outlook

Overall, these results suggest that antibiotic transport pathways through OmpF may or may not involve interactions with the constriction loop depending on charge distribution on the antibiotic. If the charge distribution is such that promotes strong interaction with the L3 loop, the L3D-D mechanism becomes dominant. Such fluctuations likely enable the antibiotic to negotiate the large entropic barrier at the channel constriction zone and thus permeate more efficiently. Molecules that do not interact with the L3 loop follow the L3D-I pathway that is associated with less efficient permeation rates. These insights could be useful in the development of antibacterial molecules with improved permeation rates. The redesign strategy would involve the introduction of chemical moieties into existing bacterial inhibitors that improves the engagement of the L3-FS during permeation, thereby improving the permeation rates.

Publications

1. Acharya, A.; Prajapati, J. D.; Kleinekathöfer, U. *Atomistic Simulation of Molecules Interacting with Biological Nanopores: From Current Understanding to Future Directions*. J. Phys. Chem. B 2022, 126, 3995–4008.
2. Acharya, A.; Prajapati, J. D.; Kleinekathöfer, U. *Improved Sampling and Free Energy Estimates for Antibiotic Permeation through Bacterial Porins*. J. Chem. Theory Comput. 2021, 17, 7, 4564–4577.

3. Acharya, A.; Ghai, I.; Piselli, C.; Prajapati, J. D.; Benz, R.; Winterhalter, M.; and Kleinekathöfer, *U. Conformational Dynamics of Loop L3 in OmpF: Implications toward Antibiotic Translocation and Voltage Gating*. J. Chem. Inf. Model. 2023 63:910–927.
4. Acharya, A.; Kalyanashis, J.; Kleinekathöfer, U. *Antibiotic Charge Profile Determines the Extent of L3 Dynamics in OmpF: An Expedited Passage for Molecules with a Positive Charge*. J. Phys. Chem. B 2023, 127, 50, 10766–10777.

6.25 *hbp00075:* Computational search for more efficient thermal barrier coatings using the Wigner formulation

HLRN Project ID:	hbp00075
Run time:	I/2023 – I/2024
Project Leader:	Dr. Anees Pazhedath[1]
Project Scientists:	Dr. Michele Simoncelli[2], Prof. Dr. Nicola Marzari[1] and, Prof. Dr. Lucio Colombi Ciacchi[1]
Affiliation:	[1] U Bremen Excellence Chair, Bremen Center for Computational Materials Science, and MAPEX Center for Materials and Processes, University of Bremen, Germany [2] Theory of Condensed Matter Group, Cavendish Laboratory, University of Cambridge, UK

Overview

Thermal barrier coatings (TBCs) are employed to protect the base alloy of turbine blades of jet engines, electricity generators, and large ships from high-temperature jet-stream deterioration [1]. The durability and reliability of the components strongly depend on the thermal and mechanical properties of TBCs. Understanding which materials offer the best performance is an active area of research. It is facing several challenges: experiments on these materials are time-consuming and expensive. At the same time, theoretical studies based on molecular dynamics simulations do not provide a direct information about the microscopic properties of the heat carriers. These limitations have been overcome with the recently introduced Wigner formulation of thermal transport [2, 3] and first-principles calculations; an approach that allows resolving with quantum accuracy how every microscopic heat carrier contributes to heat conduction. The current project aims to employ the Wigner formulation to search for more efficient TBC materials, rigorously. Both crystalline and disordered (solid solutions) materials will be investigated.

Results

We combine first-principles calculations with the Wigner formulation to unveil the microscopic heat conduction mechanisms in $LaPO_4$ and in its solid solutions with $GdPO_4$. These materials are employed TBCs due to their unique thermal and mechanical properties [4]. **Fig. 1a** shows the thermal conductivity of $LaPO_4$ as a function of temperature. At low temperatures, the population conductivity (κ_p) is predominant, decreases with an increase in temperature, and exhibits a $1/T$ dependence in decay, as anticipated from the linearized Peierls-Boltzmann transport (LBTE) equation [5]. However, the experimental data shows a mild $1/T$ dependence. This discrepancy is corrected in the Wigner formulation by adding the coherences contribution (κ_c) to the total thermal conductivity. The κ_c increases with temperatures and starts to become significant at high temperatures, the complex crystal regime. This onset of the substantial contribution of κ_c compensates for the $1/T$ decay of κ_p and restores the mild $1/T$ dependence in total conductivity ($\kappa_T = \kappa_p + \kappa_c$) at higher temperatures, and agrees well with experiments. This exemplifies the necessity of using the Wigner method to add all the coherences contributions, and thus to have an accurate description of the thermal conductivity of complex crystals.

More precisely, we have shown that the macroscopic trend of the conductivity is determined by the coexistence of microscopic particle-like and wave-like conduction mechanisms: the

former strongly decay with temperature, while the latter increases with temperature and the sum of the two yields the mildly decreasing trend observed in experiments.

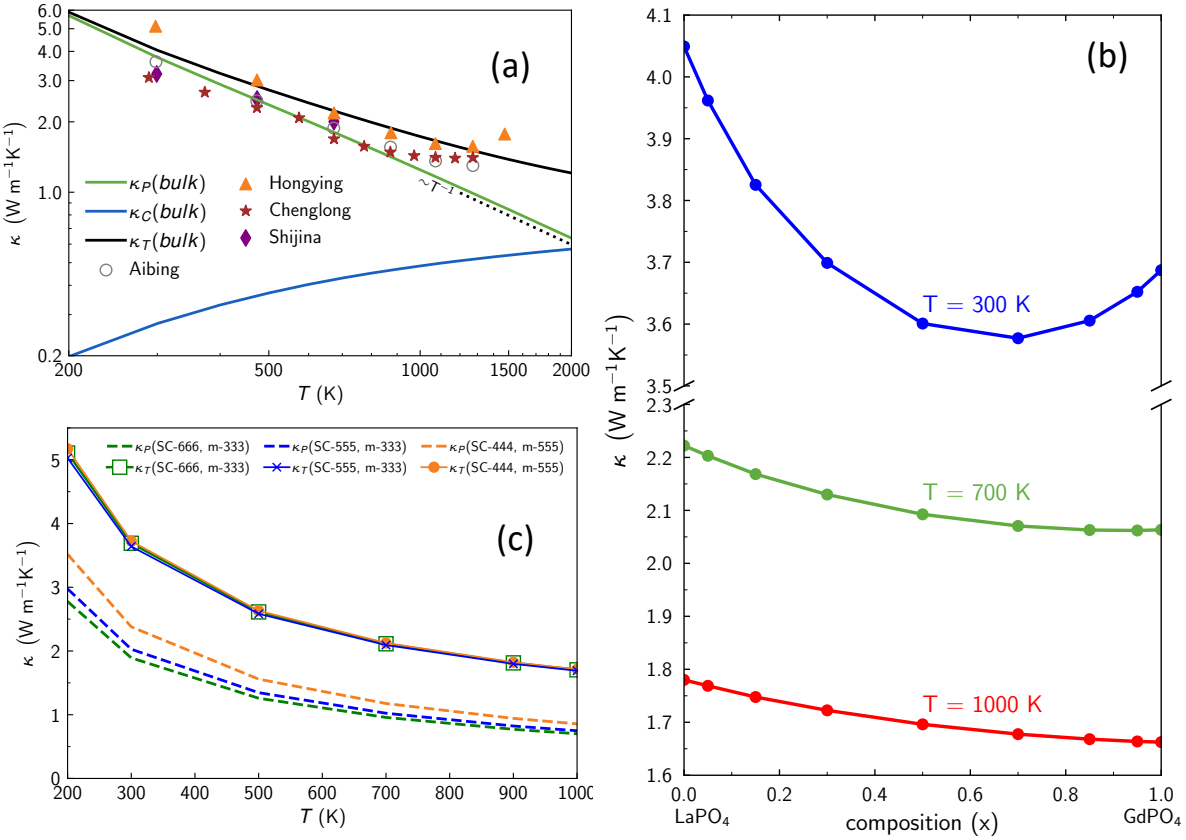

Figure 1: (a) Thermal conductivity of $LaPO_4$ crystal as a function of temperature (in log-log scale). Green, populations conductivity κ_p which follows the $1/T$ decay typical of Peierls' particle-like transport in crystals with dominant third-order anharmonicity. Blue, coherences conductivity κ_c, significant at high temperatures. Black, total conductivity, $\kappa_T = \kappa_p + \kappa_c$. For the experimental reference and more details see [arXiv:2309.10789] and reference therein. (b) Thermal conductivity of $La_{1-x}Gd_xPO_4$ alloys as a function of composition, at 300, 700, and 1000 K. The effect of compositional disorder becomes less relevant as temperature increases. (c) Thermal conductivity of models of $La_{0.5}Gd_{0.5}PO_4$ with different disorder lengthscales. We highlight how the populations conductivity (κ_p) (dashed) decreases as the size of the model increases, such a decrease is compensated by an increase in the coherences conductivity (κ_c); this implies that these different models have practically indistinguishable total conductivities

In general, the presence of compositional disorder (alloying) causes a reduction of the thermal conductivity and thus is expected to be beneficial for TBC applications [4]. Standard LBTE-based perturbative treatment of compositional disorder – which is accurate in weakly anharmonic systems in which low-frequency vibrational modes dominate transport – fails in systems where transport is not dominated by low-frequency modes [6]. $LaPO_4$ belongs to this class, hence, we develop a computational protocol that exploits the Wigner formulation to describe compositional-mass disorder explicitly, overcoming the limitations of the standard LBTE-based perturbative treatment of disorder. We employed the newly developed protocol to investigate the thermal properties of $La_{1-x}Gd_xPO_4$ alloys. We described explicitly compositionally disordered samples simulating systems containing up to 5184 atoms, a size that is one order of magnitude larger than that tractable by state-of-the-art ab initio molecular dynamics techniques. We discussed how the interplay between anharmonicity and disorder affects thermal transport in $La_{1-x}Gd_xPO_4$ alloys at different temperatures (**Fig. 1b**), showing that disorder has strong effects around room temperatures and almost negligible effects at

high temperatures (& 700 K). We have also shown that the LBTE yields a size-dependent conductivity in the presence of disorder (dashed lines in **Fig. 1c**), while the Wigner formulation yields compatible results for compositionally disordered models having different sizes (solid lines with markers); the latter behavior shares analogies to the size-consistent results obtained using the Wigner formulation in structurally disordered materials. This novel computational scheme sets the stage to rationalize thermal transport with quantum accuracy in solids with compositional-mass disorder and will be potentially very useful to develop novel design strategies for thermal barrier coating systems.

Outlook

In the future, we plan to study the thermal transport in another class of TBC materials, rare-earth pyrochlores such as $La_2Zr_2O_7$, $Yb_2Zr_2O_7$, $La_2Hf_2O_7$, and their solid solutions, $(La_{1-x}Yb_x)_2Zr_2O_7$ and $La_2(Zr_{1-x}Hf_x)_2O_7$ [4]. We further plan to extend these studies to glassy systems, where we employ the machine learning potentials, enabling us to evaluate the harmonic and anharmonic conductivity in the bulk limit, accurately.

Publications

1. Pazhedath, L. Bastonero, N. Marzari, and M. Simoncelli, *First-principles characterization of thermal conductivity in $LaPO_4$-based alloys*, arXiv:2309.10789 (2023)

Presentations

1. A. Pazhedath, L. Bastonero, N. Marzari, and M. Simoncelli, *Wigner thermal transport in rare-earth zirconates and their solid solutions*, DPG-Frühjahrstagung (DPG Spring Meeting), Technical University Dresden, Germany, March, 26-31st (2023)
2. A. Pazhedath, L. Bastonero, N. Marzari, and M. Simoncelli, *First-principles characterization of thermal conductivity in $LaPO_4$-based alloys*, ADIS-2023, Ringberg, Tegersee, Germany, 29thOct - 3rdNov (2023)

References

1. N. P. Padture, Nature Materials 15, 804 (2016)
2. M. Simoncelli, N. Marzari, and F. Mauri, Nature Physics 15, 809 (2019)
3. M. Simoncelli, N. Marzari, and F. Mauri, Physical Review X 12, 041011 (2022)
4. B. Liu, Y. Liu, C. Zhu, H. Xiang, H. Chen, L. Sun, Y. Gao, and Y. Zhou, Journal of Materials Science & Technology 35, 833 (2019).
5. J. M. Ziman, *Electrons and phonons: the theory of transport phenomena in solids, Oxford classic texts in the physical sciences*. Clarendon Press; Oxford University Press, Oxford: New York, (2001)
6. S. Thébaud, C. A. Polanco, L. Lindsay, and T. Berlijn, Physical Review B 102, 094206 (2020)

6.26 *hbp00076:* Multiscale analysis of the dynamic interactions of nanoparticles and oil-soluble surfactants at liquid interfaces

HLRN Project ID:	hbp00076
Run time:	I/2023 – I/2024
Project Leader:	Dr. Saeed Amiri
Project Scientists:	Prof. Dr. Lucio Colombi Ciacchi
Affiliation:	Hybrid Materials Interfaces Group, Faculty of Production Engineering, University of Bremen

Overview

Particle-stabilized emulsion systems have a wide range of industrial uses, including cosmetics, pharmaceuticals, oil recovery, and materials processing. However, creating stable emulsion systems that contain multiple components is a complicated process that requires significant resources and experimentation. This is because of the complex nature of these systems and the molecular-level interactions between heterogeneous and multi-component oil/water interfaces that contain surfactant molecules and nanoparticles. Our project seeks to bridge the gap between molecular-level interactions and the macroscopic behavior of emulsion films. Our goal is to establish design rules that will enable us to create particle/surfactant emulsion systems with precision by manipulating key parameters such as oil/water surface tension and macroscopic contact angle. To achieve these objectives, we will carry out experiments and employ atomistic/mesoscopic simulations. The general design of the project is based on water-dispersable, hydrophilic nanoparticles and oil-soluble surfactants. This system prevents volume-phase interactions between particles and surfactants and limits such interactions to the interfacial region. In order to retain a realistic scope of the project, the investigated system is limited to a well-defined set of constituents that allows comparability with other systems. Silica nanoparticles are chosen for their hydrophilicity, monodispersity, sphericity, purity, and availability in small sizes. The surface chemistry of silica can be efficiently tailored via reaction with various silanes. Decane is selected as an organic solvent mainly because it can be purified to the high degree essential for interfacial measurements, which are sensitive to parts-per-billion amounts of surface-active impurities. Lastly, oil-soluble surfactants with a hydrophobic tail with different functional head groups are chosen [1-3].

Results

The project was marked by significant advancements in our investigation of the complex interactions occurring at the interface of heterogeneous systems, specifically the interplay between functional silica nanoparticles and the water-decane interface. Our research aimed to elucidate the dynamic behavior of these systems, both in the presence and absence of octadecylamine (ODA) surfactants. This report provides a short overview of the research activities and findings achieved during this period. A key aspect of our research effort was the careful preparation of simulation systems to emulate real-world scenarios faithfully. The core focus of our simulations was to unravel the complexities of nanoparticle interactions at the liquid-liquid interface. Two distinct sets of simulations were designed and executed: one with the presence of a nanoparticle (NP) and another without a NP. In both cases, systems with different concentrations of ODA surfactants were prepared (**Fig. 1a**). These simulations played a critical role in our quest to understand the complex interactions within these systems. A notable achievement during this project period was the successful calculation of surface tension for both sets of systems. These calculations encompassed a wide range of ODA

concentrations, providing a comprehensive dataset that shed light on the effects of surfactants on the interfacial tension of the water-decane interface. Of particular significance was the observation that the presence of functional silica nanoparticles had a minimal impact on surface tension. This finding underscored the dominant role played by ODA in modulating interfacial properties. These results were in close agreement with experimental observations, consolidating our understanding of the interplay between nanoparticles and surfactants at liquid interfaces (**Fig. 1b**).

Even with the notable progress made in clarifying the impact of nanoparticles and surfactants on interfacial tension, the underlying molecular-level mechanisms remained a subject of ongoing investigation. Most of our research efforts during this period were dedicated to delving deeper into the intricate molecular details.

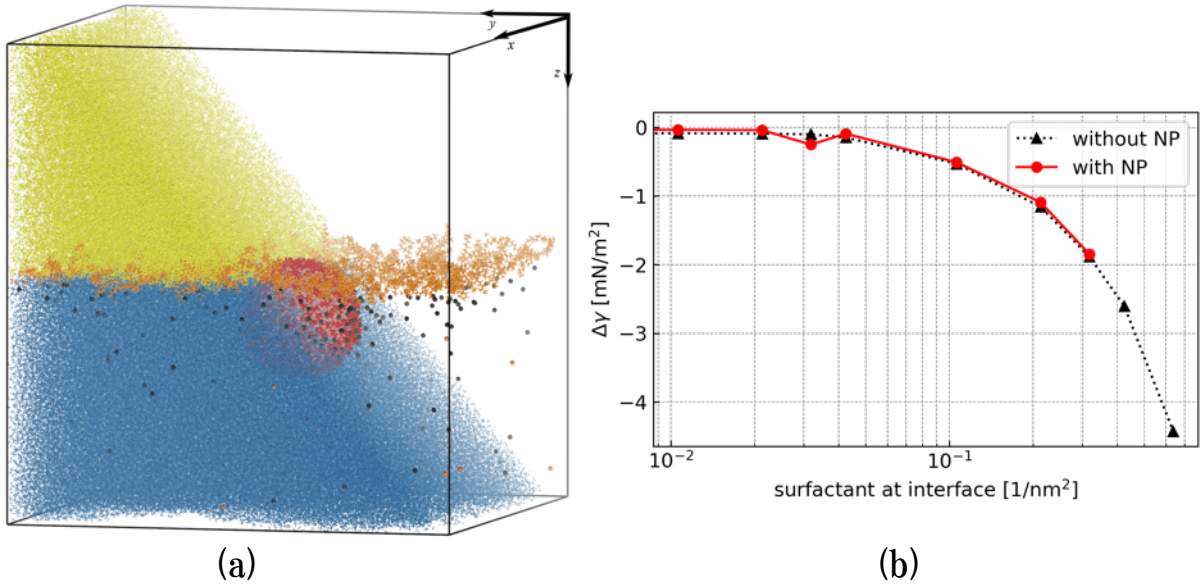

(a) (b)

Figure 1: Figure (a) displays a system with a single nanoparticle (red in the middle of the box) at the water (blue) and decane (yellow) interface, with surfactants (orange) and ions (black) in the water phase. A portion of the water and decane has been removed for visibility, highlighting the interface. Note that such systems typically contain over a million atoms. In Figure (b), we observe the ongoing simulations analyzing interfacial tension changes in systems with and without nanoparticles in the presence of surfactants. Further simulations are planned to deepen our understanding of these tension alterations, aligning with our project's objectives.

Outlook

Our aim was to unravel the precise mechanisms through which surfactants influence interfacial tension. The ongoing mechanistic analysis seeks to uncover the molecular arrangements and interactions transpiring at the water-decane interface in the presence of surfactants. This will yield valuable insights into the mechanisms through which surfactants effectively reduce interfacial tension and govern the behavior of these complex systems. We simulated systems featuring more silica nanoparticles as part of our research strategy. These systems, twice the size of those in the initial simulations, represent scenarios encountered in practical applications. Notably, these simulations involved systems comprising more than two million atoms, necessitating advanced computational resources. The data derived from these simulations will serve as a cornerstone in the calculation of essential parameters and forces crucial for coarse-grain simulations. By simulating systems with an increased number of nanoparticles at the interface, our goal is to gain a deeper understanding of the interparticle interactions governing real-world systems in greater detail.

References

1. Y. Chevalier. M. A. Bolzinger Colloids surf. Physicochem. Eng. Asp., 439 (2013).
2. R. Moreno Colloidal Processing of Ceramics and Composites. Appl. Ceram., 111 (2012).
3. S. Reynaert, P. Moldenaers, J. Vermant Control over Colloidal Aggregation in Monolayers of Latex Particles at the Oil-Water Interface. Langmuir, 22 (2006)